Automated Detection and Classification of Intracranial Aneurysms based on 3D Surface Analysis

A dissertation submitted by

Alexandra Lauric

In partial fulfillment of the requirements

for the degree of Doctor of Philosophy in

Computer Science

TUFTS UNIVERSITY

August 2010

ADVISER: Eric L. Miller

Abstract

Intracranial aneurysms are localized, abnormal, arterial dilations with a variable risk of rupture, which can lead to subarachnoid hemorrhage (SAH), a condition associated with high morbidity and mortality. The majority of non-traumatic SAH cases are caused by ruptured intracranial aneurysms. Accurate detection can decrease a significant proportion of misdiagnosed cases. However, only a small percent of all detected incidental aneurysms proceed to rupture and preventive treatment carries risks of complications, thus creating a need for aneurysm rupture risk stratification tools to help guide the treatment of these asymptomatic lesions.

This research investigates the two major areas of intracranial aneurysm analysis - aneurysm detection and rupture risk classification. First a method for automatic detection of intracranial aneurysms is proposed. Applied to the segmented cerebral vasculature, the method detects aneurysms as suspect regions on the vascular tree and is designed to assist diagnosticians with their interpretations. The method is imaging modality independent and was tested on magnetic resonance imaging, computed tomography and 3D angiography data. Second, a new approach to morphological analysis of the 3D shape of an aneurysm is presented as a differentiator of rupture risk status in cerebral aneurysms. The *writhe number* is introduced as a novel surface descriptor which proves useful in both detection and classification studies. In addition to the writhe number, 3D shape descriptors based on surface curvature and centroid-radii model are proposed and investigated for rupture risk classification.

The combined use of these shape descriptors yields very promising results for predicting rupture risk in intracranial aneurysms. In experiments, the aneurysm detection method achieved 100% sensitivity, independent of modality. Depending on the imaging modality, there are between 0.66 and 5.7 false positives per study; the worst case performance is comparable to that of existing detection research. The classification method resulted in a $\sim$20% increase in prediction accuracy, compared to other commonly used shape indexes. These results support the utility of writhe number aneurysm shape analysis as a high order descriptor with potential clinical use in intracranial aneurysm detection and rupture risk stratification.

Acknowledgements

I would like to thank the Tufts University Department of Computer Science for providing an academic atmosphere that is stimulating, challenging, and supportive of its students. I am particularly grateful to my advisor, Eric Miller, for his guidance over the period we worked together. Prof. Miller achieved the perfect balance between offering all his support, while at the same time allowing me to grow into an independent researcher. His high research standards inspired me to push my limits and thrive for excellence. I would like to thank the members of my dissertation committee, not only for their helpful suggestions in the final writing of this thesis, but also for the constant inspiration they provided as researchers, teachers and mentors during my graduate years: Prof. Diane Souvaine for encouraging me to pursue a PhD degree, Dr. Sarah Frisken for introducing me to the world of medical imaging, Dr. Adel Malek for providing great research problems and acting as my medical research advisor, and Prof. Lenore Cowen for her advice and support at key times in my doctoral studies.

I would like to thank my friend Elena for her help editing this thesis, but mostly for her support and friendship during our graduate years and beyond. I must thank my parents for compelling me to study Computer Science. As it turns out, they were right! Finally, this thesis is dedicated to my husband, Petru. His never-ending patience, encouragement and support made this work possible.

Contents

1 Introduction **1**

1.1 Overview of Automatic Detection 3

1.2 Overview of Rupture Status Classification 5

1.3 Outline of the Thesis 8

2 Background and Related Work **10**

2.1 Geometry of Curves and Surfaces 10

2.1.1 Curves in the Plane 10

2.1.2 Surfaces in 3-Dimensional Space 11

2.1.3 Curvature 13

2.1.4 Writhe Number 20

2.2 Probability and Statistics 23

2.3 Aneurysm Detection and Characterization 25

2.3.1 Aneurysm Detection 25

2.3.2 Rupture Analysis 27

3 The Writhe Number **34**

3.1 The Writhe Number of Surfaces 34

3.2 Writhe Number for Aneurysm Detection 36

3.2.1 The Writhe of a Cylinder 37

3.2.2 The Writhe of an Extruded Surface Along a Parabola 37

3.2.3 Generalization of Writhe Number 38
3.3 Writhe Number for Rupture Status Prediction 38
3.3.1 A Physical Interpretation of Surface Writhe 39

4 Automated Detection of Intracranial Aneurysms using the Writhe Number of Surfaces 42
4.1 Method 42
4.1.1 Overview of the Detection Algorithm 42
4.1.2 Segmentation 43
4.1.3 Medial Axis Detection 43
4.1.4 Short Branches Selection 43
4.1.5 Local Neighborhood Model 44
4.1.6 Writhe Number Computation 46
4.1.7 False Positive Reduction 46
4.2 Clinical Data 47
4.2.1 3D-RA, MRA and CTA 47
4.2.2 Preprocessing 49
4.2.3 Experimental Validation of Local Neighborhoods 50
4.3 Aneurysm Detection Results 53
4.4 Discussion 56

5 Rupture Status Classification of Intracranial Aneurysms using the Writhe Number of Surfaces 62
5.1 Clinical Data 63
5.2 Method 65
5.2.1 Overview of the Classification Algorithm 65
5.2.2 Segmentation 66
5.2.3 Isolation of Aneurysms 66

5.2.4 Writhe Number Computation 68
5.2.5 Histogram Statistics 68
5.2.6 Classification 68
5.3 Classification Results 69
5.3.1 Rupture Status Prediction 69
5.3.2 Sensitivity to Segmentation 74
5.3.3 Sensitivity to Cutting Planes Definition 75
5.3.4 Synthetic Data Analysis 77
5.4 Discussion 78

6 Rupture Status Classification of Intracranial Aneurysms using Surface Curvature and the Centroid-Radii Model 90

6.1 Method 90
6.1.1 Overview of the Classification Algorithm 90
6.1.2 Segmentation 91
6.1.3 Isolation of Aneurysms 91
6.1.4 Surface Curvature and Centroid-Radii Computation 91
6.1.5 Histogram Statistics 92
6.1.6 Classification 92
6.2 Classification Results 93
6.2.1 Rupture Status Prediction 93
6.2.2 Sensitivity to Segmentation 97
6.2.3 Sensitivity to Cutting Planes Definition 98
6.2.4 Synthetic Data Analysis 99
6.3 Discussion 100

7 Conclusions and Future Work 107

7.1 Ongoing Research 108

7.2 Future Work 109

Appendices **111**

A Writhe Number Analysis 111

A.1 Writhe Number of a Cylinder 111

A.2 Writhe Number of an Extruded Surface Along a Parabola . . 112

Bibliography **115**

List of Figures

2.1 Illustration of the curvature of elliptical surfaces. (a) The Gaussian curvature of an elliptical surface is positive. (b) The mean curvature of an elliptical surface is positive if the surface is locally convex and negative if the surface is locally concave. 15

2.2 Illustration of the curvature of hyperbolic surfaces. (a) The Gaussian curvature of a hyperbolic surface is negative. (b) The mean curvature of a hyperbolic surface has both zero and non-zero values. 15

2.3 Gaussian and mean curvature of a more complex surface. (a) Gaussian curvature capture intrinsic geometric properties, i.e., whether a region is elliptical or hyperbolic. (b) mean curvature captures extrinsic geometric properties, i.e., whether an elliptical region is convex or concave. 16

2.4 A tubular neighborhood of a polygon P, represented as an offset manifold in the direction of the unit normal field of P. The offset distance is bounded by constant ϵ. 17

2.5 Computing the curvature on aneurysms represented as triangular meshes. (a) Complete model of an aneurysm represented as a triangular mesh. (b) Detail on the mesh. The yellow disk surrounding vertex v represents the neighborhood B over which the curvature at v is computed. (c) The angle between a pair of adjacent faces sharing an edge e is computed as the angle between the normals at the two triangles. $|e \cap B|$ is the length of $e \cap B$ (between 0 and $|e|$). 19

2.6 (a) A curve crossing is considered positive if, in order to align two curve intervals, the upper interval is rotated counterclockwise with an angle between 0 and π. (b) A curve crossing is considered negative if, in order to align two curve intervals, the upper interval is rotated clockwise with an angle between 0 and π. 22

2.7 The trefoil knot curve has 3 crossings and a writhe number of 3. (a) 3D view along x axis. (b) 3D view along the y axis. (c) 3D view along the z axis. 22

2.8 Interpretation of third and fourth central moments. (a) Normal distribution with mean μ. (b) Distribution with positive skewness. The asymmetric tail extends out toward positive x values. (c) Distribution with negative skewness. The asymmetric tail extends toward negative x values. (d) Flat distribution with large kurtosis is called *platykurtic*. (e) Sharp distribution with small kurtosis is called *laptokurtic*. 24

2.9 Existing 2D size indexes (a) Largest diameter size. (b) Aspect ratio is defined as the height H of the aneurysm divided by its neck diameter D_1 (c) Height-width index is defined as the height H of the aneurysm divided by its largest diameter D. (d) The bottleneck factor is defined as the largest diameter D of the aneurysm divided by its neck diameter D_1. (e) Aneurysm inclination angle is defined as the angle on inclination between the aneurysm and its neck plane. 29

2.10 The centroid-radii model applied to a 2D shape. (a) The original shape. (b) The corresponding star-shape envelope with respect to centroid C. The interval between radii is fixed and the resulting distances are stored in a fixed-size vector. Shapes are compared using a vector metric. 33

3.1 Examples of the writhe number for objects with symmetry. (a) The writhe number of a cylinder is zero based on the symmetric nature of a cylinder. (b) The points on the parabola that have zero writhe numbers are shown in red. 37

3.2 The torque τ of a rigid body under the effect of two concurrent forces, $\mathbf{F_1}$ and $\mathbf{F_2}$. (a) The torque about the origin. (b) The torque about the $\mathbf{x}$ axis represents the projection of the torque about the origin on the axis. 40

4.1 Local neighborhood of surface point $\mathbf{p}$. $\mathbf{c}$ is the point on a short branch closest to $\mathbf{p}$. Most points $\mathbf{c}$ represent noise on the medial axis and sit close to the true medial axis of the normal vessels. The local neighborhood of $\mathbf{p}$ is build around $\mathbf{c}$ and is defined as the connected set of surface points whose Euclidean distance is within $R\sqrt{2}$ from $\mathbf{c}$ (a) $\mathbf{p}$ is a point on the surface of normal vessels and $\mathbf{c}$ is a noise point on the medial axis sitting close to the true medial axis of the region. (b) Detail of local neighborhood on healthy vessels. (c) $\mathbf{p}$ belongs to an aneurysm. 45

4.2 Images of vasculature obtained using different modalities. (a) 3D-RA axial image (window 1000, level -200) displays high contrast between vasculature and surrounding tissue. (b) MRA axial image (window 150, level 125). A contrast agent is used to enhance the vessels. (c) CTA axial image (window 700, level 250). The contrast agent injected during CTA imaging increases the image contrast between vessels and surrounding soft tissue, but lowers the contrast between vessels and bone. 49

4.3 Histogram of line fitting errors. 51

4.4 Histogram of plane fitting errors. 52

4.5 Histogram of parabola fitting errors. 53

4.6 FROC analysis of the aneurysm detection algorithm on 3D-RA, MRA and CTA data. The figure shows how many false positive results are observed on average before one aneurysm is detected for 3D-RA, MRA and CTA. 56

4.7 Relationship between the writhe number and region index. The total writhe number of a positive region is computed as the sum of writhe numbers of all individual surface points. True positives are shown as red stars and false positives are shown as blue stars. The analysis is done on the ten 3D-RA datasets. 57

4.8 Aneurysm detection results on one patient study. (a) Original 3d-rotational angiography. (b) Corresponding medial axis of the 3D-RA dataset. (c) Detection results. Positive results are colored in red. Black arrows point to true positives. 58

4.9 Aneurysm detection on six patient-derived datasets. Results shown after thresholding positive results with a region index of 5. Positive results are colored in red. The white arrow points to true positive. Orientation is chosen for the best visualization of the aneurysms. (a-c) 3D-RA data. (d-f) MRA data. (g-i) CTA data 59

5.1 Aneurysm surfaces are analyzed both completely isolated from parent vessels and taking into account a portion of their adjacent vessels. They are represented as triangular meshes. Both bifurcation and sidewall aneurysms are considered. The top row shows isolated aneurysms. The bottom row shows the aneurysm attached to its corresponding parent vessels. 65

5.2 Segmentation and isolation of aneurysms. (a) Original 3D-RA data. (b) Cerebral vessels are segmented from surrounding tissue. (c) Segmented vessels are represented as a triangular mesh. (d) The aneurysm is separated from the vasculature and part of the adjacent parent vessels is included. (e) The aneurysm sac is completely separated from its parent vessels. 67

5.3 Isolation of the aneurysm geometry from the segmented vasculature (a) Cutting planes at parent vessels are selected and shown in dash lines. (b) The aneurysm is cut in such a way that its neck and a portion of the adjacent vessels are included in the model. Each parent vessel is cut at a distance approximately equal to its diameter D. (c) Cutting plane at the neck of the aneurysm is selected and shown in dash line. (d) The aneurysm sac is completely isolated from all surrounding vessels. 67

5.4 Sensitivity of the classification to cutting plane definition. Four aneurysms with parent vessels attached were cut using 3 different planes per parent vessel cut. (a) Sidewall aneurysm. Cutting planes options are shown in black. Combining the cutting planes result in 9 models. (b) SW ruptured: outermost planes used. (c) SW ruptured: innermost planes used. (d) SW unruptured: outermost planes used. (e) SW unruptured: innermost planes used.(f) Bifurcation aneurysm. Cutting planes options are shown in black. Combining the cutting planes result in 27 models. (g) BF ruptured: outermost planes used. (h) BF ruptured: innermost planes used. (i) BF unruptured: outermost planes used. (j) BF unruptured: innermost planes used. 76

5.5 Analysis results on four representative unruptured SIDEWALL aneurysms. The results are shown on aneurysm dome models. (a),(b),(e),(f) Unruptured aneurysms. Writhe number values along the surface. Low values are interpreted as low surface tension. (c),(d),(g),(h) Corresponding histograms. The approximating probability distribution is shown in red. Unruptured aneurysms have sharp writhe number distributions, low entropy and low skewness. 83

5.6 Analysis results on four representative ruptured SIDEWALL aneurysms. The results are shown on aneurysm dome models. (a),(b),(e),(f) Ruptured aneurysms. Writhe number values along the surface. High values are interpreted as high surface tension and are a predictor for rupture. (c),(d),(g),(h) Corresponding histograms. The approximating probability distribution is shown in red. Ruptured aneurysms have more spread writhe number distributions, high entropy and high skewness. 84

5.7 Analysis results on four representative unruptured BIFURCATION aneurysms. The results are illustrated on aneurysms with adjacent parent vessels attached. (a),(b),(e),(f) Unruptured aneurysms. Writhe number values along the surface. Low values are interpreted as low surface tension. (c),(d),(g),(h) Corresponding histograms. The approximating probability distribution is shown in red. Unruptured aneurysms have sharp writhe number distributions, low entropy and low skewness. 85

5.8 Analysis results on four representative ruptured BIFURCATION aneurysms. The results are illustrated on aneurysms with adjacent parent vessels attached. (a),(b),(e),(f) Ruptured aneurysms. Writhe number values along the surface. High values are interpreted as high surface tension and are a predictor for rupture. (c),(d),(g),(h) Corresponding histograms. The approximating probability distribution is shown in red. Ruptured aneurysms have more spread writhe number distributions, high entropy and high skewness. 86

5.9 Analyze how the writhe number captures changes in the size of the angle between aneurysm and parent vessel. (a) The aneurysm makes a 90 degrees angle with its parent vessel. (b) The aneurysm makes a 70 degrees angle with its parent vessel. (c), (d) Corresponding histograms. It is apparent from both the writhe number values along the aneurysm surface and the corresponding histograms that the writhe number is proportional with deviations from the 90 degree angle. 87

5.10 Analyze how the writhe number captures changes in the size of the aneurysm height and the width neck as reflected by the aspect ratio index. (a) The aneurysm has an aspect ratio of 15. (b) The aneurysm has an aspect ratio of 27.5. (c), (d) Corresponding histograms. It is apparent from both the writhe number values along the aneurysm surface and the corresponding histograms that the writhe number is proportional with the change in aspect ratio. 88

5.11 Analyze the relation between the writhe number and the aneurysm hight-width ratio (HW). (a) HW = 1.6 (b) HW = 3.6 (c), (d) Corresponding histograms. (e) HW = 1.6 and the inclination angle = 110 degrees. (f) HW = 3.6 and the inclination angle = 110 degrees. (g), (h) Corresponding histograms. It is apparent from both the writhe number values along the aneurysm surface and the corresponding histograms that the writhe number is inverse proportional with the change in HW. This correlation is true even when the angle between the aneurysm and the parent vessel changes. 89

6.1 Analysis results based on the centroid-radii model on four representative unruptured SIDEWALL aneurysms. The results are shown on aneurysm dome models. (a),(b),(e),(f) Unruptured aneurysms. (c),(d),(g),(h) Corresponding histograms. The approximating probability distribution of centroid-radii distances is shown in red. Unruptured aneurysms have sharp centroid-radii distributions, low entropy and low variance. 102

6.2 Analysis results based on the centroid-radii model on four representative ruptured SIDEWALL aneurysms. The results are shown on aneurysm dome models. (a),(b),(e),(f) Ruptured aneurysms. (c),(d),(g),(h) Corresponding histograms. The approximating probability distribution is shown in red. Ruptured aneurysms have more spread centroid-radii distributions, high entropy and high variance. 103

6.3 Analysis results based on mean curvature statistics on four representative unruptured BIFURCATION aneurysms. The results are illustrated on aneurysms with adjacent parent vessels attached. (a),(b),(e),(f) Unruptured aneurysms. Mean curvature values along the surface. (c),(d),(g),(h) Corresponding histograms. The approximating probability distribution is shown in red. Mean curvature distribution for unruptured aneurysms have lower entropy, variance, skewness and kurtosis compared with ruptured aneurysms. 104

6.4 Analysis results based on mean curvature statistics on four representative ruptured BIFURCATION aneurysms. The results are illustrated on aneurysms with adjacent parent vessels attached. (a),(b),(e),(f) Ruptured aneurysms. Mean curvature values along the surface. (c),(d),(g),(h) Corresponding histograms. The approximating probability distribution is shown in red. Mean curvature distribution for ruptured aneurysms have higher entropy, variance, skewness and kurtosis compared with unruptured aneurysms. 105

6.5 Centroid-radii model analysis on four synthetic models. (a),(b),(e),(f) Centroid-radii distance values along the surface of the models. (c),(d),(g),(h) Corresponding histograms. Models entropy values increase from (c) to (h). Higher entropy values are associated with rupture. 106

A.1 Computing the writhe number of a cylinder. 111

A.2 Computing the writhe number of an extruded parabola. 113

List of Tables

4.1 Statistics for aneurysm detection on 3D-RA. 54

4.2 Statistics for aneurysm detection on MRA. 54

4.3 Statistics for aneurysm detection on CTA. 54

4.4 Performance comparison with existing detection methods on MRA data. 57

5.1 Aneurysms are classified according to their location. N is the number of aneurysms in each class. The mean value of the largest diameter size is presented for each class with the associated standard deviation. 64

5.2 The number of ruptured and unruptured aneurysms in the whole database (SW+BF), and in sidewall (SW) and bifurcation (BF) subsets. 64

5.3 Accuracy of rupture prediction when aspect ratio (AR), largest diameter size, height-width and aneurysm angle are used. The prediction is performed on three aneurysms sets: (1) 117 sidewall and bifurcation (SW+BF) aneurysms, (2) 58 sidewall (SW) aneurysms and (3) 59 bifurcation (BF) aneurysms 72

5.4 Accuracy of rupture prediction when writhe number statistics are used. The prediction is performed on three aneurysms sets: (1) 117 sidewall and bifurcation (SW+BF) aneurysms, (2) 58 sidewall (SW) aneurysms and (3) 59 bifurcation (BF) aneurysms. For each set, rupture status is predicted by considering first only aneurysm model (AM) features, second considering only parent vessel model (PVM) features, and third considering both AM and PVM features. The set of features taken into account for each particular classification case are marked with an X. Sequential backward selection is applied to determine best features set. 73

5.5 Accuracy of rupture prediction when writhe number values are used together with the other size and shape indexes. The prediction is performed on the sidewall and bifurcation aneurysms sets. For each set, rupture status is predicted by considering writhe number aneurysm model (AM) features, writhe number parent vessel model (PVM) features, and the set of 11 size and shape indexes. The set of features taken into account for each particular classification case are marked with an X. Sequential backward selection is applied to determine best features set. 74

5.6 Sensitivity of the classification to segmentation. The two segmentation methods used are region-growing thresholding and level sets. The study involves four classification cases: two in which the training and the testing sets are segmented using the same method, and two in which the training and the testing sets are segmented using different methods. 75

5.7 Sensitivity of the classification to cutting plane definition. Four aneurysms with parent vessels attached were cut using 3 different planes per parent vessel. N represents the resulting number of models for each aneurysm. The models are classified according to their type (SW or BF). 77

6.1 Accuracy of rupture prediction when centroid-radii statistics are used. The prediction is performed on three aneurysms sets: (1) 117 sidewall and bifurcation (SW+BF) aneurysms, (2) 58 sidewall (SW) aneurysms and (3) 59 bifurcation (BF) aneurysms. Rupture status is predicted by considering only aneurysm model (AM) features. Sequential backward selection is applied to determine best features set. 95

6.2 Accuracy of rupture prediction when centroid-radii statistics are used. The prediction is performed on three aneurysms sets: (1) 117 sidewall and bifurcation (SW+BF) aneurysms, (2) 58 sidewall (SW) aneurysms and (3) 59 bifurcation (BF) aneurysms. Rupture status is predicted by considering only aneurysm model (AM) features. Sequential backward selection is applied to determine best features set. 95

6.3 Accuracy of rupture prediction when all size and shape aneurysm attributes are taken into account: curvature statistics, centroid-radii model statistics(CR-M), writhe number statistics and the 11 established size and shape indexes. The prediction is performed on the sidewall and bifurcation aneurysms sets. The statistical model takes into account both aneurysm model (AM) features and parent vessel model (PVM) features. The set of features taken into account for each particular classification case are marked with an X. Sequential backward selection is applied to determine best features set. 96

6.4 Sensitivity of the classification based on centroid-radii model to segmentation. The study involves only sidewall aneurysms and takes into account features derived from aneurysm models (AM) only. The two segmentation methods used are region-growing thresholding and level sets. The study involves four classification cases: two in which the training and the testing sets are segmented using the same method, and two in which the training and the testing sets are segmented using different methods. 98

6.5 Sensitivity of the classification based on surface curvature to segmentation. The study involves only sidewall aneurysms and takes into account features derived from aneurysm models (AM) only. The two segmentation methods used are region-growing thresholding and level sets. The study involves four classification cases: two in which the training and the testing sets are segmented using the same method, and two in which the training and the testing sets are segmented using different methods. 98

6.6 Sensitivity of the classification to cutting plane definition. Four aneurysms with parent vessels attached were cut using 3 different planes per parent vessel. N represents the resulting number of models for each aneurysm. The models are classified according to their type (SW or BF). 99

Chapter 1

Introduction

An intracranial cerebral aneurysm is a localized pathological dilatation of a blood vessel in the brain. The origin, formation and evolution of cerebral aneurysms are still not completely understood. It is clear that there is not one single factor involved in aneurysmal development, but rather multiple risk factors which determine their growth and eventual rupture [WBHT06]. Ruptured aneurysms may lead to subarachnoid hemorrhage (SAH), a severe condition associated with high mortality and morbidity. SAH is a form of stroke, with the main symptoms being severe headache with rapid onset, vomiting, fever, and mild confusion [EMO08]. It is estimated that 10 to 15% of patients with SAH die before reaching the hospital [vGKR07]. SAH is a medical emergency and prompt diagnosis and treatment are essential in improving patient outcomes.

The diagnosis and management of SAH represents a challenge to emergency physicians, neuroradiologists, neurologists and neurosurgeons. Detecting symptomatic intracranial aneurysms from imaging scans is an essential step in the prevention of aneurysmal SAH and its attendant complications [WW00], as treatment of aneurysms using endovascular or surgical methods carries a lower rate of complication when performed in unruptured versus ruptured aneurysms [BSN06].

While a severe condition, SAH accounts for only 5% of all strokes and only a small fraction of all existing aneurysms progress to SAH. Recent studies suggest that 6% of the general population may harbor unruptured cerebral aneurysms [LeBB09, WBHT06]. These are asymptomatic aneurysms, the majority of which remains undetected and are not a medical concern. However, advancement in imaging technologies has led to an increased detection of these incidental, asymptomatic unruptured intracranial aneurysms (UIA) during the routine evaluation of headache patients in Emergency Department settings [WBHT06, KW07]. Once discovered, the management of these asymptomatic UAI is controversial [WW00, Wie05, Wei05]. It is not always obvious which particular aneurysmal lesions carry a rupture risk significant enough to warrant intervention [ZD04]. Recent studies estimate the annual rupture rate of a prospectively monitored patient population at only 0.1-0.2% [Wie03], so the relative low risk of rupture of incidental asymptomatic UIA needs to be balanced against the risks of complications carried by preventive treatment options.

This work investigates the two major areas of intracranial aneurysms analysis - aneurysms detection and rupture status classification. The *writhe number* is introduced as a novel 3D shape feature, which proves useful in both detection and classification studies. As such our contribution is twofold. First, we concentrate on our theoretical contribution by introducing the writhe number as a new 3D descriptor used to characterize surfaces. Known in curve theory since its introduction by Fuller in 1971 [Ful71], the writhe number is used to describe the global geometry of a closed space curve or knot [AEW04, BP06]. To the best of our knowledge, this research represents the first time the writhe number has been extended to surfaces. Second, writhe number-based methods are developed for both automatic aneurysm detection and rupture status classification. Our experiments support the usefulness of the writhe number aneurysm shape analysis as a 3D shape descriptor

with potential clinical use in both detection and rupture risk stratification. In addition to the writhe number, 3D shape descriptors based on surface curvature [Blo97] and centroid-radii model [TOT00, Fan01] are proposed and investigated for rupture classification. The Gaussian and mean curvatures are evaluated to describe local changes on the surface of the aneurysms. In the centroid-radii model, the distances between the centroid and the boundary of the aneurysms are computed in all directions. The resulting distribution of unnormalized distances describes both the size and the shape of the aneurysms. The combined use of these shape descriptors yields very promising results for predicting rupture status in intracranial aneurysms.

1.1 Overview of Automatic Detection

The detection of brain aneurysms plays a key role in reducing the incidence of intracranial subarachnoid hemorrhage (SAH) which carries a high rate of morbidity and mortality. The majority of non-traumatic SAH cases are caused by ruptured intracranial aneurysms. Accurate detection can decrease a significant proportion of misdiagnosed cases. Although aneurysm detection is currently performed visually by experienced diagnosticians, there is an increasing interest in computed-aided systems to assist clinicians, improve diagnostic accuracy and limit missed detection.

Existing aneurysm detection methods focus on magnetic resonance angiography (MRA) data and are usually two-step processes [ALK$^+$04, UAY$^+$05, KKH06]. First, potential regions of interest (potential aneurysms) are detected from the input 3D volume. Most detection methods start by searching for dot-like structures on the segmented vasculature. This is performed by pre-processing the data and using dot-enhancement filters [ALK$^+$04], and/or by analyzing and comparing the geometry of the vessels with a prior normal vessels model [KKH06]. This first step typically returns a large number of possible aneurysmal regions, requiring the use

of a false positive reduction scheme based on region properties such as image intensity, shape, size, and relative position in the input volume. The complexity of the false positive reduction scheme depends on the specificity of the detection method used in the first step. Detection algorithms which return a large number of possible aneurysmal regions after the first step, rely on the false positive reduction method to prune the results and as such may require a more complex reduction scheme. In comparison, algorithms which discriminate well between aneurysmal lesions and healthy vessels during the first detection step may require a less complex false positive reduction scheme.

A scheme for automated detection of intracranial aneurysms is proposed in this study [LMFM09]. The method detects aneurysms as suspect regions on the vascular tree, and is designed to assist diagnosticians with their interpretations and thus reduce missed detections. In the current approach, the vessels are segmented from background and surrounding brain tissue and their medial axis is computed, where the medial axis is defined as the shape skeleton or centerline. Normal healthy vessels are modeled as tubular structures. Using the medial axis as a positional guidance, small regions along the vessels are inspected and the writhe number is used to quantify how closely any given region approximates a tubular structure. Aneurysms are detected as non-tubular regions of the vascular tree with non-zero writhe numbers. Once the suspected aneurysmal regions are highlighted, the method uses a size-based false positive reduction scheme in which small regions are eliminated from positive results. The detection method is tested on 3D-RA, MRA and CTA patient data. Free-response operator characteristic (FROC) analysis is applied to evaluate the performance of the proposed detection system.

The aneurysm detection method is tested on thirty unrelated patient datasets, ten of each imaging modality: 3D-rotational angiography (3D-RA), magnetic resonance angiography (MRA), and computed tomography angiography (CTA). In our

experiments, 100% sensitivity was achieved with false positives rates as low as 0.66 per study on 3D-RA data, 5.7 false positive rates per study on MRA data and 5.36 false positive rates per study on CTA data. The detection performance on 3D-RA data, with high sensitivity and very few false positives, provides an initial proof of concept of our processing scheme and supports the theoretical value of the algorithm.

There is a direct relationship between the quality of vessel segmentation and the accuracy of the detection method. 3D-RA data has high resolution, shows high contrast between vasculature and surrounding tissue, and displays high signal-to-noise ratio. Consequently, simple segmentation techniques yield good results on 3D-RA data. Segmentation is more challenging on MRA and CTA data which have lower resolution and more artifacts. The performance of the proposed method is comparable to that of existing methods on MRA data and will be discussed in more detail in Chapter 4.

The ultimate clinical goal of this detection research is to offer an added safety net to the diagnostician and to the patient, by making available a concordance check protocol that would point the clinician to potential areas of concern that may have been missed by the current method of visual inspection. The added value of such a tool will need to be evaluated by prospective clinical trials.

1.2 Overview of Rupture Status Classification

Recent innovations in non-invasive vascular imaging have increased the detection of incidental aneurysms, and created a need for aneurysm rupture risk stratification tools to help guide the treatment of these asymptomatic lesions. Studies suggests that at least 2% of the general population harbors aneurysms [RDAvG98]. Most of these asymptomatic aneurysms will never rupture, but their incidental detection

during routine evaluations raises ethical and medical questions about the best management strategies for these lesions.

Usually the clinical decision to treat is based on 2D geometrical features such as aneurysm size [oUIAI98, Wie03], aspect ratio (aneurysm height/neck width) [UTH+99, DTM+08, LeBB09] and height-width ratio [DTM+08]. However, many large aneurysms appear stable and, conversely, small aneurysms often present with rupture [JPP00, RMH05, NDM+05]. This incongruence has thrust morphological analysis as a possible differentiator of rupture likelihood in cerebral aneurysms. Some of the first morphological features proposed to characterize the 3D geometry of an aneurysm are global descriptors such as undulation, non-sphericity and ellipticity indexes [MHR04, RMH05, HSF+07, DTM+08]. More complex 3D features based on Fourier analysis [RLB+05], and geometrical and Zernike moments [MDMP+07] have also been investigated. Initial results showed the potential of 3D shape analysis and support the idea that, like size, geometry is likely to have an impact on the rupture risk.

In this work, a novel set of morphological parameters, again based on the writhe number but now used in a significantly different manner [LMBM10], are introduced to describe the 3D shape of cerebral aneurysms and predict rupture status. In addition to the writhe number, 3D shape descriptors based on Gaussian and mean surface curvature, and on the centroid-radii model are proposed and investigated for rupture status classification. While the analysis of surface curvature and centroid-radii model are established evaluation methods in image processing and shape representation applications [TOT00, Fan01, HMM+03], to the best of our knowledge, this is the first time statistics derived from local curvature and distance distributions are used to predict rupture status in cerebral aneurysms.

The writhe number, surface curvature, and distance from the centroid, are defined at each point on the surface of the aneurysm. The classification procedure is

based on the analysis of measures derived from the distribution of these quantities, through the use of histogram statistics. Parameters such as central moments, cumulants and entropy of the histograms are analyzed to develop a better understanding of aneurysm shape variation as measured by the writhe number, surface curvatures and the centroid-radii model. These measures are used as classification attributes in predicting rupture status in a dataset of cerebral aneurysms.

To provide some intuition concerning the morphological utility of the writhe number of 3D surfaces, a novel analogy is proposed here between writhe number of surfaces and mechanical torque [ST06]. Under this analogy, the writhe number is viewed as a measure of how close the aneurysm is to mechanical equilibrium at each point on its surface. In other words, the writhe number measures how much ”tension” there is on the surface of the aneurysm. Intuitively, the more spread out and the stronger the ”tension” is on the surface, the greater is the likelihood for rupture.

The analysis was performed on a database of 106 patients with 117 cerebral saccular aneurysms (52 ruptured and 65 unruptured). Aneurysms were analyzed both as completely isolated lesions and including a portion of their adjacent parent vessels. The aneurysms were further labeled as sidewall (58 aneurysms) or bifurcation (59 aneurysms) according to their location with respect to the parent vessels. Previous studies do not make a distinction between analysis on sidewall and bifurcation aneurysms, but during this study it was found that sidewall and bifurcation aneurysms were best described by disjoint sets of shape parameters, yielding a morphological dichotomy between the two subtypes. This is consistent to similar research in our lab which shows that most size and shape parameters predict rupture status better on sidewall than on bifurcation aneurysms.

The morphological analysis prediction results were compared with established size and shape indexes (e.g. aspect ratio, aneurysm size, height-width, non-sphericity,

ellipticity and undulation indexes). Using these indexes resulted in 77.1% accuracy for sidewall aneurysms and 64.2% accuracy for bifurcation aneurysms. Adding morphological analysis based on writhe number analysis resulted in 86.7% prediction accuracy for sidewall and 71.2% accuracy for bifurcation aneurysms; a significant increase in prediction accuracy for both aneurysm subtypes over the established shape indexes.

In addition to the writhe number, this study also introduces the centroid-radii model and the surface curvature for shape analysis. The entropy of the centroid-radii distance distribution proved to be the most accurate single index associated with rupture in sidewall aneurysms (accuracy 80.3%). When the writhe number-based features are combined with other shape and size indexes, including surface curvature and centroid-radii model, the prediction accuracy increases even further, resulting in a stronger statistical model for rupture status prediction. More specifically, the proposed methodology resulted in a prediction accuracy of 88.4% for sidewall aneurysms (vs. 77.1% using established indexes) and 79.8% for bifurcation aneurysms (vs. 64.2% using established indexes). Rupture status analysis is discussed in detail in Chapters 5 and 6.

While the analysis was performed on a relatively large database and the results are very encouraging, the eventual added value of the method remains to be determined in the clinical setting and would require validation in prospective clinical trials.

1.3 Outline of the Thesis

This thesis is structured as follows: background information and prior work details on aneurysm detection and classification, as well as on the proposed surface analysis techniques are provided in Chapter 2. The main theoretical contribution

describing the writhe number of surfaces is introduced in Chapter 3. The automatic detection of intracranial aneurysms is presented in Chapter 4. Chapter 5 describes the proposed methodology for analyzing rupture status in intracranial aneurysms using the writhe number. Both Chapter 4 and Chapter 5 represent comprehensive presentations of the proposed methods with details about corresponding testing data, preprocessing procedures, reported results, and direction for future work. Rupture status prediction analysis is continued in Chapter 6 with details about the use of 3D descriptors derived from surface curvature and centroid-radii model. This work is concluded in Chapter 7. Proofs involving the writhe number are demonstrated in Appendix A.

Chapter 2

Background and Related Work

This chapter provides an introduction to some basic differential geometry concepts which are relevant to our use of surface curvature and writhe number. Related work regarding aneurysm detection and rupture risk prediction is also presented here.

2.1 Geometry of Curves and Surfaces

2.1.1 Curves in the Plane

A *curve* in $\Re^3$ is a piecewise-differentiable function $\alpha : I \rightarrow \Re^3$ defined on the open interval I in $\Re$. For every value $t \in I$, α is described as $\alpha(t) = (\alpha_1(t), \alpha_2(t), \alpha_3(t))$, where α_1, α_2 and α_3 are the Euclidean coordinate functions of α [Gra93, O'N06]. The function $\alpha' : I \rightarrow \Re^3$ given by $\alpha(t)' = (\alpha_1'(t), \alpha_2'(t), \alpha_3'(t))$ is called the velocity of curve. Note that ' denotes differentiation with respect to t. The magnitude of the velocity at each point gives the speed of the curve. Curve α is said to be regular if it is differentiable with non-zero velocity. The curve is said to have unit speed if its speed is constant and equal to 1 at every point. The *tangent vector* at a point on the curve is given by the velocity at that point.

Given a curve $\alpha : I \rightarrow \Re^3$ and a function $h : J \rightarrow I$ differentiable on the open

interval $J \in \Re$, then function $\beta = \alpha(h) : J \to \Re^3$ is called a parametrization of α by h. The parametrization of a curve is not unique.

To compute the length of a closed arc of a curve, let $\alpha : I \to \Re^3$ be a curve defined on the open interval I. Let $\gamma : [a, b] \to \Re^3$ be a closed arc of curve α, which means γ is defined on a closed interval $[a, b] \in I$, such that γ is defined and differentiable at both a and b. The closed arc is said to be *rectifiable* if it has finite length, which is defined as the line integral of the curve velocity $Length(\gamma) = \int_a^b \|\gamma'(t)\| dt$. The length of the closed arc does not depend on the curve parametrization. A curve is said to be rectifiable if any of its closed arcs is also rectifiable. Rectifiable curves can be parameterized using the so-called *arc length or unit speed parameterization*. If curve α has an arc length parameterization $\alpha = \alpha(t)$, then for every $t_1, t_2 \in [a, b]$, the arc length function starting at t_1 satisfies $s(t) = \int_{t_1}^{t_2} \|\alpha'(u)\| du = t_2 - t_1$. It can be proved that any rectifiable curve admits an arc length parameterization [O'N06].

2.1.2 Surfaces in 3-Dimensional Space

A coordinate patch $x : D \to \Re^3$ is a one-to-one mapping of the open set $D \in \Re^2$ into $\Re^3$. If x is defined as $x(u, v) = (u, v, f(u, v))$, where f is any differentiable real-value function on the set $D \in \Re^2$, then the image $M = x(D)$ of patch D is called a *simple surface*. Holding u or v constant in the function $(u, v) \to x(u, v)$ results in two sets of curves. For a specific point $(u_0, v_0) \in D$, the curve $u \to x(u, v_0)$ is called the *u-parameter curve* of x and the curve $v \to x(u_0, v)$ is called the *v-parameter curve* of x. Surface $M = x(D)$ is covered by these two families of curves. If curve u and v are regular curves, x is called a parametrization of the region $x(D)$ in M [Gra93, O'N06].

Patch x can be described using its Euclidean coordinate functions $x(u, v) = (x_1(u, v), x_2(u, v), x_3(u, v))$. At each point $(u_0, v_0) \in D$, the velocity vector at u_0

of the u-parameter curve is denoted $x_u(u_0, v_0)$ and the velocity vector at v_0 of the v-parameter curve is denoted $x_v(u_0, v_0)$. Functions x_u and x_v are defined as

$$x_u = \frac{\partial x}{\partial u} = \left(\frac{\partial x_1}{\partial u}, \frac{\partial x_2}{\partial u}, \frac{\partial x_3}{\partial u}\right) \tag{2.1}$$

$$x_v = \frac{\partial x}{\partial v} = \left(\frac{\partial x_1}{\partial v}, \frac{\partial x_2}{\partial v}, \frac{\partial x_3}{\partial v}\right) \tag{2.2}$$

Vectors $x_u(u_0, v_0)$ and $x_v(u_0, v_0)$ are *tangents* to surface M at point (u_0, v_0). The two vectors define the tangent plane to surface M at point (u_0, v_0). The *normal vector* to surface M at point (u_0, v_0) is given by the cross product $x_u(u_0, v_0) \times x_v(u_0, v_0)$. In general, the *unit normal vector field* or *surface normal* U of surface M is defined as

$$U(u, v) = \frac{x_u \times x_v}{\|x_u \times x_v\|}(u, v) \tag{2.3}$$

at those points $(u, v) \in D$ where $x_u \times x_v$ is non-zero [Gra93].

To compute metric properties of the surface such as arc length, surface area and surface curvature, the first and second fundamental forms are defined. The *Riemannian metric* or *the first fundamental form* is defined as

$$ds^2 = Edu^2 + 2Fdudv + Gdv^2 \tag{2.4}$$

where ds is the element of arc length, du, dv are parameterization elements, and coefficients E, F, G are defined as $E = \|x_u\|^2$, $F = x_u \cdot x_v$, and $G = \|x_v\|^2$. There is also a *second fundamental form*, which can be expressed in quadratic form as

$$II = edu^2 + 2fdudv + gdv^2 \tag{2.5}$$

where coefficients e, f, g are defined as $e = U \cdot x_{uu}$, $f = U \cdot x_{uv}$ and $g = U \cdot x_{vv}$ given $x_{uu} = \frac{\partial x_u}{\partial u}$, $x_{uv} = \frac{\partial x_u}{\partial v}$, $x_{vv} = \frac{\partial x_v}{\partial v}$.

2.1.3 Curvature

The curvature measures the extent to which a geometric object bends at each point. For a regular curve parametrized by arc length, $\alpha : (a, b) \rightarrow \Re^3$, and described as $\alpha(t) = (\alpha_1(t), \alpha_2(t), \alpha_3(t))$ with $t \in (a, b)$, the curvature is a measure of the radius of the unique circle which best approximates the curve at each point. Analytically, the curvature k of curve α can be computed from the first and second derivatives of $\alpha(t)$ as

$$k(t) = \frac{\|\alpha^{'}(t) \times \alpha^{"}(t)\|}{\|\alpha'(t)\|^3}. \tag{2.6}$$

In the case of surfaces, given a regular surface M, for each arbitrary tangent vector v_p to M at point p, a normal curvature of M in the direction v_p is defined as a function of the first and second fundamental forms

$$k(v_p) = \frac{edu^2 + 2fdudv + gdv^2}{Edu^2 + 2Fdudv + Gdv^2}. \tag{2.7}$$

The minimum k_{min} and maximum k_{max} values of the normal curvature k of M at p computed over all possible directions, are called principal curvatures. The unit vectors at which these values occur are called principal directions [Gra93]. To describe geometric and topological surface properties, the Gaussian (K_g), and mean (K_m) curvatures are defined as functions of the principal curvatures.

$$K_g = k_{min}k_{max} \tag{2.8}$$

$$K_m = \frac{[k_{min} + k_{max}]}{2} \tag{2.9}$$

In practice, the Gaussian and mean curvature can be computed directly from the

coefficients of the first and second fundamental forms [Gra93].

$$K_g = \frac{eg - f^2}{EG - F^2} \tag{2.10}$$

$$K_m = \frac{eG - 2fF + gE}{2(EG - F^2)}. \tag{2.11}$$

Intuitively, a flat piece of paper can only be bent in one direction, such that at any point on the surface there is a straight line in at least one direction. This means that the minimum curvature along the surface of the paper is zero regardless of whether the paper lies flat or is bent into a cylinder or a cone. Consequently, the Gaussian curvature of a cylinder or a cone is zero, equal to the Gaussian curvature of a plane. Similarly, the skin of a sphere can never be completely flattened into a plane without distortion. This phenomenon has to do with the intrinsic geometry of surfaces.

The intrinsic geometry describes properties dependent on surface alone, without considering the space around them. The Gaussian curvature is an intrinsic geometric property of the surface which describes mathematically if one surface can or cannot be bent into another. The study of curved surfaces and their intrinsic properties are the topics of Riemannian geometry [Gra93]. In contrast, the mean curvature is an extrinsic measure of curvature, describing the local curvature by taking the surrounding space into account. As such, the mean curvature captures notions such as the inside and the outside of the geometric object.

As shown in Fig. 2.1, regions with positive Gaussian curvature represent elliptical patches, which have positive mean curvature if they are locally convex and negative mean curvature if they are locally concave. As illustrated in Fig. 2.2, regions with negative Gaussian curvature represent hyperbolic patches, in which one of the principal curvatures is positive and the other is negative. Points with zero Gaussian curvature are either parabolic (one of the principal curvatures is zero) or

planar (both principal curvatures are zero) [HL93]. Figure 2.3 illustrates the differences between Gaussian and mean curvature on a more complex surface, where the Gaussian curvature differentiates between elliptic and saddle points, while the mean curvature further differentiates the elliptic points into convex or concave.

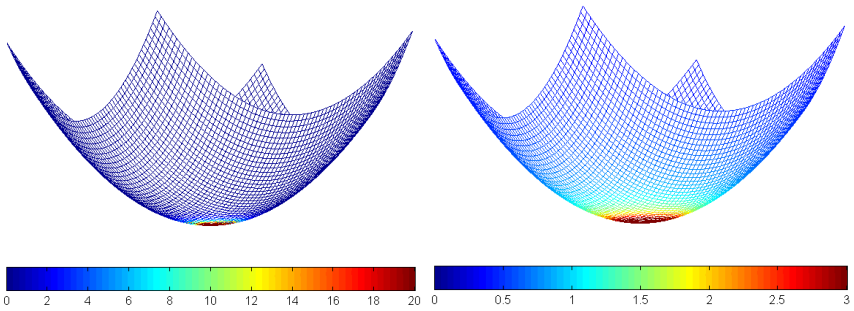

(a) (b)

Figure 2.1: Illustration of the curvature of elliptical surfaces. (a) The Gaussian curvature of an elliptical surface is positive. (b) The mean curvature of an elliptical surface is positive if the surface is locally convex and negative if the surface is locally concave.

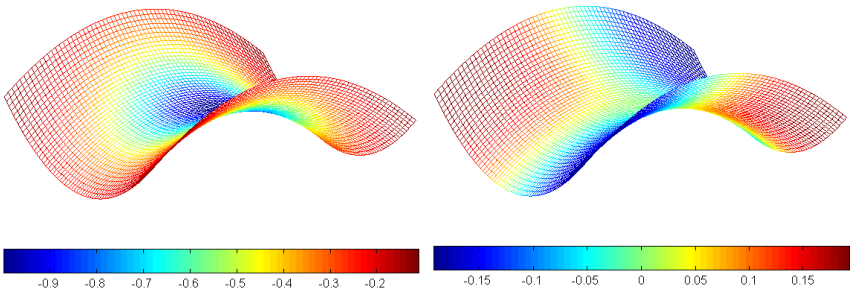

(a) (b)

Figure 2.2: Illustration of the curvature of hyperbolic surfaces. (a) The Gaussian curvature of a hyperbolic surface is negative. (b) The mean curvature of a hyperbolic surface has both zero and non-zero values.

Many computer vision applications that make use of input data composed of triangular meshes require an estimate of local surface curvature. However, curvature is a continuous function of local surface behavior and triangle meshes are a discrete approximation of a continuous surface that are only C^0 continuous at triangle edges.

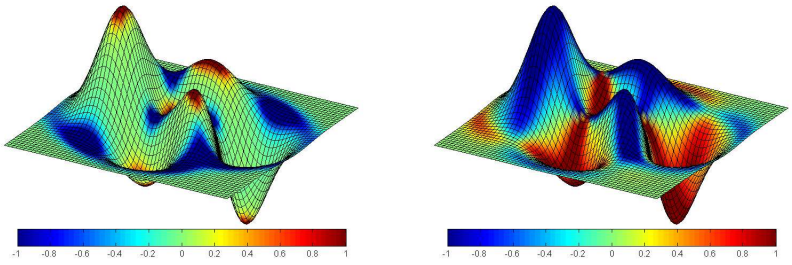

(a) (b)

Figure 2.3: Gaussian and mean curvature of a more complex surface. (a) Gaussian curvature capture intrinsic geometric properties, i.e., whether a region is elliptical or hyperbolic. (b) mean curvature captures extrinsic geometric properties, i.e., whether an elliptical region is convex or concave.

Thus, estimating the curvature of a triangle mesh is an ongoing research problem.

Strategies for estimating surface curvature on meshes fall in one of three major categories [GG06]. In the first category, the mesh around the vertex of interest is locally approximated as a continuous, typically quadratic, parametric surface patch [SW92, Ham93]. The curvature is determined by evaluating second order derivatives from the parametric surface patch. However, this parametric approximation does not guarantee that the vertex of interest sits on the parametric surface patch. Thus, constraints can be used to guarantee that specific points are part of the resulting parametrization.

In the second category, curvature is approximated directly from the discrete mesh, using only mesh connectivity information [MW00, DHKL01]. However, the resulting curvature tends to be sensitive to noise and mesh resolution. Therefore, a smoothing technique is applied to either the initial mesh or to the resulting curvature field by averaging values over a small neighborhood.

In the third category, methods employ tensor evaluation directly on the mesh. Tensors are mathematical concepts used to generalize algebraic notions such as scalars, vectors and matrices. In the context of 3D surfaces, tensors describe a

particular relationship between two vectors, thereby acting as maps transforming one vector into another. In particular, a curvature tensor associates a point on the 3D surface to its corresponding principal curvatures. Using this approach, regions on the mesh are locally associated with tensors, which converge to the theoretically curvature tensor map of the smooth surface [Tau95, CSM03b, ACSD$^+$03]. See [GG06, MSR07] for a in-depth survey and accuracy comparison of the most recent research in curvature estimation.

In this work, curvature estimation is performed using tensor evaluation, based on the work described in [CSM03b, ACSD$^+$03]. The method relies on the theory of normal cycles [CSM03a, Mor08] to provide a way to define curvature for both smooth and polyhedral surfaces. Given a surface represented as a polyhedron P, a normal cycle of the surface associates particular offsets around the polyhedron in the direction of the unit normal field of P. If the polyhedron is closely inscribed in the offset manifold, with offsets bounded by some small positive constant ϵ, than a curvature measure of the polyhedron can be recovered from its normal cycle [CSM03b]. It can be proved that under certain continuity and differentiability conditions, the normal cycle of P exists and is unique [Mor08]. Figure 2.1.3 shows a tubular neighborhood $N_\epsilon(P)$ of a convex polygon P, defined as $N_\epsilon(P) = \{x \in \Re^n | dist(x, P) \leq \epsilon\}$, n = 2,3.

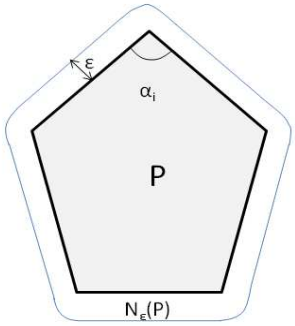

Figure 2.4: A tubular neighborhood of a polygon P, represented as an offset manifold in the direction of the unit normal field of P. The offset distance is bounded by constant ϵ.

For a convex polyhedron, the volume of the offset is a function of the mean and Gaussian curvatures at each vertex of P. The volume is given by the formula

$$Vol_\epsilon(P) = \epsilon Area(P) + \frac{1}{2}\epsilon^2 \int_{v\in P} K_m dv + \frac{1}{3}\epsilon^3 \int_{v\in P} K_g dv. \tag{2.12}$$

When instead of the whole volume, only a neighborhood B surrounding a vertex $v \in P$ is considered, $B \in N_\epsilon(P)$, the volume of B is given by

$$Vol_\epsilon(B) = \epsilon Area(B) + \frac{1}{2}\epsilon^2 \int_{v\in B\cap P} K_m dv + \frac{1}{3}\epsilon^3 \int_{v\in B\cap P} K_g dv. \tag{2.13}$$

In the non-convex case, normal cycles are decomposed into the convex components of the offset, which are each classified as spherical, cylindrical and planar parts. It is proved in [CSM03b] that, for both convex and non-convex cases, the discrete Gaussian curvature associated with neighborhood B is a function of the angle defect of P at vertices $v \in B \cap P$. The angle defect is defined as 2π minus the sum of angles between consecutive edges incident on v. Similarly, the discrete mean curvature is a function of the angles between incident faces, weighted by the length of their edges in B. To capture these measurements, a piecewise linear curvature tensor field, defined as 3x3 symmetrical bilinear forms, is built over the polyhedron P. The curvature tensor is estimated at each vertex over a neighborhood B and estimated tensor values are interpolated linearly across adjacent triangles. Given a vertex $v \in P$, the curvature tensor at v is defined as

$$T(v) = \frac{1}{|B|}\sum_{e\in B} \beta(e)|e \cap B|\overline{e}\overline{e}^t \tag{2.14}$$

where, as shown in Fig. 2.5, B is a neighborhood surrounding vertex v, e is an edge

of the mesh, $\beta(e)$ is the signed angle between the normals of the two oriented triangles incident to e, $|e \cap B|$ is the length of $e \cap B$ (between 0 and $|e|$) and $\bar{e}$ is a the unit vector in the same direction as e [ACSD+03]. According to the theory developed in [CSM03b], $T(v)$ is a 3x3 matrix whose sorted eigenvalues are associated with the normal at v, and with the minimum (k_{min}) and maximum (k_{max}) curvatures at v, respectively. Given the principal curvatures, the Gaussian ($K_g = k_{min}k_{max}$) and mean ($K_m = [k_{min} + k_{max}]/2$) curvatures are also computed for each vertex along the surface.

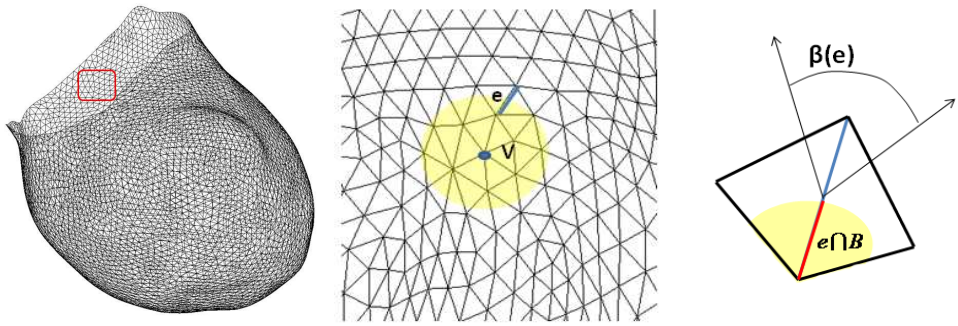

(a) (b) (c)

Figure 2.5: Computing the curvature on aneurysms represented as triangular meshes. (a) Complete model of an aneurysm represented as a triangular mesh. (b) Detail on the mesh. The yellow disk surrounding vertex v represents the neighborhood B over which the curvature at v is computed. (c) The angle between a pair of adjacent faces sharing an edge e is computed as the angle between the normals at the two triangles. $|e \cap B|$ is the length of $e \cap B$ (between 0 and $|e|$).

While other studies [MHR04, RMH05] have investigated curvature-based indexes for aneurysm surface analysis, they use only global measures of curvature. For example, [MHR04] introduces four global shape indices based on Gaussian and mean curvature: area-averaged Gaussian (GAA), area-averaged mean (MAA),

L2-norm of Gaussian (GLN) and L2-norm of the mean (MLN).

$$GAA = \sum_{\triangle_i} K_{gi} S_i / \sum_{\triangle_i} S_i \tag{2.15}$$

$$MAA = \sum_{\triangle_i} K_{mi} S_i / \sum_{\triangle_i} S_i \tag{2.16}$$

$$GLN = \frac{1}{4\pi} \sqrt{\sum_{\triangle_i} K_{gi}^2 S_i \sum_{\triangle_i} S_i} \tag{2.17}$$

$$MLN = \frac{1}{4\pi} \sqrt{\sum_{\triangle_i} K_{mi}^2 S_i}, \tag{2.18}$$

where K_{gi}, K_{mi} and S_i are the Gaussian curvature, the mean curvature and the surface area associated with the *i*th triangular element of the triangle mesh model of the aneurysm [MHR04]. GAA and MAA have units of inverse distance [L^{-2}] and [L^{-1}] respectively, and therefore depends on the size as well as the shape of the aneurysm. GLN and MLN are both non-dimensional and depend on surface shape only [MHR04].

This thesis presents a set of new curvature-based shape descriptors for aneurysm rupture status classification that go beyond the global curvature-based shape descriptors of prior art which fail to capture subtle shape differences. The new shape descriptors include variance, skewness, kurtosis, and entropy of surface curvature distributions. Details about the use and the performance of these new curvature-based shape descriptors for aneurysm rupture classification are provided in Chapter 6.

2.1.4 Writhe Number

The introduction of the writhe number as a novel 3D surface descriptor is a main theoretical contribution of this research. The writhe number was introduced by Fuller in 1971 [Ful71] and is used in curve theory to measure how much a curve twists and coils. When a second curve is placed nearly parallel to the first one, the

writhe number measures how much the second curve twists about the first [BP06]. While the application of the writhe number is usually confined to closed ribbons, formulas for open ended curves were introduced in [Sta05, BP06]. In biomedical engineering, the writhe number is used to study the shape and topology of DNA [KL00, RM03] and to characterize the shape of curves on 3D surfaces, such as the curves of sulci and gyri on the cortical surface [HGLS08].

Let C be a closed non-self-intersecting smooth curve $C = r(s) : [0, L] \rightarrow \Re^3$, parameterized by arclength s. It is assumed C has a natural orientation following the direction of the arc coordinate [Sta05]. A two-dimensional unit sphere S^2 is used to represent the family of parallel projections in $\Re^3$. The projection of C in a direction $z \in S^2$ is an oriented, possibly self-intersecting, closed curve in a plane normal to z. The directional writhe number of C in the direction of z, denoted $Dw(z)$, is defined as the number of positive crossings minus the number of negative crossings [AEW04]. As shown in Fig. 2.6, a crossing is considered positive if, in order to align two curve intervals, the upper interval is rotated counterclockwise with an angle between 0 and π. A crossing is considered negative if, in order to align two curve intervals, the upper interval is rotated clockwise with an angle between 0 and π. The total writhe number of C is the averaged directional writhe number taken over all directions $z \in S^2$.

$$W_r(C) = \frac{1}{4\Pi} \sum_{z \in S^2} Dw(z) \tag{2.19}$$

Alternatively, the writhe number W_r can be computed from the tangents to the curve as the double line integral:

$$W_r(C) = \frac{1}{4\Pi} \int_0^L \int_0^L \frac{(r(s_1) - r(s_2)) \bullet (t(s_1) \times t(s_2))}{\|r(s_1) - r(s_2)\|^3} ds_1 ds_2, \tag{2.20}$$

where s_1, s_2 are arclengths and $t = r^{'}(s)$ is the tangent vector. Here $\|\cdot\|$ is the norm

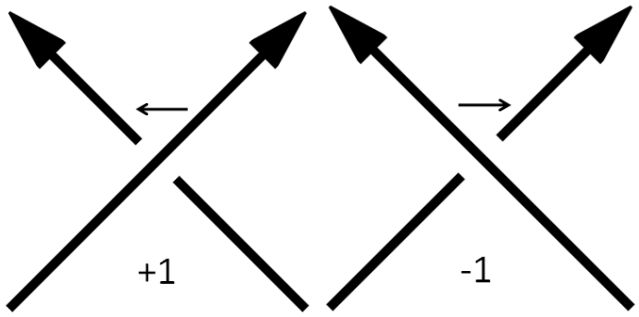

(a) (b)

Figure 2.6: (a) A curve crossing is considered positive if, in order to align two curve intervals, the upper interval is rotated counterclockwise with an angle between 0 and π. (b) A curve crossing is considered negative if, in order to align two curve intervals, the upper interval is rotated clockwise with an angle between 0 and π.

of a vector, $\bullet$ denotes a dot product and $\times$ denotes a cross product. Note that the writhe number depends exclusively on the shape of curve C and it is independent of the direction of C. The writhe number is a signed integer, measuring the number of crossings of the curve with itself, averaged over all possible projection angles [Sta05, BP06]. Figure 2.7 shows the trefoil knot curve. The knot has a writhe number of 3.

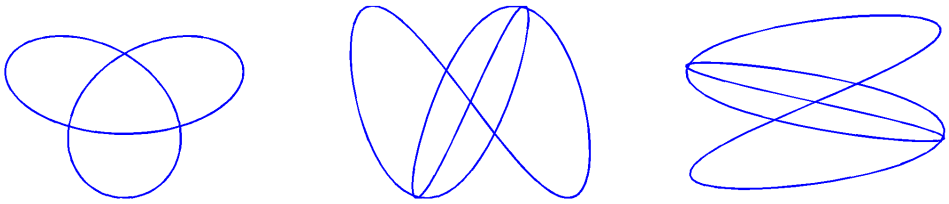

(a) (b) (c)

Figure 2.7: The trefoil knot curve has 3 crossings and a writhe number of 3. (a) 3D view along x axis. (b) 3D view along the y axis. (c) 3D view along the z axis.

This research extends the use of the writhe number from 2D to 3D. The theory behind the writhe number of curves and 3D surfaces and the geometric properties of the writhe number of surfaces are discussed in detail in the next chapter. The usefulness of the writhe number for both detection and classification of intracranial

aneurysms is presented in Chapter 4 and Chapter 5, respectively.

2.2 Probability and Statistics

Quantitative histogram analysis through use of statistics, such as central moments, cumulants and entropy, has been successfully used in biomedical imaging research for classification and pattern recognition applications [APT+07, YM06, SJY+09, CGR08, SUS09, SCH06].

In this thesis, shape descriptors such as the writhe number and surface curvatures are computed over the surface of an aneurysm model and are treated as samples of continuous density functions, which can be captured and analyzed using histograms. A histogram is a non-smooth estimator of the underlying density function showing discontinuities at its ends and at bins with zero value [MSW00, Wil97]. Because, such discontinuities may not reflect the continuous nature of the density function, histogram smoothing is performed using kernel estimators.

Kernel smoothing approximates a regression curve $p(x)$ by performing local weighted averaging in a small neighborhood around the variable x [Har90]. The kernel describes the shape of the weight function used in the local approximation. Typically, the kernel is a continuous, bounded function which integrates to one. The smoothness of the approximation is controlled by a parameter called bandwidth, which describes the size of the local neighborhood around x. In this work, the approximating function is given by the Nadaraya-Watson estimator with Gaussian kernels [Har90], [Har91]. The optimal bandwidth is computed as described in [BA97].

Statistics such as central moments, cumulants, and entropy are applied to the smoothed histogram to describe and analyze the distributions. The central moments

of a probability distribution function $p(x)$ are defined as

$$\mu_i = \int_{-\infty}^{\infty} (x - c)^i p(x) dx. \tag{2.21}$$

The first central moment is zero. The second central moment, μ_2, is the *variance* and describes the amount of variation within the values of x_i. The third central moment, μ_3, is the *skew* and describes the asymmetry of the shape around the mean (Fig. 2.8). The fourth central moment, μ_4, is the *kurtosis* and describes the sharpness of the distribution (Fig. 2.8).

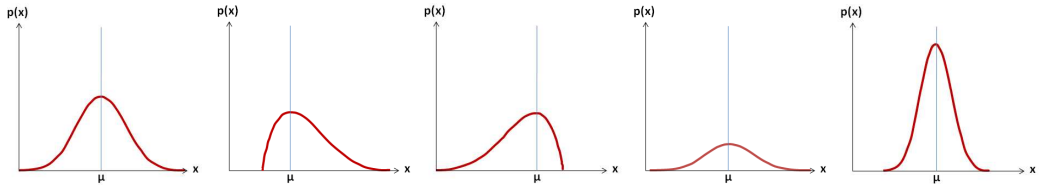

Figure 2.8: Interpretation of third and fourth central moments. (a) Normal distribution with mean μ. (b) Distribution with positive skewness. The asymmetric tail extends out toward positive x values. (c) Distribution with negative skewness. The asymmetric tail extends toward negative x values. (d) Flat distribution with large kurtosis is called *platykurtic*. (e) Sharp distribution with small kurtosis is called *laptokurtic*.

The cumulants of a distribution are closely related to the moments of that distribution. The first five cumulants as functions of the central moments are: $k_1 = c$, $k_2 = \mu_2$, $k_3 = \mu_3$, $k_4 = \mu_4 - 3{\mu_2}^2$ and $k_5 = \mu_5 - 10\mu_3\mu_2$ [JKK05, TK03]. The fourth order cumulant gives a measure of the non-Gaussianity of the variable x [TK03]. Distributions with sharp peeks and heavy tails have positive k_4, whereas distributions with flatter shapes have negative k_4. Gaussian distributions have $k_4 = 0$.

The entropy of a continuous random variable x, with density $p(x)$, is a measure of the uncertainty associated with that variable and it is defined as

$$h(x) = -\int_x p(x) \log p(x) dx. \tag{2.22}$$

The entropy does not depend on the values of x but only on the probabilities that x will occur [CT06].

Statistics describing writhe number, curvature and centroid-radii distributions along the surface or aneurysms are computed from the their corresponding smoothed histograms. The central moments, cumulants and entropy of these histograms are analyzed to develop a better understanding of how shape variation influences rupture status in cerebral aneurysms. Details about the use and performance of histogram statistics for rupture status prediction are provided in Chapters 5 and 6.

2.3 Aneurysm Detection and Characterization

In this thesis, surface analysis based on writhe number and surface curvature is tested on two major areas in the field of neurovascular care - cerebral aneurysms detection and rupture status classification.

2.3.1 Aneurysm Detection

Detecting intracranial aneurysms from imaging scans is an essential step in the prevention of aneurysmal SAH and its attendant complications [WW00]. It is reported that 1% of the patients presenting with headaches to Emergency Departments have SAH and up to 10% of the patients presenting with severe, abrupt-onset headaches complaints have SAH [EMO08]. Although aneurysm detection is currently performed visually by experienced diagnosticians, there is an increasing interest in computed-aided diagnostic (CAD) systems to assist diagnosticians and possibly improve diagnostic accuracy and limit missed detection.

When interpreting scans and searching for aneurysms, it is important for clinicians to have access to the underlying 3D structures from the 2D studies. Because 3D-RA, CTA and MRA data provide vessel and aneurysm positions in cross-

sectional images only, 3D structures are typically extracted from sets of 2D images using segmentation. A great deal of research has been carried out in developing algorithms for the segmentation of cerebral vasculature, including aneurysms, from MRA and CTA studies [FPAB04, HF07, RP09]. Vessel segmentation remains a challenging task and the research in this field remains active. Refer to [LZ05] for a survey of algorithms for vessel segmentation from MRA data and [KQ03] for a survey on vessel extraction techniques and algorithms applied to MRA, CTA and 3D-RA datasets.

In order to visually isolate aneurysms from segmented volumes, it is necessary to study the entire vasculature. Small aneurysms are often visible only from specific viewing directions and may go undetected, leading to misdiagnosis. In contrast, CAD-based aneurysm detection methods highlight possible aneurysm areas and may help improve diagnostic accuracy and ultimately, reduce diagnostic times.

Uchiyama et al. [UAY$^+$05] detect potential aneurysms by measuring the degree of convergence of the surface gradient vectors at each point on the segmented vessels. Analysis of the size, shape, and image intensity of each potential aneurysm is performed to eliminate false positive results. Kobashi et al. [KKH06] construct "normal vasculature models" by dilating the vessel axes obtained by thinning the segmented vasculature, such that the resulting vasculature model has circular cross-sections. Aneurysm candidates are obtained by subtracting the "normal vasculature model" from the segmented arteries. False positive reduction is based on evaluating nine feature values with respect to the shape and intensity of the aneurysms candidates. In the method proposed by Arimura et al. [ALK$^+$04], MRA images are pre-processed using a dot-enhancement filter and potential aneurysms are detected by grey level thresholding of the enhanced images. False positive reduction is performed based on size, local structure and image intensity of potential aneurysms. False positive rates are further reduced by finding short branches in the medial axis

of the vessels and using that as a high likelihood of small aneurysms [ALK+05]. The method is improved using a shape-based image differencing approach which extracts additional features based on local changes in vessel thickness; thin regions have a higher likelihood of being false positives [ALK+06]. The differencing approach determines local changes in thickness using distance-transformed and skeleton images.

The detection methodology presented in this thesis is detailed in Chapter 4. The work is similar to [KQ03] in that we evaluate the intracranial vasculature as a whole and consider normal vessels to be approximated by tubular structures. However, instead of constructing a global vasculature model we focus on local 3D vessel geometry. Our detection method is based on the use of the writhe number. The writhe number as used here describes the 3D geometry of both the parent vessels and potential aneurysms, and proves to be very accurate in distinguishing between healthy vessels and regions with potential aneurysms.

2.3.2 Rupture Analysis

Rupture of cerebral aneurysms is the leading cause of non-traumatic SAH, a condition still associated with 50% mortality despite optimal treatment and care. However, the majority of intracranial aneurysms are asymptomatic and remain undetected. Recent advances in imaging technologies and the increasing use of less invasive computed tomography (CT) and magnetic resonance (MR) imaging in outpatient settings, has led to an increased detection of incidental, asymptomatic unruptured intracranial aneurysms (UIA) during the routine evaluation of headache, dizziness, and trauma [WBHT06, KW07].

With rare exceptions, the general recommendation for all unruptured symptomatic aneurysms is treatment. However, the management of asymptomatic UIA remains controversial [WW00, Wie05, Wei05]. On one hand, should an aneurysm

rupture, the initial bleed is fatal in 10-20% of instances. Despite improvements in patient management, the incidence of subarachnoid hemorrhage (SAH) has not declined over time and the morbidity rate remains between 25% and 50% in patients surviving initial aneurysm rupture [Sch97, WW00, Juv04, STS06]. On the other hand, recent studies estimate the annual rupture rate of a prospectively monitored patient population at only 0.1-0.2% [Wie03], in contrast with earlier data which reported an annual rupture rate of 1-2% [WW00, JGP$^+$01]. Preventive treatment carries risks of complications which increase with age [Wie03], therefore the decision to intervene and treat UIA needs to be balanced against the risk of rupture. To this end, the International Study of Unruptured Intracranial Aneurysms (ISUIA) released the conclusions of two studies in 1998 and 2003 with the goal of defining an optimal treatment strategy of UIA [oUIAI98, Wie03].

These studies concluded that the size and location of the aneurysms play important roles in predicting rupture risk. A threshold of 7mm was proposed for the largest diameter of the aneurysm which is a commonly used size index to predict rupture (Fig. 2.9(a)). However, it is well known from measurements of ruptured aneurysms that many small aneurysms rupture, whereas some large aneurysms never do [JPP00, RMH05, NDM$^+$05]. Ujiie et al. [UTH$^+$99] proposed using the aspect ratio (aneurysm height/neck width) as a potential size index used to estimate the risk of rupture, especially for small aneurysms which might be missed by the largest diameter measure (Fig. 2.9(b)). A threshold value of 1.6 was recommended for the aspect ratio to discriminate between unruptured and ruptured aneurysms. While proving useful in many cases, some studies have failed to detect a statistically significant difference in the aspect ratio of ruptured vs. unruptured aneurysms [SOT$^+$04, RMH05]. Other studies dispute how to best use the measure [BReB$^+$03]. Other commonly used 2D size indexes which were found to be associated with rupture risk are the height-width index, the bottleneck index and the

aneurysm inclination angle [HSF+07]. As shown in Fig. 2.9, the height-width is defined as the height of the aneurysm divided by its largest diameter. The bottle-neck index is defined as the largest diameter of the aneurysm divided by its neck diameter. The inclination angle defined as the angle between the aneurysm height and its neck plane. Recent studies found the inclination angle to be a statistically significant index for rupture risk in sidewall aneurysms ([BSH+10]).

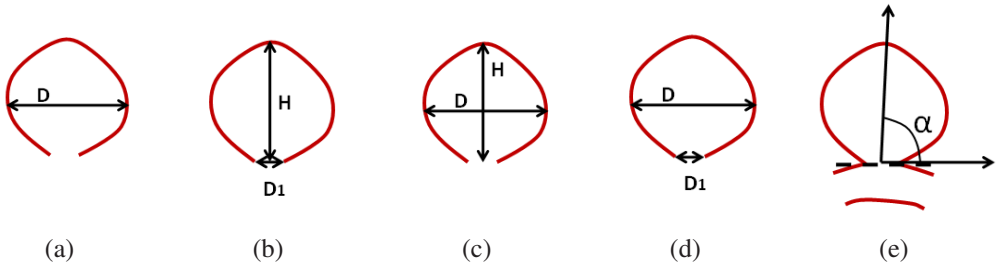

Figure 2.9: Existing 2D size indexes (a) Largest diameter size. (b) Aspect ratio is defined as the height H of the aneurysm divided by its neck diameter D_1 (c) Height-width index is defined as the height H of the aneurysm divided by its largest diameter D. (d) The bottleneck factor is defined as the largest diameter D of the aneurysm divided by its neck diameter D_1. (e) Aneurysm inclination angle is defined as the angle on inclination between the aneurysm and its neck plane.

Cerebral aneurysms present in various shapes and three-dimensional sizes and, like size, shape is likely to have an impact on the rupture risk. With advances in medical imaging, modalities such as 3D rotational angiography (3D-RA), computed tomography angiography (CTA) and magnetic resonance angiography (MRA) can capture the complexity of the volumetric shape and offer the possibility to analyze aneurysms in a 3D environment. Still, the morphological characterization of brain aneurysms remains an open research area. Ma et al. [MHR04] proposed some of the first parameters to describe the 3D geometry of cerebral aneurysms. These authors introduced global descriptors such as undulation, non-sphericity and ellipticity indexes and analyzed their usefulness as rupture predictors in [RMH05].

The ellipticity index (EI) provides a measure of how close the shape of the

aneurysm is to an ellipsoid. The ellipticity index is defined as $EI = 1-(18\pi)^{\frac{1}{3}}\frac{V_{CH}^{\frac{2}{3}}}{S_{CH}}$, where V_{CH} is the volume of the aneurysm convex hull and S_{CH} is the surface of the aneurysm convex hull. The EI varies from 0 to 1, being 0 for a sphere and increasing with ellipticity.

The undulation index (UI) describes how irregular the surface of the aneurysm is. The undulation index is defined as $UI = 1 - \frac{V}{V_{CH}}$, where V_{CH} is the volume of the aneurysm convex hull and V is the aneurysm volume. The UI varies from 0 to 1, being 0 for completely convex aneurysm and increasing with the presence of surface irregularities and lobulations.

The non-sphericity index (NSI) measures how closely the shape of the aneurysm resembles an ellipsoid. The non-sphericity index is defined as $NSI = 1-(18\pi)^{\frac{1}{3}}\frac{V^{\frac{2}{3}}}{S}$, where V is the aneurysm volume and S is the aneurysm surface. The NSI varies from 0 to 1, being 0 for a hemisphere and increasing with deviation from a spherical shape due to ellipticity or undulations in the surface [RMH05].

The EI, UI and NSI indexes are some of the first 3D shape descriptors to be associated with aneurysm rupture risk and to be included in relevant clinical research studies [RMH05, HSF+07, DTM+08]. While the introduction of these indexes showed the potential of 3D shape analysis, computing them requires significant user interaction and does not fully captured the continuous quality of 3D geometry.

More complex 3D descriptors were introduced by Rohde et al. [RLB+05], who applied Fourier analysis to capture the shape irregularities of intracranial aneurysms. Their Fourier analysis was performed on 2D data sets. They evaluated manually segmented contours of aneurysms defined on projection planes subjectively chosen to best show the relationship between an aneurysm neck and its parent vessel. As such, the work was dependent on the choice of projection planes and did not take full advantage of 3D geometry of the aneurysmal lesions. Finally, Millan et al. [MDMP+07] introduced 3D geometrical and Zernike moment invariants to describe

the 3D shape of the aneurysms in an automatic fashion. The performance of Zernike moments was superior to that of geometrical moments, and it was concluded that Zernike moments show richer description properties and are more robust to small perturbations of the models. While the work presented in [MDMP+07] gives an idea of how rich and complex the 3D shape analysis can be, it fails to offer a medical intuition of how and why the proposed descriptors work in predicting aneurysm rupture status.

The rupture status prediction methodology proposed and presented in this thesis is detailed in Chapters 5 and 6. The purpose of the current work is to explore the potential of geometrical characterization of cerebral aneurysms in differentiating between ruptured and unruptured aneurysms. This work is similar to recent morphological studies [MHR04, RMH05, HSF+07, RLB+05, MDMP+07] in that the analysis is performed on a dataset of aneurysms that were classified as being ruptured or not at the time of detection. In contrast to ISUIA studies [oUIAI98, Wie03], the evolution of these aneurysms was not followed clinically over a period of time. As such, this study describes a method for rupture status prediction as opposed to predicting rupture likelihood which would require prospective studies, where in-vivo aneurysms are followed over long periods of time until they rupture or not.

From a technical point of view, this research is close to [MDMP+07] in that it proposes an automatic method to characterize complex shapes, while taking full advantage of the 3D information available in the input data, in this case 3D-RA. In contrast to [MDMP+07], the proposed morphological parameters capture subtle changes on the surface of the shape using the writhe number, surface curvature, and the centroid-radii model.

The centroid-radii model for shape representation was proposed by Chang et al. [CHB91] and refined by Tan et al. [TOT00]. The model uses the distances between the center of mass (centroid) and the boundary of an object to represent the shape

of the object. The original work describes 2D shapes and the intervals between radii is measured in degrees and it is fixed (Fig. 2.10). As a result, each shape is described by a vector of fixed length and the shape comparison is performed using a vector metric. Because the distances are computed from the centroid, the model is translation invariant. The model can be normalized and made scale invariant by dividing all distances by the largest radius. Fan et al. [Fan01] made the comparison rotation invariant by using distance histograms for shape representation. Because the distances are computed from the centroid to the boundary of the shape, the model represents an object by its star-shaped envelope (Fig. 2.10) . An object is said to be star-shaped if there exists a point C interior to the shape, in this case the centroid, such that for every point P on the surface of the object, the line segment PC lies entirely within the object. In other words, every point on the surface of the object is visible from point C. When used to compare two similar objects, the model captures the salient features of their shapes, while discarding small shape variations. The centroid-radii model provides a compact representation of a shape and is currently used in pattern recognition and shape retrieval applications [TOT00, Fan01, TOT03, KLZL07]. The centroid-radii model is similar to the spherical extent function, a ray-based 3D descriptor used in database retrieval applications [VS00, SV01], which captures the furthest intersection points between rays emanating from the center of mass and the surface of the object.

Figure 2.10 shows that the star-shaped envelope of an object can be very different from the original model. However, in our experiments 95% of the aneurysms are star-shaped with respect to their centroids. For the remaining 5%, on average, the star-shaped envelope overlaps the actual aneurysm on more than 98% of the surface. This indicates that using the centroid radii model does not result in a loss of shape information. It also suggests that centroid-radii computation can be further simplified for this particular application and the distances between the centroid and

sample points on the aneurysm surface can be considered directly without checking for surface intersections.

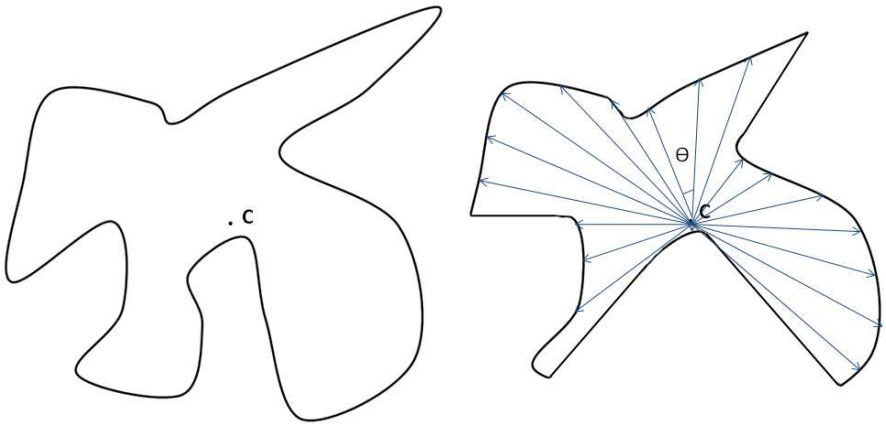

(a) (b)

Figure 2.10: The centroid-radii model applied to a 2D shape. (a) The original shape. (b) The corresponding star-shape envelope with respect to centroid C. The interval between radii is fixed and the resulting distances are stored in a fixed-size vector. Shapes are compared using a vector metric.

For aneurysm shape analysis, the surface distributions of the centroid-radii distances, of writhe numbers and surface curvatures are evaluated through use of histogram statistics. Parameters such as central moments, cumulants and entropy of the histograms are analyzed to develop a better understanding of aneurysm shape variation. These measures are used as classification attributes in predicting rupture status in a dataset of cerebral aneurysms. While proposing some new mathematically sound shape descriptors, we also attempt to make these new indexes more appealing to the medical community by offering the intuition behind their working mechanisms.

Chapter 3

The Writhe Number

3.1 The Writhe Number of Surfaces

In this thesis, the notion of the writhe number is extended from curves to surfaces [LMFM09]. To the best of our knowledge, this is the first time the writhe number is used to characterize surfaces. As in the case for a curve, the writhe number of a surface represents a measure of the complexity of a shape.

Given two points $\mathbf{p}$ and $\mathbf{p}^{'}$ on a surface S, we define a relationship w between them as

$$w(\mathbf{p}, \mathbf{p}^{'}) = \frac{\left[\mathbf{n}_{\mathbf{p}}, \mathbf{p}^{'} - \mathbf{p}, \mathbf{n}_{\mathbf{p}'}\right]}{\mathbf{n}_{\mathbf{p}} \cdot \|\mathbf{p}^{'} - \mathbf{p}\| \cdot \mathbf{n}_{\mathbf{p}'}}, \tag{3.1}$$

where $\hat{\mathbf{n}}_{\mathbf{p}}$ is the unit surface normal at point $\mathbf{p}$, $\|\cdot\|$ is the norm of a vector and $[\mathbf{a}, \mathbf{b}, \mathbf{c}]$ is the triple scalar product of vectors $\mathbf{a}$, $\mathbf{b}$ and $\mathbf{c}$. The triple scalar product is defined as $[\mathbf{a}, \mathbf{b}, \mathbf{c}] = \mathbf{a} \bullet (\mathbf{b} \times \mathbf{c})$, where $\mathbf{a} \bullet \mathbf{b}$ denotes a dot product and $\mathbf{a} \times \mathbf{b}$ denotes a cross product. The absolute value of the triple scalar product is the volume of the parallelipiped defined by vectors $\mathbf{a}$, $\mathbf{b}$ and $\mathbf{c}$ [FPBJES03]. The product supports circular permutation and its value remains the same as long as the three vectors are permuted such that they maintain their initial counterclockwise order. It follows that $\mathbf{a} \bullet (\mathbf{b} \times \mathbf{c}) = \mathbf{b} \bullet (\mathbf{c} \times \mathbf{a}) = \mathbf{c} \bullet (\mathbf{a} \times \mathbf{b})$ [FPBJES03].

The entity $w(\mathbf{p}, \mathbf{p}')$ is a pseudoscalar, meaning that it behaves like a scalar but changes sign under inversion. Indeed, it can be proven using linear algebra that $\mathbf{a} \bullet (\mathbf{b} \times \mathbf{c}) = -(-\mathbf{a}) \bullet ((-\mathbf{b}) \times (-\mathbf{c}))$ [FPBJES03].

We define the writhe number of a point $\mathbf{p}$, given a surface S with $\mathbf{p} \in S$ as

$$W(\mathbf{p}, S) = \int_{\mathbf{p}' \in S} w(\mathbf{p}, \mathbf{p}')\, dS. \tag{3.2}$$

It follows that the writhe number of a point as described by (3.2) depends on the size of the surface and has units of $Length^2$. For our applications (aneurysms detection and rupture classification) we use this measure of the writhe number which is scale dependent. Note that scale independence can be obtained by dividing the writhe of a point by the total area of surface S. This would result in a dimensionless measure.

Upon discretization (3.2) becomes

$$W(\mathbf{p}, S) = \sum_{\mathbf{p}' \in S} w(\mathbf{p}, \mathbf{p}')\Delta\mathbf{p}' \tag{3.3}$$

where $\Delta\mathbf{p}'$ is the unit of surface area. If S is a triangular mesh, then $\Delta\mathbf{p}'$ is the area associated with vertex $\mathbf{p}'$. In this case, the differential surface area, $\Delta\mathbf{p}'$, is computed as one third of the sum area of all triangles defined by $\mathbf{p}'$.

For our processing, we also require the notion of a local neighborhood, $N(\mathbf{p})$, about a point $\mathbf{p}$ on the surface of a vessel. Formally, a point $\mathbf{p}'$ belongs to $N(\mathbf{p})$ if and only if the following two conditions are satisfied. First, the geodesic path from $\mathbf{p}$ to $\mathbf{p}'$ belongs to $N(\mathbf{p})$. This condition guarantees that $N(\mathbf{p})$ is connected. Second, $\|\mathbf{p}' - \mathbf{p}\| \leq d$, $d \in \mathbb{R}_+$. This condition determines the size of the neighborhood and $\|\cdot\|$ denotes the Euclindean norm. The writhe number of a point $\mathbf{p}$, given its local neighborhood $N(\mathbf{p})$ is the surface integral

$$W(\mathbf{p}, N(\mathbf{p})) = \int_{\mathbf{p}' \in N(\mathbf{p})} w(\mathbf{p}, \mathbf{p}')\, dN(p). \tag{3.4}$$

Upon discretization 3.4 becomes

$$W(\mathbf{p}, N(\mathbf{p})) = \sum_{\mathbf{p}' \in N(\mathbf{p})} w(\mathbf{p}, \mathbf{p}')\Delta\mathbf{p}'. \tag{3.5}$$

If N(p) is a collection of uniformly sampled image voxels, then $\Delta\mathbf{p}'$ has a fixed value corresponding to the surface area of a voxel.

3.2 Writhe Number for Aneurysm Detection

For the detection problem it is assumed that healthy vessels can be modeled locally as cylinders or extruded parabolas. An extruded parabola is a tubular structure whose medial axis is a parabola. The assumption that healthy vessels can be modeled locally by cylinders and extruded parabolas is validated experimentally and results are presented in Chapter 4. The 3D writhe number as defined in Section 3.1 is used to detect perturbations from cylinders and extruded parabolas along the vasculature. We claim that if $N(p)$ is a cylinder or an extruded surface along a parabola then $W(p, N(p)) = 0$, i.e the writhe number is zero in regions of normal vasculature. Consequently, regions with non-zero writhe numbers are reported as possible aneurysms. The claim is discussed here and proven in Appendix A, using the pseudoscalar quality of the writhe number.

Given a surface point p and its local neighborhood $N(p)$ as defined in Section 3.1, the writhe number of p over $N(p)$ is given by equation Eq. 3.5 and is a sum of quantities $w(p, p')$ for all $p' \in N(p)$.

3.2.1 The Writhe of a Cylinder

If $N(p)$ is a cylinder, we claim that for every point $p_1 \in N(p)$ there exists a second point $p_2 \in N(p)$, such that the Euclidean distance $|p_1 - p| = |p_2 - p|$ and the line segment p_1p_2 lies on the cylinder surface (Fig. 3.1(a)). These two conditions ensure that the pair (p_1, p_2) is unique. It can be proven that $w(p, p_1) = -w(p, p_2)$ (Appendix A.1). Such pairs of points (p_1, p_2) cancel each other out in the writhe number summation and consequently $W(p, N(p)) = 0$.

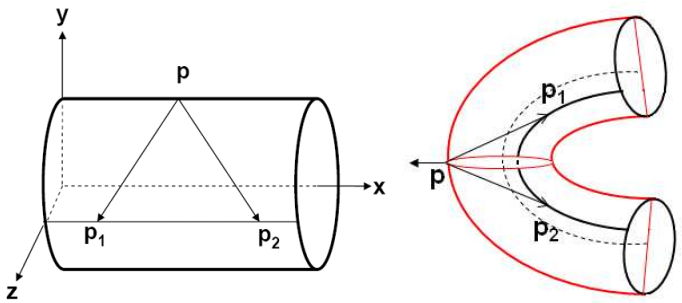

(a) (b)

Figure 3.1: Examples of the writhe number for objects with symmetry. (a) The writhe number of a cylinder is zero based on the symmetric nature of a cylinder. (b) The points on the parabola that have zero writhe numbers are shown in red.

3.2.2 The Writhe of an Extruded Surface Along a Parabola

If $N(p)$ is a non-self-intersecting extruded parabola, its medial axis is a parabola. Let p correspond to the apex of the parabola. For every point $p_1 \in N(p)$ there exists a second point $p_2 \in N(p)$, such that the Euclidean distance $|p_1 - p| = |p_2 - p|$ and p_1, p_2 lie on the extruded surface along a parabola parallel to the medial axis (Fig. 3.1(b)). These two conditions ensure that the pair (p_1, p_2) is unique. It can be proved that $w(p, p_1) = -w(p, p_2)$ (Appendix A.2). Pairs of points (p_1, p_2) cancel each other out in the writhe number summation and consequently $W(p, N(p)) = 0$.

3.2.3 Generalization of Writhe Number

Intuitively, given a surface N and a point $p \in N$ on the surface, $W(p, N) = 0$ if N displays mirror symmetry about a mirror plane which passes through point p and contains the normal at p. Mirror symmetry occurs when two halves of a whole are each other's mirror images [HH94]. Mirror symmetry guarantees that for every point $p_1 \in N$ there exists a second point $p_2 \in N$, at the opposite side of the mirror plane, such that the Euclidean distance $|p_1 - p| = |p_2 - p|$. A cylinder has an infinite number of mirror planes passing through its axis. An extruded parabola has two mirror planes, one which contains the medial axis and one which is perpendicular to the medial axis (Fig. 3.1(b)). The usefulness of the writhe number in aneurysm detection is discussed in Chapter 4.

3.3 Writhe Number for Rupture Status Prediction

This notion of symmetry captured by the writhe number is used for aneurysm detection to distinguish between normal vessels and aneurysmal regions. Healthy vessels are modeled locally as cylinders and the nominal behavior of the vasculature results in writhe number being equal to zero for regions along normal vessels. Consequently, those portions of the vessels where the writhe number is non-zero are reported as possible aneurysms. In contrast, for aneurysm rupture status prediction we make use of the statistics of the writhe number defined over the entire aneurysmal surface to predict rupture status. Kernel density estimation methods are used to represent the writhe number distribution and statistics computed from these distributions form the basis for our classification methods.

3.3.1 A Physical Interpretation of Surface Writhe

To provide some intuition concerning the morphological utility of the writhe number in our analysis of 3D surfaces, we discuss here an analogy between the writhe number of surfaces and the torque, as defined in mechanics [ST06].

The torque, also called the moment of force, describes the rotational effect of an external force applied to a rigid body S. The torque τ acting on S under the influence of an external force $\mathbf{F}$ is defined as $\tau = \mathbf{r} \times \mathbf{F}$. Vector $\mathbf{r}$ is the distance vector between the origin of the torque, a point O, and the point where $\mathbf{F}$ is applied [ST06, FPBJES03]. When the rigid body is defined as a system of points or particles, concurrent forces can be applied on different points on the surface of S. The overall effect of these forces is measured by the net torque

$$\tau = \sum_{i=0}^{N} \mathbf{r_i} \times \mathbf{F_i} = \sum_{i=0}^{N} \tau_i, \tag{3.6}$$

where N is the total number of concurrent forces, $\mathbf{F_i}$ is the force acting on a point $\mathbf{p_i} \in S$ and $\mathbf{r_i}$ is the vector from point O to the point $\mathbf{p_i}$ (Fig. 3.2(a)).

Similarly to 3D rotation, the notion of torque can be extended to measure the rotational effect about an axis rather than a point. Let $\mathbf{n}$ be the unit vector along an arbitrary axis OL. The torque τ about the axis defined by $\mathbf{n}$, acting on S under the influence of an external force $\mathbf{F}$ is defined as $\tau = \mathbf{n} \bullet (\mathbf{r} \times \mathbf{F})$ [FPBJES03]. In other words, $\tau = [\mathbf{n}, \mathbf{r}, \mathbf{F}]$ is the triple scalar product of vectors $\mathbf{n}$, $\mathbf{r}$ and $\mathbf{F}$ (Fig. 3.2(b)). When concurrent forces are applied on S, the net torque about $\mathbf{n}$ is

$$\tau = \mathbf{n} \bullet \sum_{i=0}^{N} \mathbf{r_i} \times \mathbf{F_i} = \sum_{i=0}^{N} \tau_i. \tag{3.7}$$

Using the distributive property of the dot product, the net torque about an axis $\mathbf{n}$ can be expressed as

$$\tau = \sum_{i=0}^{N} [\mathbf{n}, \mathbf{r_i}, \mathbf{F_i}] \,. \tag{3.8}$$

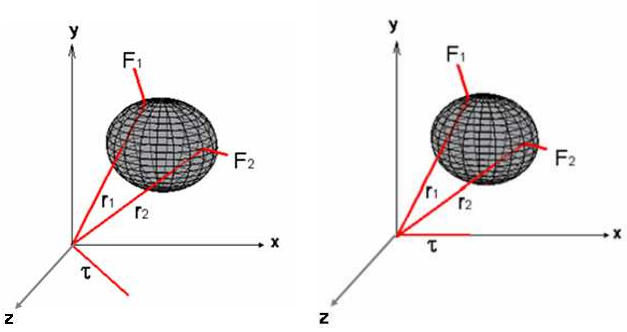

(a) (b)

Figure 3.2: The torque τ of a rigid body under the effect of two concurrent forces, $\mathbf{F_1}$ and $\mathbf{F_2}$. (a) The torque about the origin. (b) The torque about the $\mathbf{x}$ axis represents the projection of the torque about the origin on the axis.

The rigid body is said to be in equilibrium along an axis of rotation if its net torque about that axis is zero [ST06, FPBJES03].

For the purposes of this work, S is the surface of an aneurysm described as a collection of 3D vertices, $\mathbf{p_i} \in S$, with normals $\mathbf{n_i}$. Unit forces act at the vertices of S in the direction of their surface normals, creating a discretized force field surrounding the aneurysm. When computing the writhe of a particular point $\mathbf{p}$, the normal $\mathbf{n}$ at $\mathbf{p}$ is considered the rotational axis of the torque.

Returning to the writhe number, the writhe of a point $\mathbf{p}$ as defined in Eq. 3.5 can be expressed as a function of the torque about the normal at point $\mathbf{p}$

$$W(\mathbf{p}, S) = \sum_{\mathbf{p_i} \in S}^{N} \frac{\tau_i}{\|\mathbf{n_p}\| \cdot \|\mathbf{p_i} - \mathbf{p}\| \cdot \|\mathbf{n_{p_i}}\|} \Delta p_i \tag{3.9}$$

which better reflects the relation between the writhe of a point and the torque along the axis defined by the normal at that point. In effect, we are computing the torque along the normals of all the points on the surface of the aneurysm. Using the analogy with the torque, it can be concluded that the writhe number of a point $\mathbf{p}$ is

proportional to the tendency of the normals to impart to the aneurysm a motion of rotation about the fixed axis $\mathbf{n}$, where $\mathbf{n}$ is the normal at point $\mathbf{p}$.

If the rigid body, in this case the aneurysm, were free to move, it would rotate about $\mathbf{n}$ under the effect of the torque. If, however, we consider the rigid body fixed in some way, the torque would not be able to move the aneurysm, and instead it will create tension at point $\mathbf{p}$ on its surface. Throughout this work, the writhe number is viewed as a measure of how close the aneurysm is to equilibrium at each point on its surface. In other words, the writhe number measures how much "tension" there is on the surface of the aneurysm. Intuitively, the more spread out and the stronger the "tension" is on the surface, the greater the likelihood is for rupture. The usefulness of the writhe number in rupture prediction is discussed in Chapter 5.

Chapter 4

Automated Detection of Intracranial Aneurysms using the Writhe Number of Surfaces

In this chapter, the theory behind the writhe number of surfaces is applied to automatic detection of intracranial aneurysms. As described in Chapter 2, detecting brain aneurysms from imaging scans is an important step towards the diagnosis, treatment and management of aneurysmal SAH. Following the methodology detailed in this chapter, the writhe number is used to describe the vasculature locally and to determine the presence of possible aneurysmal lesions.

4.1 Method

4.1.1 Overview of the Detection Algorithm

The detection method takes as input a 3D volume in which the cerebral vasculature has been segmented from the background. The medial axis of the vessels is computed from the segmented volume. Similar to [ALK$^+$05], we consider that

aneurysms appear as short branches in the medial axis of the vasculature. Local neighborhoods are determined for surface points along short branches such that they satisfy the connectedness and size conditions described in Chapter 3, Section 3.1. The writhe number is computed for each local neighborhood, and regions with non-zero writhe numbers are reported as possible aneurysms. The size of each region is determined and small regions are eliminated from results based on a thresholding criteria. Details about each of these steps are presented below.

4.1.2 Segmentation

The detection method requires a segmented volume of the cerebral vasculature. The appropriate segmentation method depends on the modality of the input data (CTA, MRA, 3D-RA). Practical details about the preprocessing and segmentation techniques used on our particular input data are provided in Sections 4.2. From the segmented volume, the surface of the vessels is described as the set of voxels which have at least one adjacent background voxel.

4.1.3 Medial Axis Detection

The medial axis of the vessels is computed using the method described by Bouix et al. [BST05] and using a skeletonization algorithm which exploits the distance field corresponding to the segmented vessels.

4.1.4 Short Branches Selection

The aneurysm detection method takes advantage of the fact that aneurysms appear as small branches along the medial axis [ALK$^+$05]. Once the medial axis is computed, each voxel on the medial axis is labeled as an end point (the voxel has one adjacent neighbor), a connecting point (the voxel has two adjacent neighbors) or

a junction point (the voxel has three or more adjacent neighbors). Short branches are paths between end points and junction points with a length smaller than a specified threshold value where the threshold is set using voxel dimensions to detect aneurysms up to 50 mm long. In studies, 90% of the aneurysms are smaller than 25 mm in diameter and only 10% are giant aneurysms with sizes between 25-50 mm [RS06]. It should be noted that most of the short branches determined this way are actually noise on the medial axis and are only few voxels long. However, for our detection algorithm, the medial axis provides vital information about aneurysms locations and while reducing the sensitivity of the medial axis algorithm or smoothing the result might reduce the number of short branches, it could also result in misdetection of small aneurysms.

4.1.5 Local Neighborhood Model

Local neighborhoods are determined for the collection of points on the surface of short branches. Given a surface point, $\mathbf{p}$, we want to determine its local neighborhood $N(\mathbf{p})$. A second point, $\mathbf{c}$, is found such that $\mathbf{c}$ belongs to the medial axis, $\mathbf{c}$ is the closest point to $\mathbf{p}$, and $\mathbf{c}$ was labeled as a short branch medial point in Section 4.1.4. In most of the cases, $\mathbf{p}$ is a point on the surface of a normal vessel and $\mathbf{c}$ is a noise point on the medial axis sitting close to the true medial axis of the region (Fig. 4.1(a) and 4.1(b)).

Let R be the Euclidean distance between points $\mathbf{c}$ and $\mathbf{p}$. The local neighborhood of point $\mathbf{p}$ is built around point $\mathbf{c}$ and is defined as the connected set of points whose Euclidean distance is within $R\sqrt{2}$ from $\mathbf{c}$ (Fig. 4.1). Using this method, the local neighborhood of $\mathbf{p}$ is a small segment of the vasculature. In the case of a cylinder, the $R\sqrt{2}$ threshold guarantees a one-to-one length-diameter aspect ratio, which works well in practice. Depending on the local bending of the vessels near $\mathbf{p}$, the medial axis of $N(\mathbf{p})$ can be approximated by either a line segment (in this

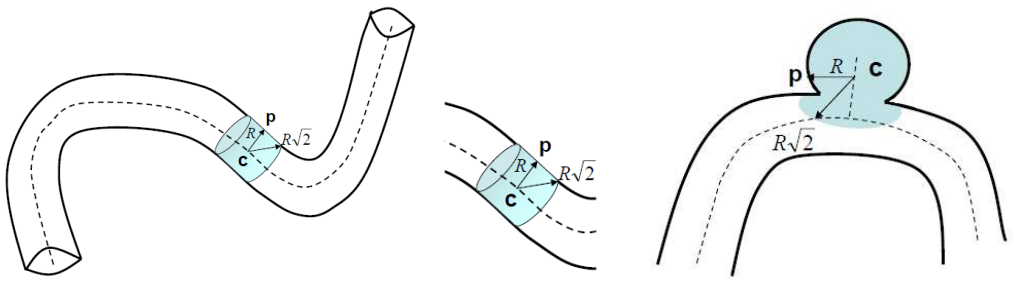

(a) (b) (c)

Figure 4.1: Local neighborhood of surface point $\mathbf{p}$. $\mathbf{c}$ is the point on a short branch closest to $\mathbf{p}$. Most points $\mathbf{c}$ represent noise on the medial axis and sit close to the true medial axis of the normal vessels. The local neighborhood of $\mathbf{p}$ is build around $\mathbf{c}$ and is defined as the connected set of surface points whose Euclidean distance is within $R\sqrt{2}$ from $\mathbf{c}$ (a) $\mathbf{p}$ is a point on the surface of normal vessels and $\mathbf{c}$ is a noise point on the medial axis sitting close to the true medial axis of the region. (b) Detail of local neighborhood on healthy vessels. (c) $\mathbf{p}$ belongs to an aneurysm.

case $\mathbf{c}$ is the midpoint of the segment) or by a parabola (in this case $\mathbf{c}$ is the apex of the parabola). This will be verified experimentally in Section 4.2.3. For healthy vessels, the construction guarantees that $\mathbf{p}$ sits on a mirror plane of $N(\mathbf{p})$.

The local neighborhood of a surface point is determined as described above independent of the location of the point on the vasculature. Fig. 4.1(c) shows the local neighborhood of a point on the surface of an aneurysm. The neighborhood contains part of the aneurysm as well as a portion of the parent vessel. Because the points on the surface of an aneurysm concentrate around the same medial axis points, they share the same local neighborhood. Even in those cases where the aneurysm area might display some symmetries, most surface points will not sit on mirror planes and therefore will have non-zero writhe numbers. Exceptions might be fusiform aneurysms which present as local dilatations of an artery, having perfectly circular cross sections and showing symmetries similar to those of normal vessels. In practice, our method was able to detect certain biological fusiform aneurysms because of their uneven dilatations in multiple directions perpendicular to the vessel axis.

4.1.6 Writhe Number Computation

Writhe numbers are computed along the surface of each local neighborhood, according to Eq. 3.5. To a very high degree of accuracy, the nominal behavior of the vasculature results in the writhe number being equal to zero for the neighborhoods along healthy vessels. This follows because locally normal vessels are shaped as cylinders or extruded parabolas which in theory have a zero writhe number. The local neighborhoods of points on the aneurysms do not display the same symmetries as cylinders and extruded parabolas and as a result have non-zero writhe numbers.

4.1.7 False Positive Reduction

Adjacent voxels on the surface of the vessels having non-zero writhe numbers are clustered in regions which are considered positive results and are highlighted as possible aneurysms. The detection method based on writhe numbers shows high specificity and as a result we are able to threshold positive results using simple features related to the size of the candidate regions. Specifically, our source data originated from multiple modalities, collected with different scanner models, and having different voxel sizes, therefore, the number of voxels within each positive region is a poor indicator of the absolute physical size of the region. The size of a voxel plays an important role in discriminating between true positives and false positive based on region size, since the same number of image voxels describe different physical sizes depending on the resolution of the data. For instance, an image region of 100 voxels describe a larger physical region on a dataset with voxel size $0.5 \times 0.5 \times 1.00\,\text{mm}^3$ than is does on a dataset with voxel size $0.5 \times 0.5 \times 0.5\,\text{mm}^3$. In order to analyze positive regions in a unique manner across modalities and scanners, a *region index* [mm^3] is defined as the product between the size of the region in voxels and the volume of the voxel. Effectively, the volume of all voxels on the surface of the positive region is summed. The region index is

used as an alternative to the surface area of the positive regions in order to avoid the triangulation of the surface. Under this definition, 100 voxels describe a region index of 25 mm^3 on a dataset with voxel size $0.5 \times 0.5 \times 1.00\ mm^3$. The same 100 voxels describe a region index of 12.5 mm^3 on a dataset with voxel size $0.5 \times 0.5 \times 0.5\ mm^3$. The region index gives an intuition of the physical size of a positive result independent of the resolution of the input data. True positives tend to have a larger region index than false positives and therefore in this work we threshold positive results based on their region index. In Section 4.3, under detection results, it is shown how detection and false positive statistics change according to the threshold value of the region index.

4.2 Clinical Data

4.2.1 3D-RA, MRA and CTA

The aneurysm detection method was tested on ten distinct 3D rotational angiography (3D-RA), ten unrelated magnetic resonance angiography (MRA) and another ten unrelated computed tomography angiography (CTA) patient-derived datasets. The thirty studies contain thirty aneurysms, with two studies showing no aneurysms and two studies having two aneurysms each. The aneurysms have diameters in the range 3.2-9.8 mm (mean 5.52) and lengths in the range 3.5-8.3 mm (mean 5.65). Among the aneurysms, twelve are sidewall aneurysms (dilatation of the artery in one direction perpendicular to the vessel axis), thirteen are bifurcation aneurysms (dilatation at the bifurcation of arteries) and five are a fusiform aneurysm (dilatation of the artery in multiple directions more or less perpendicular to the vessel axis). All aneurysms were identified a priori and classified by two independent operators.

3D-RA data were acquired using a biplane flat-detector digital subtraction angiography system (Axiom Artis, Siemens Medical Solutions, Malvern PA) at Tufts

Medical Center, Department of Neurosurgery (Boston, MA). 3D-RA is a technique employed to visualize blood vessels in a bony or dense soft tissue environment. Contrast agent is injected through a catheter which is navigated from a percutaneous femoral arterial access into a carotid or vertebral artery (i.e. one of the vessels leading to the brain vasculature). Images acquired in the presence of the contrast agent are subtracted from images acquired pre-contrast. In the case of intracranial scanning, 3D-RA produces images with very high contrast between vasculature and the surrounding environment (Fig. 4.2(a)). In the current study, the size of each 3D-RA data volume is $256 \times 256 \times 229$, with 0.48 mm isotropic voxels.

MRA is a type of magnetic resonance imaging used to visualize the blood flow and the conditions of the arteries (Fig. 4.2(b)). Most of the time, a contrast agent is used to enhance the vessels. The MRA datasets were acquired on a variety of scanners previous to the patient referral for specialized treatment to the Department of Neurosurgery at Tufts Medial Center. The following scanners were used for acquisition: 1.5T Magnetom Vision (Siemens Medical Solutions, Malvern PA; voxel size $0.78 \times 0.78 \times 0.97$ mm), 3T Achieva (Philips Medical Systems, Andover MA; voxel size $0.39 \times 0.39 \times 1$ mm), 1.5T Genesis Signa (GE Medical Systems, Schenectady NY; voxel size $0.39 \times 0.39 \times 1.6$ mm) and 1.5T Magnetom Symphony (Siemens Medical Solutions; voxel size $0.89 \times 0.89 \times 1.6$ mm).

CTA is a type of x-ray imaging used to visualize blood vessels. Images are acquired in the presence of an iodine-based contrast agent injected as an intravenous solution (Fig. 4.2(c)). Two scanners were used for the acquisition of the CTA datasets: Definition (Siemens Medical Solutions; voxel size 0.35 mm $\times$ 0.35 mm $\times$ 1 mm) and LightSpeed Plus (GE Medical Systems; voxel size 0.40 mm $\times$ 0.40 mm $\times$ 1.25 mm).

Although catheter-based 3D-RA imaging remains the gold standard in cerebral aneurysm imaging, MRA and CTA are less-invasive modalities with increasingly improving sensitivity and specificity, which are being used more and more for cere-

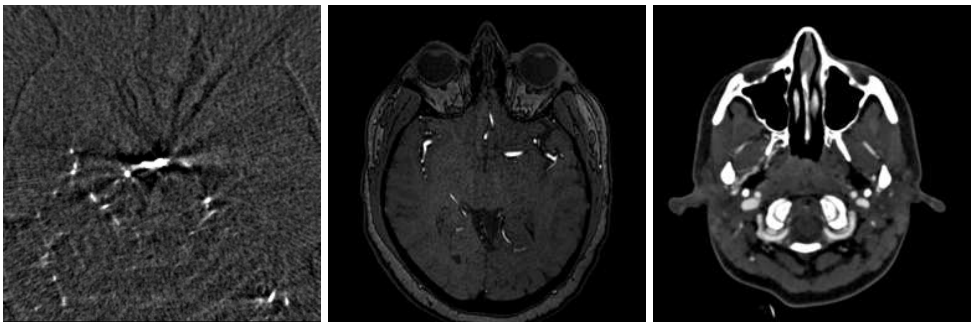

(a) (b) (c)

Figure 4.2: Images of vasculature obtained using different modalities. (a) 3D-RA axial image (window 1000, level -200) displays high contrast between vasculature and surrounding tissue. (b) MRA axial image (window 150, level 125). A contrast agent is used to enhance the vessels. (c) CTA axial image (window 700, level 250). The contrast agent injected during CTA imaging increases the image contrast between vessels and surrounding soft tissue, but lowers the contrast between vessels and bone.

brovascular imaging and aneurysm detection ([EMO08]).

4.2.2 Preprocessing

Prior to segmenting the vasculature, CTA and MRA data volumes were resampled to isotropic voxel size. Because of the high resolution of the data and high contrast between vasculature and surrounding tissue, vessel segmentation of 3D-RA data is a relatively simple task (Fig. 4.2(a)). CTA and MRA images have lower spatial resolution compared to 3D-RA and may show physical (partial volume, beam hardening) and patient-related artifacts (metal, motion and ghosting effects) [GJMP06, KE09]. The contrast agent injected during CTA imaging increases the image contrast between vessels and surrounding soft tissue, but lowers the contrast between vessels and bone, making cerebral vessel segmentation more challenging (Fig. 4.2(c)). Furthermore, CTA data display venous contamination of the images (i.e. contrast agent reaching the venous system and precluding adequate visualization of arteries). In the case of CTA, the bone was removed from the images using

a commercial 3D visualization and modeling system (Amira, Mercury Systems, Chelmsford MA). Vessel segmentation was performed on all datasets using a combination of thresholding and region-growing techniques [PXP00]. The resulting segmented volumes were used as input to the aneurysm detection method.

4.2.3 Experimental Validation of Local Neighborhoods

The aneurysm detection method relies on the assumption that if the local neighborhood of a surface point on a normal vessel is determined as described in Section 4.1.5, it can be approximated by either a cylinder, in which case the medial axis is a line segment, or by an extruded parabola, in which case the medial axis is a parabola. The assumption was tested experimentally on the ten 3D-RA patient-derived datasets. Regression analysis was applied to each local neighborhood and points on the medial axis were fit to both a line and a parabola. The smallest fitting error between the two determined if the local neighborhood was best approximated by a cylinder or by an extruded surface along a parabola.

Orthogonal linear regression [Ahn04] was applied to minimize the perpendicular distances from the medial axis points to the fitting 3D line. As described in [Ahn04], we fit a set $\{X_i\}_{i=1}^m$ of m points on the medial axis to a line described in parametric form by the equation $X_0 + u\mathbf{r} = 0$, where X_0 is a point on the line and the centroid of the medial axis points, $\mathbf{r}$ is a direction vector, $\|\mathbf{r}\| = 1$ and $u \in \mathbb{R}$. The orthogonal fitting is achieved by finding $\mathbf{r}$ which minimizes the square sum of the orthogonal distances from the points to the line

$$\min_{\mathbf{r}} \sum_{i=1}^{m} \|(X_i - X_0) \times \mathbf{r}\|^2.$$

Fig. 4.3 shows the histogram of line fitting errors. The horizontal axis represents the corresponding root mean squared (RMS) errors defined as $\text{RMS} = \sqrt{\frac{1}{m}\sum_{i=1}^{m} \epsilon^2}$,

where ϵ_i is the Euclidean distance from medial axis point i to the fitting line. The vertical axis shows the number of local neighborhoods which can be approximated by cylinders.

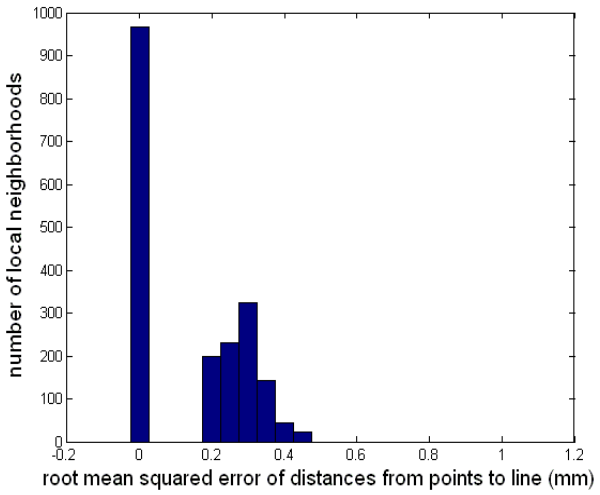

Figure 4.3: Histogram of line fitting errors.

In the case of parabola fitting, first orthogonal regression was applied to fit the 3D medial axis points to an arbitrary plane described by the equation $(X - X_0)^T \cdot \mathbf{n} = 0$, where X is an arbitrary point on the plane, X_0 is a point on the plane and the centroid of the medial axis points, $\mathbf{n}$ is the normal to the plane and $\|\mathbf{n}\| = 1$ [Ahn04]. The orthogonal fitting is achieved by finding $\mathbf{n}$ which minimizes the square sum of the orthogonal distances from the points to the plane

$$\min_{\mathbf{n}} \sum_{i=1}^{m} \|(X_i - X_0)^T \cdot \mathbf{n}\|^2.$$

Fig. 4.4 shows the histogram for plane fitting errors. It can be seen that the medial axis points for each local neighborhood are very close to being coplanar.

The 3D points were then projected onto the fitting plane and represented as 2D points in a local coordinate system. The set of 2D points, $\{(x_i', y_i')\}_{i=1}^{m}$, were fit to a 2D parabola described by equation $(y - k)^2 = 4a(x - h)$, where (h, k) is the

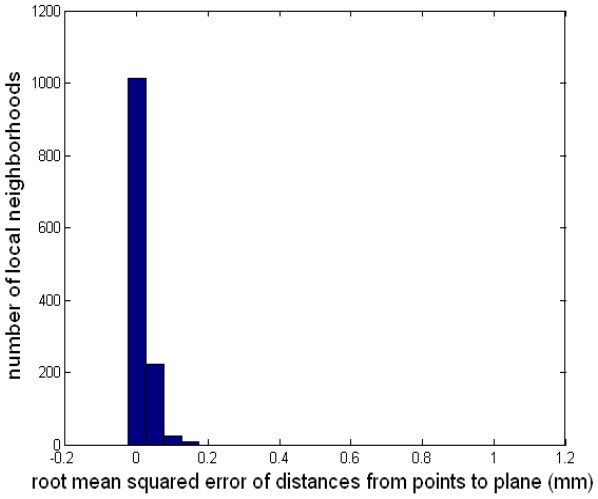

Figure 4.4: Histogram of plane fitting errors.

vertex of the parabola and $a \in \mathbb{R}$, $a \neq 0$. In addition to minimizing the distances from each point to parabola, we constrained the system such that the apex of the parabola was fixed to the center of the medial axis (point **c** from Fig. 4.1).

$$\min_a \sum_{i=1}^{m} \|(y_i - k)^2 - 4a(x_i - h)\|^2,$$
$$\text{such that } c = (h, k).$$

The histogram for parabola fitting errors is shown in Fig. 4.5. On the horizontal axis are the corresponding RMS errors from the medial axis points to the fitting parabola. The vertical axis shows the number of local neighborhoods which can be approximated by extruded surfaces along a parabola.

Note that the maximum fitting error in each of the three cases are smaller than the voxel size, which is $0.48 \times 0.48 \times 0.48$ mm^3. This local neighborhood analysis shows that it is reasonable to model small regions along normal vessels as cylinders and extruded parabolas. Deviations from such geometries are captured by the writhe number computations and provide a useful tool for finding aneurysms as abnormal vessel regions.

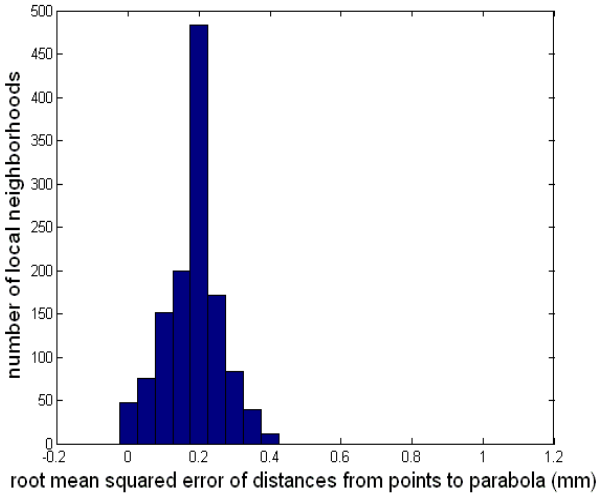

Figure 4.5: Histogram of parabola fitting errors.

4.3 Aneurysm Detection Results

All aneurysms were correctly identified by our detection method with 0.66 false positives per study on 3D-RA data, 5.70 false positives per study on MRA and 5.36 false positives per study on CTA. These results were obtained as follows. As discussed in Section 4.1.7, we start by clustering voxels whose writhe number is non-zero. The region index associated with each cluster is then computed. Suspect regions are taken as those whose region index exceeds a given threshold. The performance analysis in this paper is evaluated by varying this threshold and examining relevant statistics.

Specifically, for each threshold value, the following quantities were computed: number of true positives (TP), number of false positives (FP), number of false negatives (FN) and true positive fraction (TPF). The true positive fraction is defined as

$$\text{TPF} = \frac{\text{TP}}{\text{TP+FN}}.$$

The sensitivity of the method is measured in percentage and is computed as $\text{TPF} \times 100$.

Table 4.1: Statistics for aneurysm detection on 3D-RA.

Threshold Value (region index)	TPF (%/100)	FN (avg per study)	FP (avg per study)
0	1	0	3.66
5	1	0	1.33
7.5	1	0	1
10	1	0	0.66
12.5	0.87	0.11	0.44
15	0.50	0.33	0.22
17.5	0.35	0.33	0.22

Table 4.2: Statistics for aneurysm detection on MRA.

Threshold Value (region index)	TPF (%/100)	FN (avg per study)	FP (avg per study)
0	1	0	19.60
5	1	0	5.70
7.5	0.72	0.30	4
10	0.54	0.50	1.90
12.5	0.54	0.50	1.40
15	0.54	0.50	0.70
17.5	0.54	0.50	0.50

Tables 4.1, 4.2 and 4.3 show how detection statistics change as a function of the region index threshold value applied on the detection results, for 3D-RA, MRA and CTA respectively. It is apparent from the three tables that most false positive results have very small region indexes. The purpose when applying the region index threshold is to reduce the FP value, while maintaining a TPF value of 1. TPF equals 1 when all aneurysms are detected.

Table 4.3: Statistics for aneurysm detection on CTA.

Threshold Value (region index)	TPF (%/100)	FN (avg per study)	FP (avg per study)
0	1	0	28.80
5	1	0	5.36
7.5	0.90	0.10	3.27
10	0.81	0.18	2.27
12.5	0.81	0.18	1.54
15	0.81	0.18	1.36
17.5	0.63	0.36	1

The method detected all aneurysms and resulted in 3.66 false positives for 3D-RA data (Table 4.1), 19.60 for MRA data (Table 4.2) and 28.80 for CTA data (Table 4.3). These are detection results before any false positive reduction, which show that the detection specificity is much higher on 3D-RA data than on MRA and CTA. The first level of thresholding (with a region index of 5) reduces the MRA false positives from 19.60 to 5.70, CTA false positives from 28.80 to 5.36 and the 3D-RA positive results from 3.66 to 1.33, showing that most false positives are very small in size, especially for MRA and CTA data. The 3D-RA false positives can be further thresholded for a region index up to 10 which corresponds to 0.66 false positives per study.

To evaluate the performance of the proposed detection method, free-response operator characteristic FROC analysis was applied as shown in Fig. 4.6. The horizontal axis indicates the average number of false positives (FP) per study, while the vertical axis indicates the true positive fraction (TPF), which is related to the sensitivity of the detection. Specifically, the FROC curves were determined by plotting TPF (second column from Tables 4.1, 4.2 and 4.3) as a function of FP (fourth column from tables) for all 3D-RA, MRA and CTA data. Figure 4.6 shows how many false positive results are observed on average before one aneurysm is detected for 3D-RA (0.66 false positives), MRA (5.7 false positives) and CTA (5.36 false positives). The results correspond to thresholding positive results with a region index of 10 for 3D-RA data and 5 for MRA and CTA data.

The relationship between the writhe numbers and the size of the suspected regions is shown in Fig. 4.7. The horizontal axis holds the total writhe numbers for each positive result, computed as the sum of writhe numbers of all surface points on that positive result. On the vertical axis are the corresponding region indexes. True positives are shown as red stars and false positives are shown as blue stars. The analysis is done on the ten 3D-RA datasets. The figure shows that it is reasonable

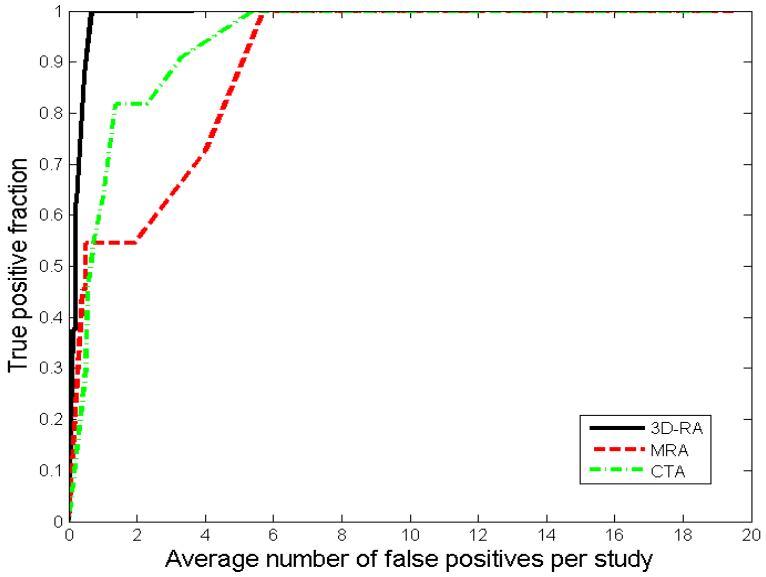

Figure 4.6: FROC analysis of the aneurysm detection algorithm on 3D-RA, MRA and CTA data. The figure shows how many false positive results are observed on average before one aneurysm is detected for 3D-RA, MRA and CTA.

to use the size of the positive regions as a threshold value. It also suggests that both the size of the positive regions and the surface writhe number can be used to classify true positives vs. false positives using linear discriminant analysis.

Figures 4.8 and 4.9 show the visual results of the detection algorithm after thresholding positive results with region index smaller than 10.

4.4 Discussion

The proposed detection method was tested on thirty datasets from three imaging modalities, acquired with seven different scanner models. Despite the data being highly non-homogeneous, all aneurysms were detected correctly.

As shown by the FROC analysis, the detection algorithm performs very well on 3D-RA data and results in few false positive results (0.66 per study). 3D-RA images have high resolution and show high contrast between vasculature and surrounding tissue and simple segmentation techniques result in accurately segmented

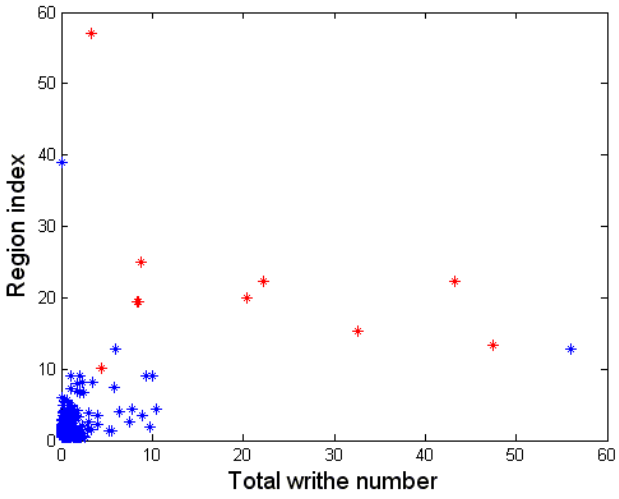

Figure 4.7: Relationship between the writhe number and region index. The total writhe number of a positive region is computed as the sum of writhe numbers of all individual surface points. True positives are shown as red stars and false positives are shown as blue stars. The analysis is done on the ten 3D-RA datasets.

Table 4.4: Performance comparison with existing detection methods on MRA data.

Method	Total Aneurysms	Sensitivity(%)	FP per study
[ALK+04]	36	100	2.40
[ALK+05]	61	97	5.80
[ALK+06]	61	97	3.80
[UAY+05]	7	100	1.85
[KKH06]	19	100	6.43
Proposed Method	11	100	5.70

volumes. Segmentation is more challenging on MRA and CTA data which have lower resolution, more artifacts and show venous contamination.

While the performance of the proposed method is comparable to that of existing methods on MRA data (Table 4.4), there is a direct relationship between the quality of vessel segmentation and the accuracy of the detection method. Because this study focused on aneurysm detection, simple, readily available segmentation methods were used to preprocess the image data. However, particularly for MRA and CTA imaging, it is likely that better segmentation techniques [HF07, RP09, FPAB04] would improve the detection accuracy.

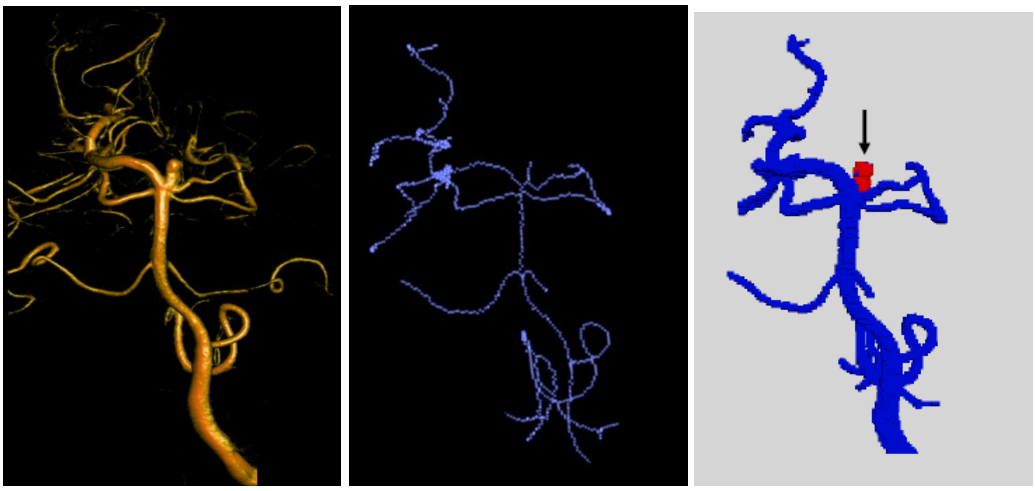

(a) (b) (c)

Figure 4.8: Aneurysm detection results on one patient study. (a) Original 3d-rotational angiography. (b) Corresponding medial axis of the 3D-RA dataset. (c) Detection results. Positive results are colored in red. Black arrows point to true positives.

The clinical value of the algorithm depends on its performance on less-invasive CTA and MRA modalities. The current method is intended to be eventually generalized to include non-invasive cross-sectional imaging modalities and such studies will require an in-depth analysis of the characteristics, shortcomings and strengths of each imaging modality. The input modality will affect the choice of optimal segmentation algorithms and the effect of the segmentation performance on the detection results. While these complex issues were avoided by our use of 3D-RA data in this initial report, they will be the basis of future studies.

The presence of noise in the medial axis calculation, especially for narrow vessels (2-3 voxels in diameter) is the reason for a large portion of the false positive results. The medial axis of the vessels is computed applying the method described by [BST05], which in tests on synthetic data showed a high percentage of voxel overlap between the computed medial axis and the ground truth medial axis. In regions where the computed medial axis did not overlap the ground truth medial axis, the average distance reported was half a voxel. The maximum reported dis-

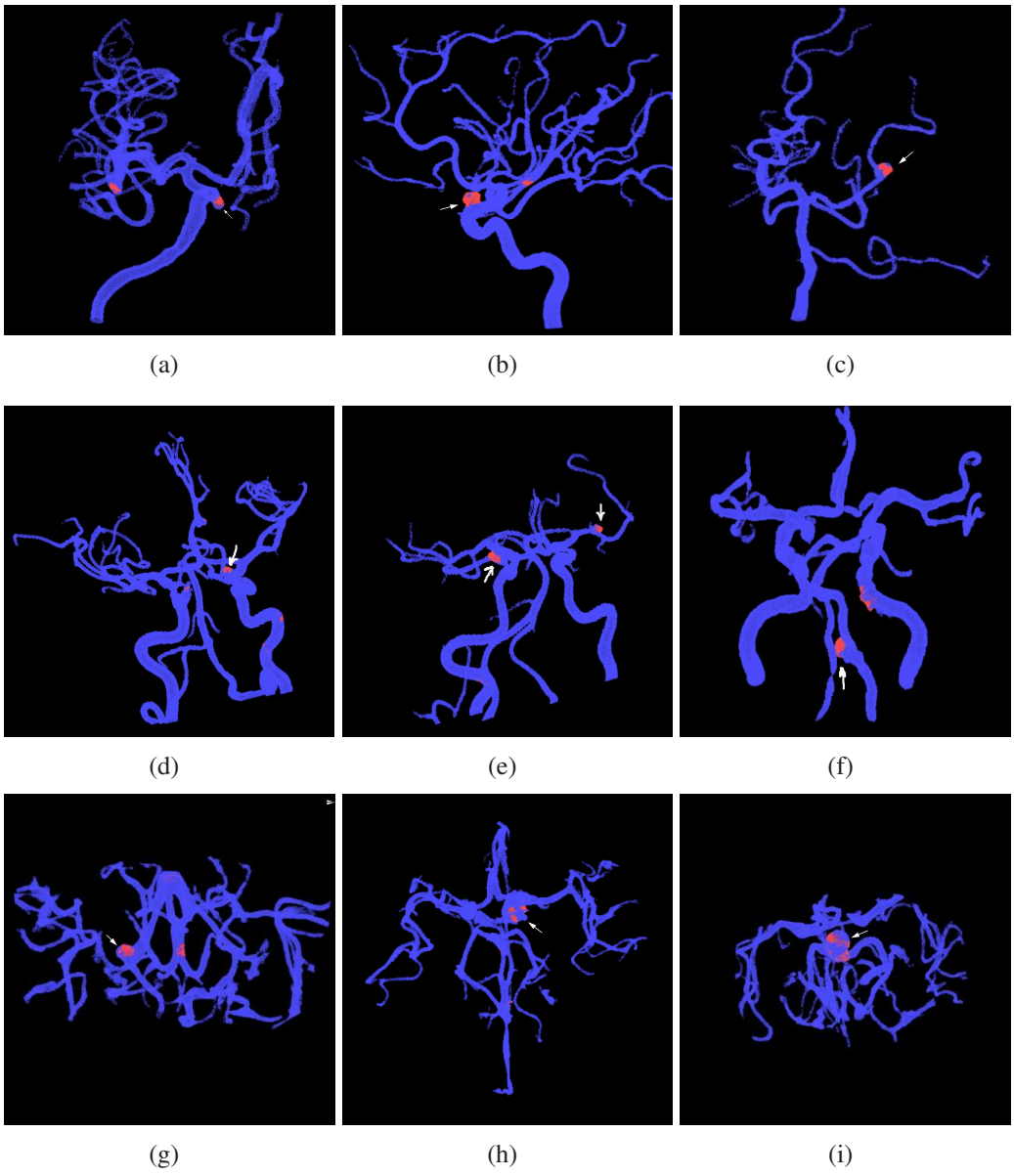

Figure 4.9: Aneurysm detection on six patient-derived datasets. Results shown after thresholding positive results with a region index of 5. Positive results are colored in red. The white arrow points to true positive. Orientation is chosen for the best visualization of the aneurysms. (a-c) 3D-RA data. (d-f) MRA data. (g-i) CTA data

tance is one or two voxels, usually at the end points [BST05]. As it is expected the presence of noise influences the accuracy of the medial axis [BST05]. Some of the false positive detection results are located on peripheral vessels (2-3 voxels in diameter). While 3D-RA has excellent signal-to-noise ratio, the signal intensity

is weaker in regions with small vessels compared to regions with main arteries and may influence the accuracy of the medial axis computation. At the same time, a half voxel discrepancy in medial axis computation has little impact when computing local neighborhoods in regions with wider vessels, but can result in incorrect local neighborhoods and false positive results in regions with much narrow vessels. For large, irregular aneurysms, the medial axis inside the aneurysm presents as a cluster of small branches rather than one branch, thus resulting in patches of positive results on the surface of the aneurysm as shown in Fig. 4.9(i). The algorithm would benefit from an automated grouping of the positive results describing the same aneurysm. This would yield larger region indexes for true positives and a more discriminant false positive reduction. For future work we plan to study how smoothing of the medial axis affects false positive rates. There is a risk that smoothing of the medial axis might decrease the method sensitivity by removing small branches describing true positives.

The detection method correctly identified the five fusiform aneurysms from the test data. These are biological fusiform aneurysms which present as uneven dilatations in multiple directions perpendicular to the vessel axis. These aneurysms result in short branches on the vasculature centerline. The method is unlikely to detect true radially symmetric fusiform aneurysms defined as local dilatations of an artery and having perfectly circular cross sections.

For future work, on a larger single modality database, we intend to improve false positive reduction using cross-validation for classification of the positive results taking into account features such as region index, estimated diameter, location on the vasculature and writhe number values.

Currently, the detection method requires an average of two minutes for a 3D-RA dataset and an average of eight minutes for MRA and CTA data on a desktop machine with an Intel Duo Core@2.66GHz CPU and 2GB of RAM. This excludes

segmentation time since we assume a segmented volume is given as input. On our particular data, we applied a combination of thresholding and region growing segmentation techniques which take less than one minute for all data. Currently the code contains no optimizations.

In terms of computational complexity, there is nothing inherently prohibitive in the proposed analysis, as all steps composing the detection method are computationally tractable. The local analysis work is highly parallelizable, and as such, is well suited to efficient implementation on advanced hardware such as multicore processors, FPGAs, ASICS, and GPUs. We are confident that code optimization and parallel programming will greatly decrease the required computation times and render the algorithm suitable for on-line use in clinical applications.

To assess the performance and utility of the aneurysm detection method in a clinical setting, we plan to perform a validation study, with and without computed-aided diagnostic systems assistance, to investigate the effect of our method on diagnostic accuracy. The detection of intracranial aneurysms is fraught by multiple confounding factors including the quality and age of the equipment available, the acquisition technique, patient cooperation, and clinician's expertise and state of alertness. Each of these factors is difficult to control or optimize on an ongoing basis. We believe an additional computational tool that would point the interpreting clinician to possible aneurysmal dilatations may be useful in improving diagnostic accuracy and reducing interpretation times.

Chapter 5

Rupture Status Classification of Intracranial Aneurysms using the Writhe Number of Surfaces

In this chapter, the theory behind the writhe number of surfaces is applied for rupture status classification of intracranial aneurysms. As described in Chapter 2, constant advancements in medical imaging during the last decades resulted in wide availability of imaging equipment and, as a consequence, increased patient access to such technologies. Asymptomatic unruptured intracranial aneurysms are now detected during routine evaluations, and the management and treatment of these lesions depends on assessing their risk of rupture. Following the methodology detailed in this chapter, the writhe number is used to describe and analyze the shape of the aneurysms in order to predict their rupture status.

5.1 Clinical Data

The clinical database used in this study consists of 117 cerebral aneurysms from 106 patient-derived 3D rotational angiography (3D-RA) datasets. Data were acquired using a biplane flat-detector digital subtraction angiography system (Axiom Artis, Siemens Medical Solutions, Malvern PA) at Tufts Medical Center, Department of Neurosurgery (Boston, MA). 3D-RA is a technique employed to visualize blood vessels in a bony or dense soft tissue environment. Contrast agent is injected through a catheter which is navigated from a percutaneous femoral arterial access into a carotid or vertebral artery (i.e. one of the vessels leading to the brain vasculature). Images acquired during the contrast agent are subtracted from images acquired pre-contrast. In the case of intracranial scanning, 3D-RA produces images with very high contrast between vasculature and the surrounding environment. In the current study, the size of each 3D-RA data volume is $128 \times 128 \times 128$ voxels with 0.48 mm isotropic voxels.

All aneurysms in this study are saccular aneurysms, berrylike outpouchings which appear mostly in the Circle of Willis and are dilatations of a vascular lumen caused by weakness of the vessel wall layers. The distribution of the aneurysms according to their specific location is shown in Table 5.1 together with the mean values of their largest diameter size derived from manual measurements in 3D space. In the table, aneurysms are classified into posterior communicating (PComA), anterior communicating (AComA), internal carotid (ICA), middle cerebral (MCA), ophthalmic artery (OpthA), internal carotid artery bifurcation (ICAB), basilar, anterior choroidal artery(AChA), vertebral (VA) and posterior inferior cerebellar artery (PICA). The average maximal size of the aneurysms in the database is 6.8 ± 3.1 mm.

It was recorded a priori which patients presented with subarachnoid hemorrhage (SAH) before the scan and the 117 aneurysms were classified as being ruptured (52 aneurysms) and unruptured (65 aneurysms).

Table 5.1: Aneurysms are classified according to their location. N is the number of aneurysms in each class. The mean value of the largest diameter size is presented for each class with the associated standard deviation.

Location	N	size[mm]
PComA	31	8.4±3.8
AComA	22	5.4±2.0
ICA	18	7.1±3.6
MCA	17	5.9±1.9
OpthA	8	7.5±3.7
ICAB	6	5.8±2.3
Basilar	6	7.4±2.4
ACHA	5	5.2±2.0
VA	3	5.9±1.0
PICA	1	8.1

Table 5.2: The number of ruptured and unruptured aneurysms in the whole database (SW+BF), and in sidewall (SW) and bifurcation (BF) subsets.

Type	Total	Ruptured	Unruptured
SW+BF	117	52	65
SW	58	23	35
BF	59	29	30

The aneurysms were further classified according to their location with respect to the parent vessels. The database contains 58 sidewall aneurysms (dilation of the artery in one direction perpendicular to the vessel axis) and 59 bifurcation aneurysms (dilation at the bifurcation of arteries). See Table 5.2 for details on the number of ruptured and unruptured aneurysms in each dataset. Fusiform aneurysms (dilation of the artery in multiple directions more or less perpendicular to the vessel axis) are not considered in this study given how different their pathology and morphology are from that of saccular aneurysms [BSN06, CCD$^+$07].

5.2 Method

5.2.1 Overview of the Classification Algorithm

The following methodology is proposed to differentiate between ruptured and unruptured cerebral aneurysms. First, the cerebral vasculature is segmented from the 3D-RA volume. For each aneurysm two separate 3D models are created, one in which the aneurysm is completely separated from the parent vessels and one in which parts of the adjacent vessels are included as shown in Fig. 5.1. These two surface models are represented as triangular meshes. Writhe numbers are computed along the surface of the models as described in Chapter 3, Section 3.1. As detailed in Chapter 2, kernel density methods are applied to the histogram of writhe numbers over each surface and statistics such as central moments, cumulants and entropy are computed for the estimated density function. These descriptors are used as classification features in predicting the risk of rupture in cerebral aneurysms. Each of these steps are presented below.

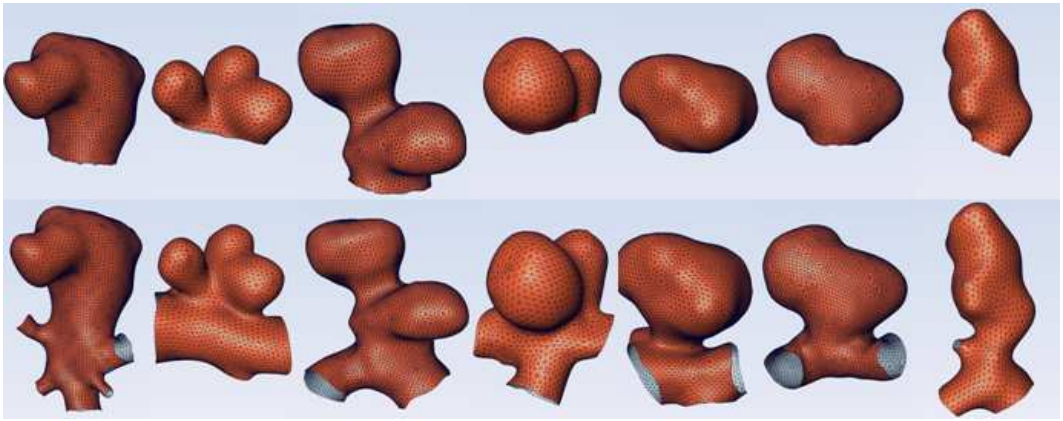

Figure 5.1: Aneurysm surfaces are analyzed both completely isolated from parent vessels and taking into account a portion of their adjacent vessels. They are represented as triangular meshes. Both bifurcation and sidewall aneurysms are considered. The top row shows isolated aneurysms. The bottom row shows the aneurysm attached to its corresponding parent vessels.

5.2.2 Segmentation

The proposed method requires a segmented volume of the cerebral vasculature. The appropriate segmentation method is highly dependent on the modality of the input data. In our case, 3D-RA data have high resolution and show high contrast between vasculature and the surrounding tissue (Fig. 5.2(a)). Segmentation is performed on all 106 volumes using a combination of thresholding and region-growing techniques [PXP00], applied with a commercial 3D visualization and modeling system (Amira, Mercury Systems, Chelmsford MA) (Fig. 5.2(b)). From the segmented volume, the surface of the vasculature is described as a triangular mesh (Fig. 5.2(c)).

As mentioned in Section 5.1, the voxel size of the image data is 0.48 mm, whereas the average size on the aneurysms is 6.8 ± 3.1 mm, thus guaranteeing a a well sampled representation of the geometry of the aneurysms. However, various segmentation methods may result in small shape variations and influence the classification accuracy. In order to determine the sensitivity of the method to segmentation, a second segmentation based on level sets [Set99, Whi98] is employed on a subset of 58 sidewall aneurysms, using a different visualization system (ITK-SNAP [YPC$^+$06]). The results of this robustness analysis are described in Section 5.3.2.

5.2.3 Isolation of Aneurysms

To allow for morphologic analysis, the aneurysm geometry is manually separated from the segmented vasculature. Each aneurysm is isolated from surrounding vessels in two steps as shown in Fig. 5.3.

First, the aneurysm is cut in such a way that its neck and a portion of the adjacent vessels are included in the model. The cut planes are empirically selected, the emphasis being on capturing the whole attachment area (i.e. the region where the aneurysm neck attaches to the parent vessels). Similarly to [MDMP$^+$07], each

parent vessel is cut at a distance approximately equal to its diameter, as measured at the aneurysm neck. The sensitivity of the classification to the cutting planes definition is discussed in Section 5.3.3.

Second, the aneurysm sac is completely isolated from all surrounding vessels as shown in Fig. 5.3(c). The cut plane is selected at the location where the aneurysmal sac pouched outward from the parent vessel [DTM+08]. The two resulting models are represented as triangular meshes as shown in Fig. 5.2.

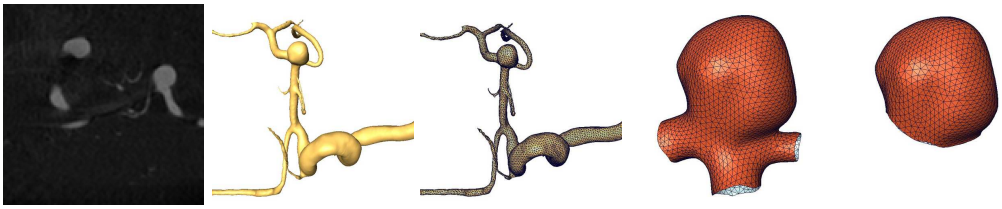

Figure 5.2: Segmentation and isolation of aneurysms. (a) Original 3D-RA data. (b) Cerebral vessels are segmented from surrounding tissue. (c) Segmented vessels are represented as a triangular mesh. (d) The aneurysm is separated from the vasculature and part of the adjacent parent vessels is included. (e) The aneurysm sac is completely separated from its parent vessels.

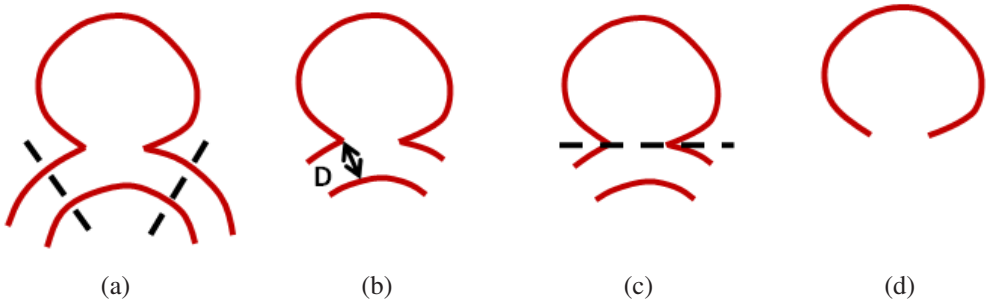

Figure 5.3: Isolation of the aneurysm geometry from the segmented vasculature (a) Cutting planes at parent vessels are selected and shown in dash lines. (b) The aneurysm is cut in such a way that its neck and a portion of the adjacent vessels are included in the model. Each parent vessel is cut at a distance approximately equal to its diameter D. (c) Cutting plane at the neck of the aneurysm is selected and shown in dash line. (d) The aneurysm sac is completely isolated from all surrounding vessels.

5.2.4 Writhe Number Computation

Given a triangular mesh representing an aneurysm, the writhe number is computed for each vertex $\mathbf{p} \in S$ on the aneurysm surface according to Eq. 3.3.

5.2.5 Histogram Statistics

As detailed in Chapter 2, Section 2.2, writhe number values along the surface of an aneurysm are represented using smoothed histograms. Statistics such as central moments, cumulants, and entropy are applied to the smoothed histogram to describe and analyze the distributions. Each aneurysm model is described by 10 attributes related to the writhe number distribution: the entropy (wh), central moments 2 to 8 ($w\mu_2$ to $w\mu_8$) and, cumulants 4 and 5 (wk_4 and wk_5). Note that cumulants order 1 to 3 are identical to the corresponding central moments. Consequently, each natural aneurysm is associated with 20 attributes, 10 describing the aneurysm sac and 10 describing the aneurysm with a portion of the parent vessels attached. These descriptors are used as classification features in predicting the rupture status in cerebral aneurysms.

5.2.6 Classification

The classification problem solved here involves 2 classes (ruptured vs. unruptured) and 117 samples (the aneurysms), described by 20 features each. The method used is logistic regression with 10-fold cross validation [FEH01]. The classification is repeated 10 times with 10 different random seeds. This results in 100 different splittings and the average performance is reported.

Classification is first performed on all 117 samples, then separately on 58 side-wall aneurysms and 59 bifurcation aneurysms. In each of these cases, first the aneurysm sac attributes are considered, then only the attributes from the aneurysm

with parent vessels attached are considered, and finally the total of 20 attributes are considered. The results of these nine different scenarios are described under classification results in Sec.5.3.1. To the best of our knowledge, this is the first study to perform morphological analysis on both aneurysm sac models and parent vessels models and compare prediction results between the two groups.

The best ratio between the number of features and the number of training samples is a controversial issue. A long standing statistical rule-of-thumb suggests that ten samples per feature are a minimum requirement for regression in order to avoid overfitting [Har84, FEH01]. To reduce the dimensionality of the feature space, sequential backward selection [SA04] was performed on the number of attributes considered for each of the nine classification scenarios. Details about the most significant attributes for each classification case are provided in Sec. 5.3.1.

5.3 Classification Results

5.3.1 Rupture Status Prediction

In this study, the rupture status prediction results obtained using writhe number analysis are compared with the prediction performance of the size and shape indexes described in Chapter 2, Section 2.3.2: aneurysm size, aspect ratio (AR), height-width (HW), bottleneck factor (BFN) ellipticity index (EI) undulation index (UI), non-sphericity index (NSI), area-averaged Gaussian and mean curvature (GAA, MAA), and L2 norm Gaussian and mean curvature (GLN, MLN).

Table 5.3 shows the accuracy for rupture prediction when these 11 size and shape indexes are considered on the whole set of 117 aneurysms (SW+BF) and on subsets of sidewall (SW) and bifurcation (BF) aneurysms respectively. All indexes perform much better on sidewall than on bifurcation aneurysms. This is consistent with recent research findings utilizing conventional aneurysm size and first-order

shape analysis (A.M. Malek, in review), that most of the currently used shape and size indexes give consistently better results predicting rupture in sidewall vs. bifurcation aneurysms. When each index is considered independently in univariate analysis, the rupture in sidewall aneurysms is best captured by NSI, MAA and GLN indexes (accuracy 77.1, 75.1, 69.3 respectively). Using similar analysis, the rupture in bifurcation aneurysms is best described by EI, UI and AR indexes (accuracy 62.7, 62.6 and 62.1 respectively). It is interesting to note that when the whole set of indexes is used to predict rupture status using multivariate analysis, the final results are not significantly improved compared to the best univariate results, for both sidewall and bifurcation subsets. Multivariate analysis results are also shown in Table 5.3. For sidewall aneurysms, multivariate statistics identified size, NSI and MAA as the best feature set associated with rupture. For bifurcation aneurysms, multivariate statistics identified AR, HW and UI as the best feature set associated with rupture. This suggests there is overlapping between indexes, with a number of indexes describing the same size or shape quality.

Table 5.4 summarizes the central results of the chapter, when writhe number analysis is applied to predict rupture status. Classification is performed on the three subsets: 117 SW + BF, 58 SW, and 59 BF aneurysms. For each subset, rupture status is predicted by considering first only aneurysm model (AM) features, second considering only parent vessel model (PVM) features, and third considering both AM and PVM features. These are the features previously detailed in Section 5.2.5. The sets of features taken into account for each particular classification case are marked with an X in the corresponding columns of the table. We distinguish between the features which are taken into consideration, and those which are ultimately used for classification. More specifically, as indicated at the end of Section 5.2.6, sequential backward selection is applied on the features taken into consideration to reduce the set to the five most significant features, which are the features

used for classification. While we are considering at most five features, some models may require less than five statistically significant features to completely describe the dataset. Using at most five features guarantees a samples-to-features ratio greater than ten. In turn, this reduces the risk that multivariate classification may overfit the data [Har84, FEH01].

Best prediction results are obtained when the classification is performed separately on sidewall and bifurcation aneurysms, respectively. The accuracy obtained using morphological analysis based on writhe number is of 86.7% for sidewall aneurysms and of 71.2% for bifurcation aneurysms. The results represent a significant increase in prediction accuracy for both subtypes, compared to when aspect ratio index was considered. Adding parent vessel information increased the prediction accuracy for sidewall aneurysms and proved essential for bifurcation aneurysms. Using writhe number analysis results in a significant increase in prediction accuracy when compared with the performance of any of the established indexes for both sidewall and bifurcation subtypes.

In terms of features, the entropy is part of all best features sets and it seems to be a significant quantity for both aneurysm subtypes. Ruptured aneurysms were consistently characterized by a higher mean entropy of the writhe number compared to unruptured aneurysms. Also, all best feature sets contain at least two of the variance, skewness and kurtosis central moments.

The differences between ruptured and unruptured aneurysms are apparent in Figures 5.5, 5.6, 5.7 and 5.8 which show analysis results on sidewall and bifurcation aneurysms, respectively. In the figures, we show the writhe number values along the surface of representative ruptured and unruptured aneurysms and their corresponding histograms. For sidewall aneurysms the results are shown on aneurysm dome models and for bifurcation aneurysms the results are illustrated on aneurysms with adjacent parent vessels attached. It can be seen from the histograms that unruptured

Table 5.3: Accuracy of rupture prediction when aspect ratio (AR), largest diameter size, height-width and aneurysm angle are used. The prediction is performed on three aneurysms sets: (1) 117 sidewall and bifurcation (SW+BF) aneurysms, (2) 58 sidewall (SW) aneurysms and (3) 59 bifurcation (BF) aneurysms

Type	N	Features	Accuracy %
SW+BF	117	Size	55.9
SW+BF	117	AR	63.6
SW+BF	117	HW	64.7
SW+BF	117	BNF	60.7
SW+BF	117	angle	49.7
SW+BF	117	EI	62.5
SW+BF	117	UI	62.3
SW+BF	117	NSI	66.9
SW+BF	117	GAA	51.9
SW+BF	117	MAA	62.4
SW+BF	117	GLN	56.5
SW+BF	117	MLN	56.4
SW+BF	117	HW, NSI	68.3
SW	58	Size	70.6
SW	58	AR	69.2
SW	58	HW	67.2
SW	58	BNF	67.9
SW	58	angle	53.6
SW	58	EI	61.6
SW	58	UI	68.6
SW	58	NSI	77.1
SW	58	GAA	64.2
SW	58	MAA	75.1
SW	58	GLN	69.3
SW	58	MLN	66.4
SW	58	Size, NSI	77.1
BF	59	Size	47.7
BF	59	AR	62.1
BF	59	HW	64.0
BF	59	BNF	55.0
BF	59	angle	48.1
BF	59	EI	62.7
BF	59	UI	62.6
BF	59	NSI	60.2
BF	59	GAA	48.7
BF	59	MAA	60.0
BF	59	GLN	40.0
BF	59	MLN	48.2
BF	59	AR, HW, UI	64.2

Table 5.4: Accuracy of rupture prediction when writhe number statistics are used. The prediction is performed on three aneurysms sets: (1) 117 sidewall and bifurcation (SW+BF) aneurysms, (2) 58 sidewall (SW) aneurysms and (3) 59 bifurcation (BF) aneurysms. For each set, rupture status is predicted by considering first only aneurysm model (AM) features, second considering only parent vessel model (PVM) features, and third considering both AM and PVM features. The set of features taken into account for each particular classification case are marked with an X. Sequential backward selection is applied to determine best features set.

Type	AM	PVM	Best Features AM	Best Features PVM	Accuracy %
SW+BF	X		$w\mu_2$, $w\mu_3$, $w\mu_4$, $w\mu_5$, wh		67.9
SW+BF		X		$w\mu_2$, $w\mu_7$, $w\mu_8$, wk_4, wh	68.3
SW+BF	X	X	$w\mu_2$, $w\mu_3$ $w\mu_5$	$w\mu_8$, wh	64.3
SW	X		$w\mu_2$, $w\mu_3$, $w\mu_8$, wk_5, wh		81.2
SW		X		$w\mu_4$, $w\mu_6$, $w\mu_7$, $w\mu_8$, wh	72.2
SW	X	X	$w\mu_2$, $w\mu_3$, $w\mu_8$	wk_5, wh	86.7
BF	X		$w\mu_2$, $w\mu_3$, wk_4, wk_5, wh		60.3
BF		X		$w\mu_3$, $w\mu_4$, $w\mu_8$, wk_5, wh	71.2
BF	X	X		$w\mu_3$, $w\mu_4$, $w\mu_8$, wk_5, wh	71.2

aneurysms have small skewness and small kurtosis (sharp distribution), while ruptured aneurysms tend to have high positive skewness and high kurtosis (flat distribution). Histograms with high positive skewness where the asymmetric tails extend toward large writhe numbers indicate the presence of high torque-related tension on the surface of the aneurysm as described in Section 3.3.1. The high tension regions are shown as red patches in the corresponding aneurysm figures. In terms of the mechanical interpretation of writhe in Section 3.3.1, ruptured aneurysms apparently show visibly higher ”tension” on their surfaces and we conclude that higher writhe number values are a predictor for rupture status.

Table 5.5 shows the prediction results when writhe number analysis and the existing 11 indexes are use together in a multivariate statistics context. For the sidewall subset only three features proved statistically significant: L2 norm of mean curvature MLN, the order 5 cumulant k_5 and the entropy h of the parent model. Using these three features resulted in 87.4 prediction accuracy. While there is not a statistically significant accuracy increase compared to using only writhe number

Table 5.5: Accuracy of rupture prediction when writhe number values are used together with the other size and shape indexes. The prediction is performed on the sidewall and bifurcation aneurysms sets. For each set, rupture status is predicted by considering writhe number aneurysm model (AM) features, writhe number parent vessel model (PVM) features, and the set of 11 size and shape indexes. The set of features taken into account for each particular classification case are marked with an X. Sequential backward selection is applied to determine best features set.

Type	AM	PVM	11 indexes	Best Features Selection	Accuracy %
SW	X	X	X	MLN, PVM: wk_5, wh	87.3
BF	X	X	X	PVM: $w\mu_3$, $w\mu_4$, $w\mu_8$, wk_5, wh	71.2

statistics, the best feature set has decreased from five features to three. This simplifies the statistical model and makes it more intuitive. For the bifurcation subset, adding the 11 indexes to writhe number analysis did not change the best feature set and consequently, did not change the prediction accuracy. The results reinforce the fact that parent vessel information is important when trying to understand aneurysm rupture for both sidewall and bifurcation subtypes. Writhe-based statistics have proved to be powerful features when compared to the more established indexes.

5.3.2 Sensitivity to Segmentation

In order to determine the sensitivity of the classification to segmentation, a subset of 58 sidewall aneurysms is segmented using two methods. As described in Section 5.2.2, the two methods used are region-growing thresholding [PXP00] and level-sets [Set99]. For this analysis only isolated aneurysm models (aneurysms completely separated from surrounding vessels) are considered. As shown in Table 5.6, the robustness analysis involves four classification cases: two in which the training and the testing sets are segmented using the same method, and two in which the training and the testing sets are segmented using different methods.

It is apparent from the table that the best results are obtained when both the

Table 5.6: Sensitivity of the classification to segmentation. The two segmentation methods used are region-growing thresholding and level sets. The study involves four classification cases: two in which the training and the testing sets are segmented using the same method, and two in which the training and the testing sets are segmented using different methods.

Train set	Test set	Best Features	Accuracy %
Threshold	Threshold	$w\mu_2$, $w\mu_3$, $w\mu_8$, wk_5, wh	81.2
Threshold	Level Sets	$w\mu_2$, $w\mu_3$, $w\mu_8$, wk_5, wh	76.8
Level Sets	Level Sets	$w\mu_2$, $w\mu_3$, $w\mu_7$,$w\mu_8$, wh	80.3
Level Sets	Threshold	$w\mu_2$, $w\mu_3$, $w\mu_7$, $w\mu_8$, wh	74.6

training and the testing sets are segmented using the same method. When this is the case, both segmentation methods result in similar classification accuracy ($\sim$80%), which is reassuring. Equally encouraging is the fact that the best feature sets are very similar in the two cases, with four overlapping features. Segmentation does influence the result of classification when the training and the testing sets are segmented differently. It is to be expected that depending on the different natures of the various edge- and region-based segmentation algorithms, they may give somewhat different results and consequently different information. Furthermore, many segmentation methods have one or more adjustable parameters which determine the granularity of the segmentation and different tuning of these parameters may lead sometimes to significantly different results [Zha97, ZFG05].

5.3.3 Sensitivity to Cutting Planes Definition

The sensitivity of the classification to cutting plane definition is investigated on four aneurysms. The aneurysms types are sidewall ruptured, sidewall unruptured, bifurcation ruptured, and bifurcation unruptured. All four aneurysms were correctly classified previously in Section 5.3.1. For this analysis, only models of aneurysms with attached parent vessels are considered, since these are the models affected by cutting plane definition. For each aneurysm, several models are created by using

three different cutting planes per parent vessel cut. The planes are roughly chosen at distances equal with 1.5, 1 and 0.5 of the vessel diameter as measured at the aneurysm neck. Cutting planes choices are shown in Fig. 5.4(a) and 5.4(f) for sidewall and bifurcation aneurysms respectively. A sidewall aneurysm results in nine models and a bifurcation aneurysm with three branches results in twenty-seven models. In the figure, the two most extreme models are shown for each aneurysm - when all adjacent vessels are cut using the outermost planes, and then all adjacent vessels are cut using the innermost planes. All other models fall between the two extreme models shown here.

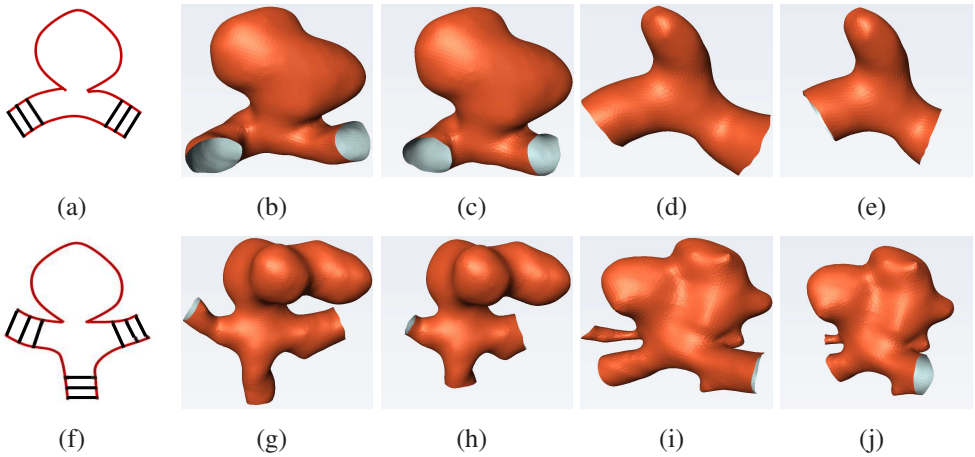

Figure 5.4: Sensitivity of the classification to cutting plane definition. Four aneurysms with parent vessels attached were cut using 3 different planes per parent vessel cut. (a) Sidewall aneurysm. Cutting planes options are shown in black. Combining the cutting planes result in 9 models. (b) SW ruptured: outermost planes used. (c) SW ruptured: innermost planes used. (d) SW unruptured: outermost planes used. (e) SW unruptured: innermost planes used.(f) Bifurcation aneurysm. Cutting planes options are shown in black. Combining the cutting planes result in 27 models. (g) BF ruptured: outermost planes used. (h) BF ruptured: innermost planes used. (i) BF unruptured: outermost planes used. (j) BF unruptured: innermost planes used.

The resulting aneurysm models were classified according to their type (SW or BF) using the best features sets from Table 5.4. All 72 models were correctly classified regardless of the cutting plane choices (Table 5.7). The results suggest the

Table 5.7: Sensitivity of the classification to cutting plane definition. Four aneurysms with parent vessels attached were cut using 3 different planes per parent vessel. N represents the resulting number of models for each aneurysm. The models are classified according to their type (SW or BF).

Type	Ruptured?	N	Correctly classified
SW	yes	9	9
SW	no	9	9
BF	yes	27	27
BF	no	27	27

classification based on writhe number analysis is not overly sensitive to cutting plane definition.

5.3.4 Synthetic Data Analysis

To give a better understanding on how the writhe number captures changes in the size and shape of aneurysms, writhe number analysis was performed on 11 synthetic aneurysm models. The synthetic models were created using a commercial 3D mechanical CAD software (Dassault Systemes SolidWorks Corp, Concord MA). The resulting mesh models were refined using the Harpoon automatic mesher (Sharc Ltd, Manchester UK). More specifically, the following size and shape changes are targeted: changes in the angle size between aneurysm and parent vessel (Fig. 5.9), changes in the aneurysm height and aneurysm neck as reflected by the aspect ratio index (Fig. 5.10) and changes in the aneurysm height and width as reflected by the height-width index (Fig. 5.11).

Figure 5.9 shows how the writhe number captures changes in the size of the inclination angle between aneurysm and parent vessel. Recent studies found the inclination angle to be statistically significant in predicting rupture status in sidewall aneurysms (A.M. Malek, in review). Figures 5.9(a) and 5.9(b) how aneurysms having inclination angles of 90 and 70 degree, respectively. It is apparent from both the writhe number values along the aneurysm surface and the corresponding his-

tograms that the writhe number values increase with deviations from the 90 degree angle.

Figure 5.10 shows how the writhe number captures changes in the aneurysm height and aneurysm neck as reflected by the aspect ratio index. The aspect ratio was found to be statistically significant in predicting rupture status in intracranial aneurysms [UTH$^+$99]. Figures 5.10(a) and 5.10(b) have aspect ratio indexes of 15 and 27.5, respectively. It is apparent from both the writhe number values along the aneurysm surface and the corresponding histograms that an increase in the aspect ratio results in an increase of the writhe number values.

Figure 5.11 shows how the writhe number captures changes in the aneurysm height and width as reflected by the height-width index. The aspect ratio was found to be statistically significant in predicting rupture status in intracranial aneurysms [DTM$^+$08]. Figures 5.11(a) and 5.11(b) have height-width indexes of 1.6 and 3.6, respectively. It is apparent from both the writhe number values along the aneurysm surface and the corresponding histograms that the writhe number is inversely proportional with the change in height-width ratio. This relation between the writhe number and the HW index holds even when the angle between the aneurysm and the parent vessel changes as shown in Fig. 5.11(e) and 5.11(f).

Synthetic data analysis suggests that size and shape changes described by aspect ratio, height-width and the inclination angle can all be represented using features based on writhe number. This may explain the very promising classification results reported on clinical data in Section 5.3.1.

5.4 Discussion

Subarachnoid hemorrhage as a consequence of aneurysm rupture is a life-threatening and debilitating event with high mortality and morbidity rates. While current clini-

cal practice relies mostly on size of the aneurysms as the main indicator for rupture, this study suggests that morphology is likely to play an important role in discriminating between ruptured and unruptured cerebral aneurysms. The morphological analysis in this work is based on writhe number distributions on the surface of aneurysms. To the best of our knowledge this is the first study using 3D shape descriptors derived from the writhe number statistics. The writhe number captures subtle changes on the surface of the aneurysms and, through the analogy with the torque, lends a a physically intuitive interpretation.

The results show that ruptured aneurysms tend to have regions of high torque-related tension on their surface, which is indicated by writhe number distribution spreading out over a larger writhe number range. We believe regions of high tension correspond to convoluted, highly asymmetrical surfaces. These qualities seem to be captured by the writhe number and to play a role in predicting rupture status. For future work, we plan to study how the writhe of surfaces can provide an objective, quantitative measure of these somewhat subjective qualities describing the complexity of a shape.

This study is performed both on isolated aneurysmal dome models and on combined models incorporating the attached adjacent parent vessel region. When only the aneurysmal dome is considered, the accuracy of risk prediction yields encouraging results on the sidewall aneurysm subset but performs poorly on bifurcation aneurysm subset (81.2% vs. 60.3% accuracy). Incorporating parent vessel information into the prediction process results in a significant increase in accuracy. This increase is especially apparent for bifurcation aneurysms, where the most important classification features are derived from the combined dome and parent vessel models. This would suggest that the relation between the aneurysm and the adjacent vessels is a better indicator of rupture compared to the shape of the aneurysm sac in the bifurcation subset. Still, this morphological analysis captures the rupture risk

of sidewall aneurysms much better than that of bifurcation aneurysms (86.7% vs. 71.2% accuracy). There seems to be a morphological split between sidewall and bifurcation aneurysms which is supported by recent research in our lab using two-dimensional shape descriptors such as the aspect ratio index, height-width ratio, and inflow-angle into the aneurysm dome (A.M. Malek, unpublished data). These findings suggest that the shape and size may not be enough to accurately predict rupture in bifurcation aneurysms. Other patient-specific factors such as aneurysm location, patient age and gender may need to be explored and incorporated into the analysis.

Robustness analysis shows the classification to be insensitive to segmentation as long as the same method is used on both the training and the testing sets (Table 5.6). The classification is sensitive to segmentation when the training and testing sets are segmented using different methods. Segmentation of cerebral vasculature is a challenging task and the research in the field remains active [FPAB04, HF07, RP09]. It is beyond the scope of this research to improve segmentation algorithms or to compare the performance of the various methods. Currently, our recommendation is to use compatible training and testing methods for rupture classification.

When creating aneurysm models with parent vessels attached, the cutting planes are chosen somewhat arbitrary. We do not know of the existence of a comprehensive study to recommend a methodology on how to create these models. The analysis from Section 5.3.3 suggests the classification based on writhe number is relatively impervious to cutting plane definitions. However, since incorporating parent vessel information improves the prediction results, it would be worth exploring the effect of cutting plane definition on a larger set of both correctly classified and misclassified aneurysms.

The isolation of the aneurysms is the only part of the method that is not completely automated. For future work, we plan to investigate how to incorporate into

this current work the results presented in Chapter 4, where aneurysms are automatically detected from the whole cerebral vasculature.

The prediction results obtained when using the writhe number together with other indexes show that writhe number statistics are powerful tools, acting as aggregate features which may encompass characteristics of other existing shape and size indexes. This notion is supported by preliminary synthetic data analysis. Future work should further the synthetic data analysis to determine how writhe number statistics fit into the pool of existing morphological features describing intracranial aneurysms.

Similar to previous morphological research, the current study premise is based on an yet unproven assumption that aneurysms do not change shape and size upon rupture [UTH+99, MHR04, RMH05, MDMP+07]. This is still a point of contention and there is not enough information to decidedly settle the debate. Some studies report no major change in size and shape after rupture [UTH+99, BReB+03], whereas the ISUIA study [Wie03] contends that ruptured aneurysms data should not be used to draw conclusions about unruptured aneurysms evolution.

Similar to previous morphological research, the current analysis is performed on a dataset of aneurysms which were classified as being ruptured or not at the time of detection. The evolution of these aneurysms was not followed clinically over a period of time. As such we differentiate between predicting aneurysms rupture status and predicting rupture likelihood. Prospective studies, where in-vivo aneurysms are followed over long periods of time until they rupture or not, would determine if the writhe number usefulness can be extended from predicting rupture status to determining rupture likelihood.

While the analysis was performed on a relatively large database and the results are very encouraging, the eventual added value of the method remains to be determined in the clinical setting and, as mentioned above, would require validation in

prospective clinical trials.

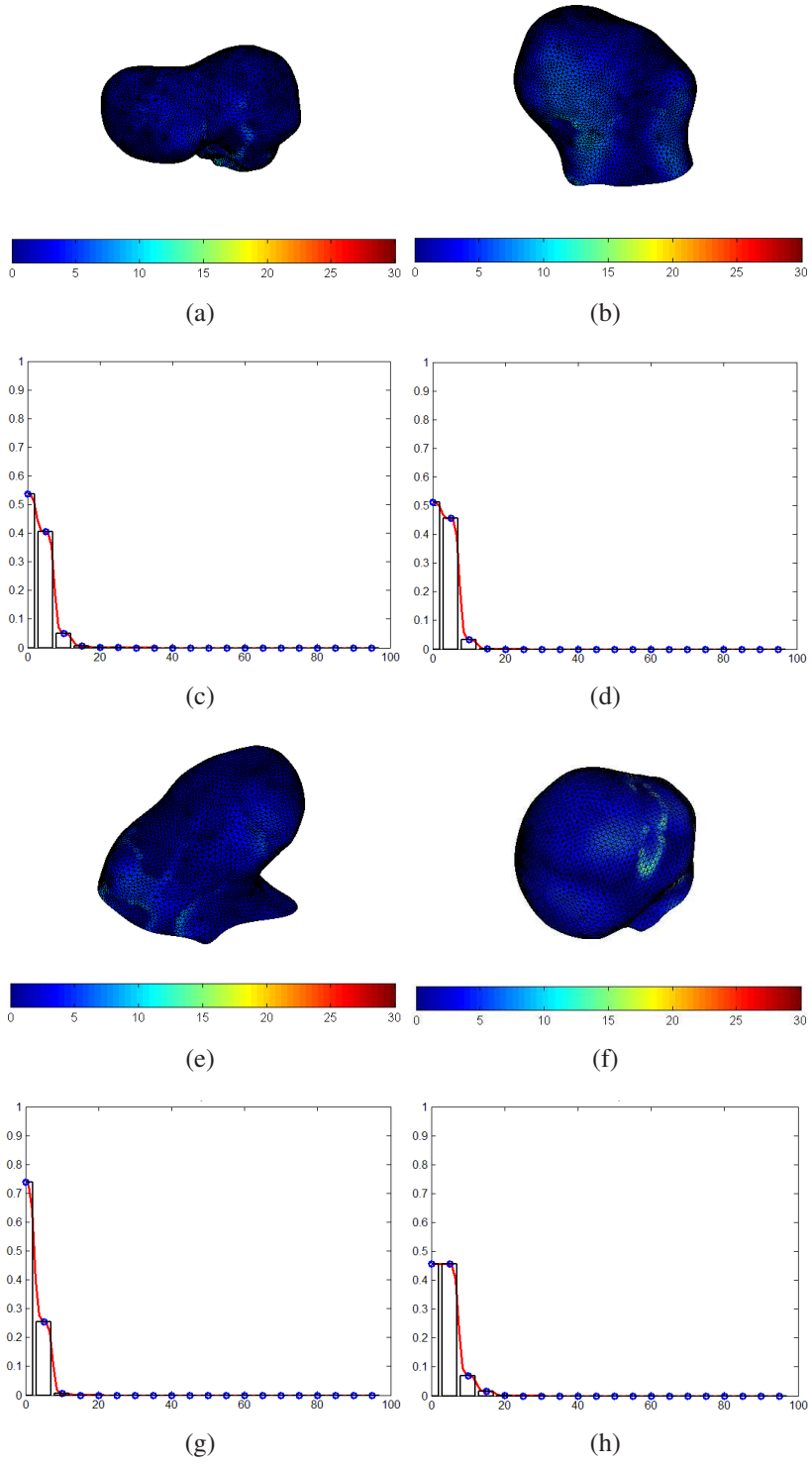

Figure 5.5: Analysis results on four representative unruptured SIDEWALL aneurysms. The results are shown on aneurysm dome models. (a),(b),(e),(f) Unruptured aneurysms. Writhe number values along the surface. Low values are interpreted as low surface tension. (c),(d),(g),(h) Corresponding histograms. The approximating probability distribution is shown in red. Unruptured aneurysms have sharp writhe number distributions, low entropy and low skewness.

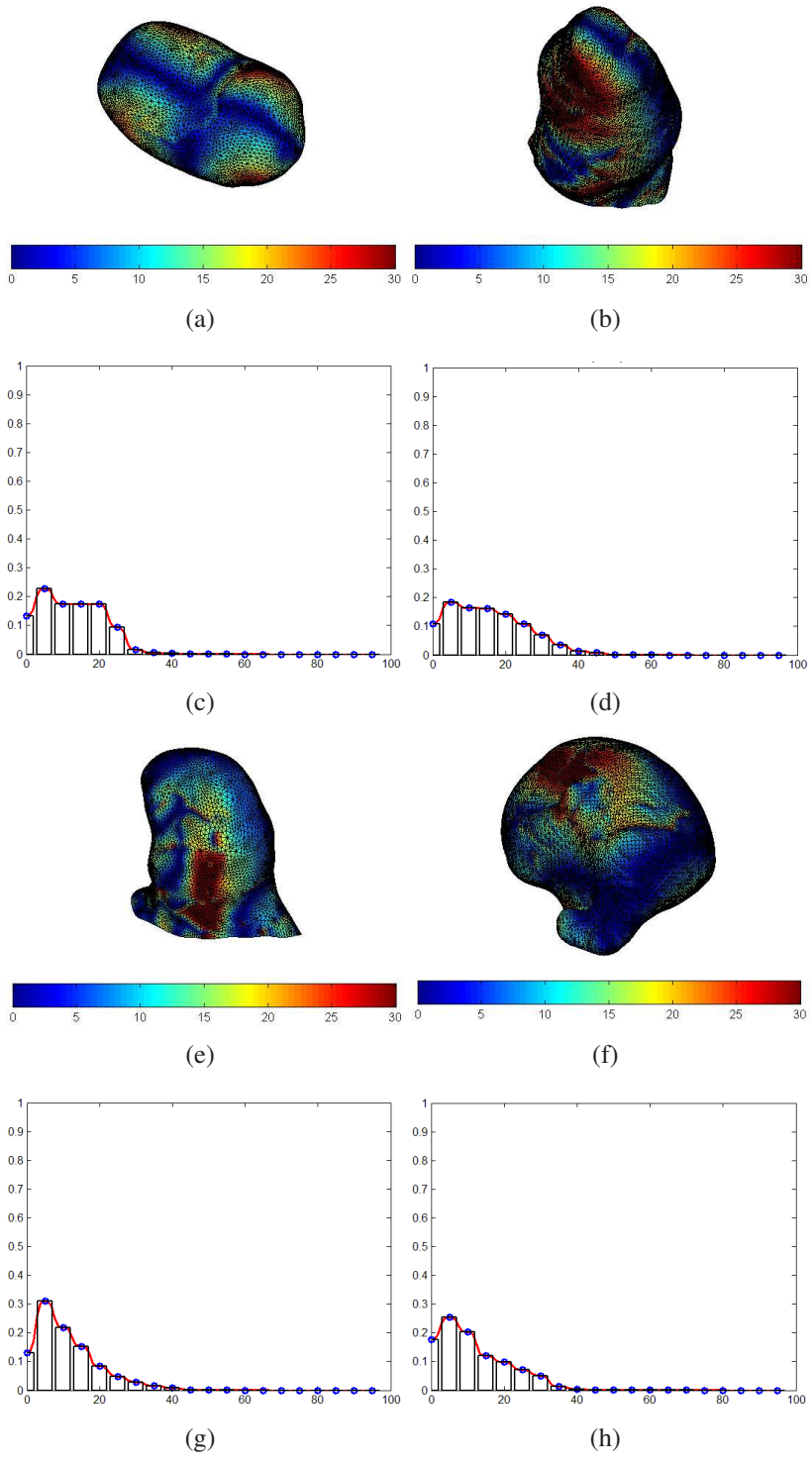

Figure 5.6: Analysis results on four representative ruptured SIDEWALL aneurysms. The results are shown on aneurysm dome models. (a),(b),(e),(f) Ruptured aneurysms. Writhe the number values along the surface. High values are interpreted as high surface tension and are a predictor for rupture. (c),(d),(g),(h) Corresponding histograms. The approximating probability distribution is shown in red. Ruptured aneurysms have more spread writhe the number distributions, high entropy and high skewness.

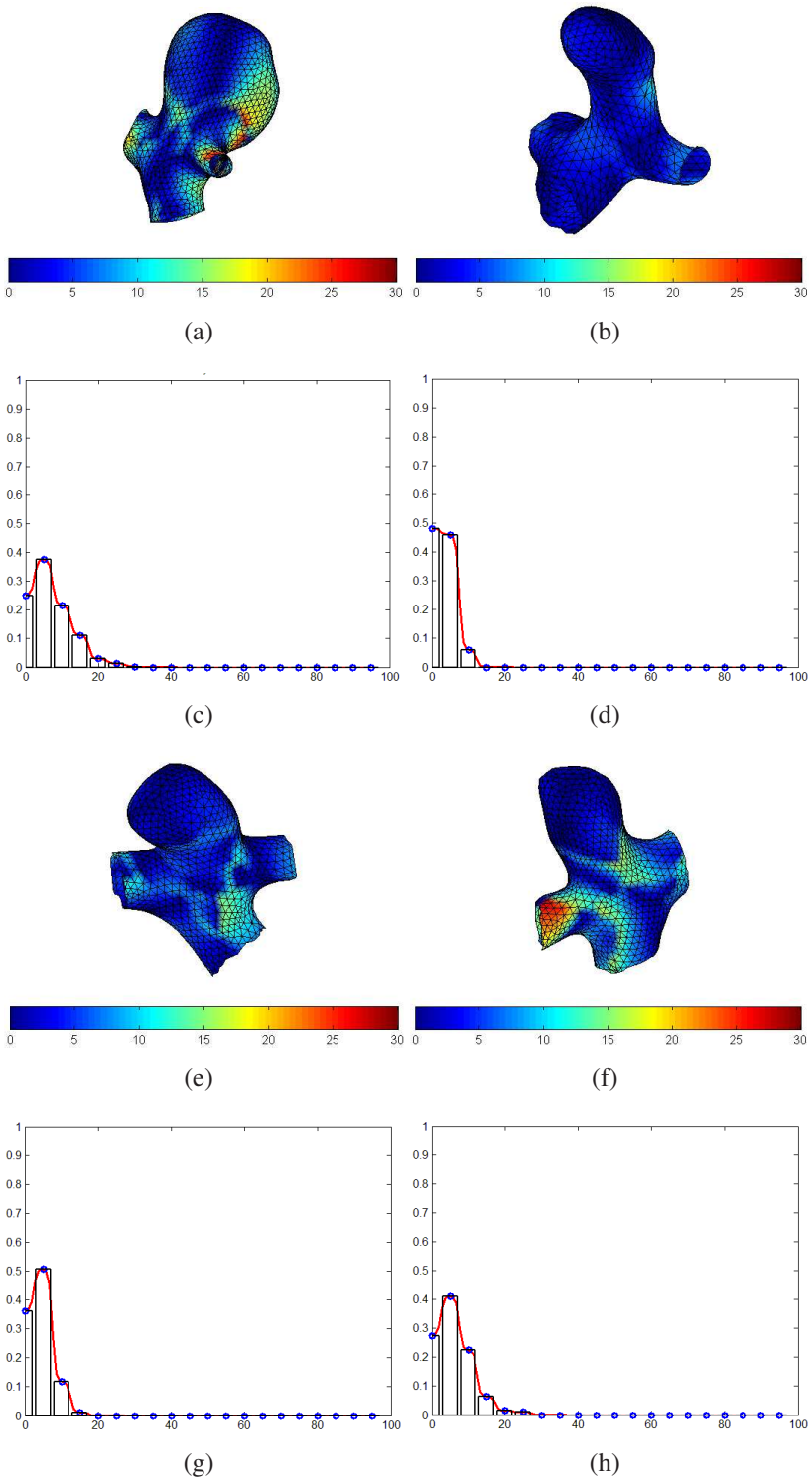

Figure 5.7: Analysis results on four representative unruptured BIFURCATION aneurysms. The results are illustrated on aneurysms with adjacent parent vessels attached. (a),(b),(e),(f) Unruptured aneurysms. Writhe number values along the surface. Low values are interpreted as low surface tension. (c),(d),(g),(h) Corresponding histograms. The approximating probability distribution is shown in red. Unruptured aneurysms have sharp writhe number distributions, low entropy and low skewness.

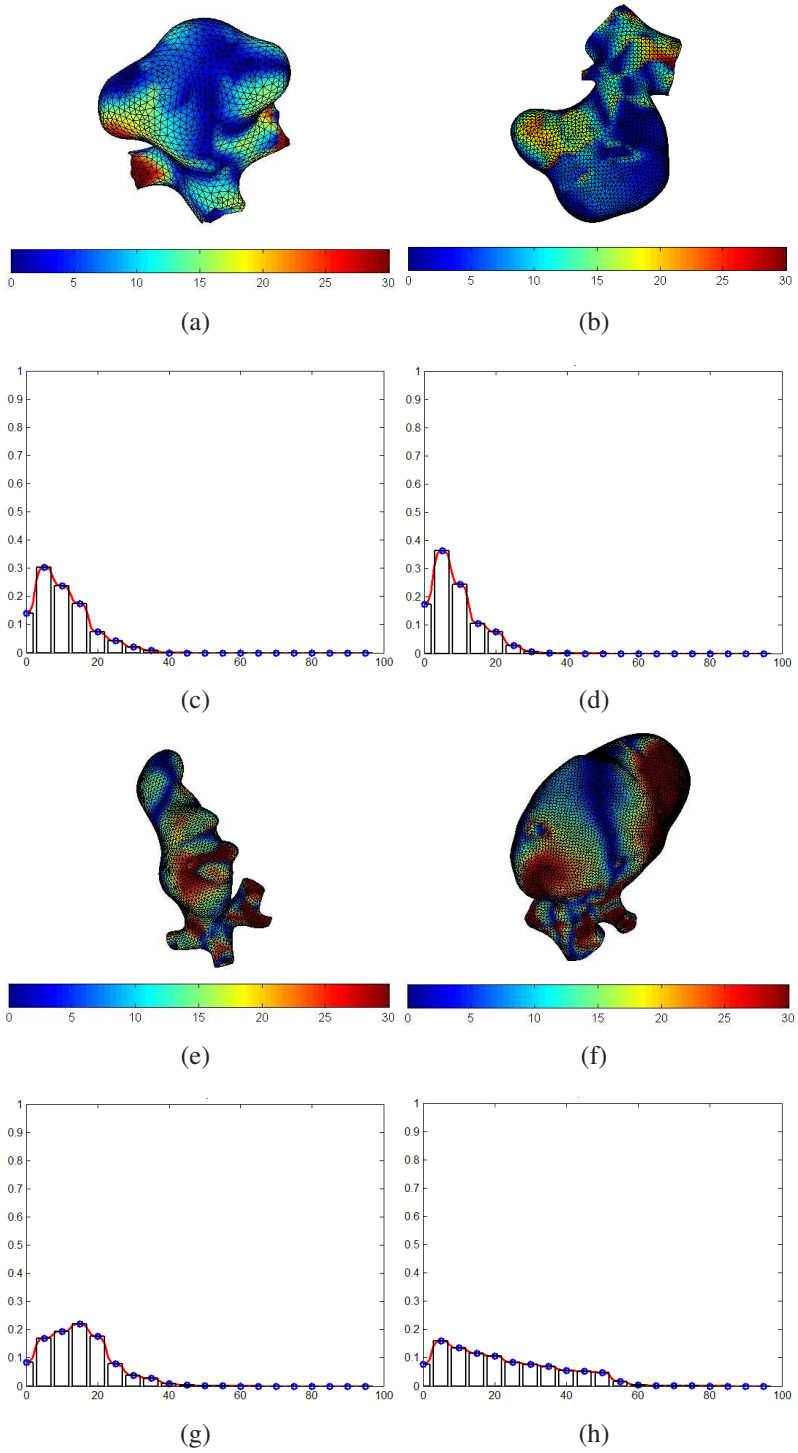

Figure 5.8: Analysis results on four representative ruptured BIFURCATION aneurysms. The results are illustrated on aneurysms with adjacent parent vessels attached. (a),(b),(e),(f) Ruptured aneurysms. Writhe the number values along the surface. High values are interpreted as high surface tension and are a predictor for rupture. (c),(d),(g),(h) Corresponding histograms. The approximating probability distribution is shown in red. Ruptured aneurysms have more spread writhe the number distributions, high entropy and high skewness.

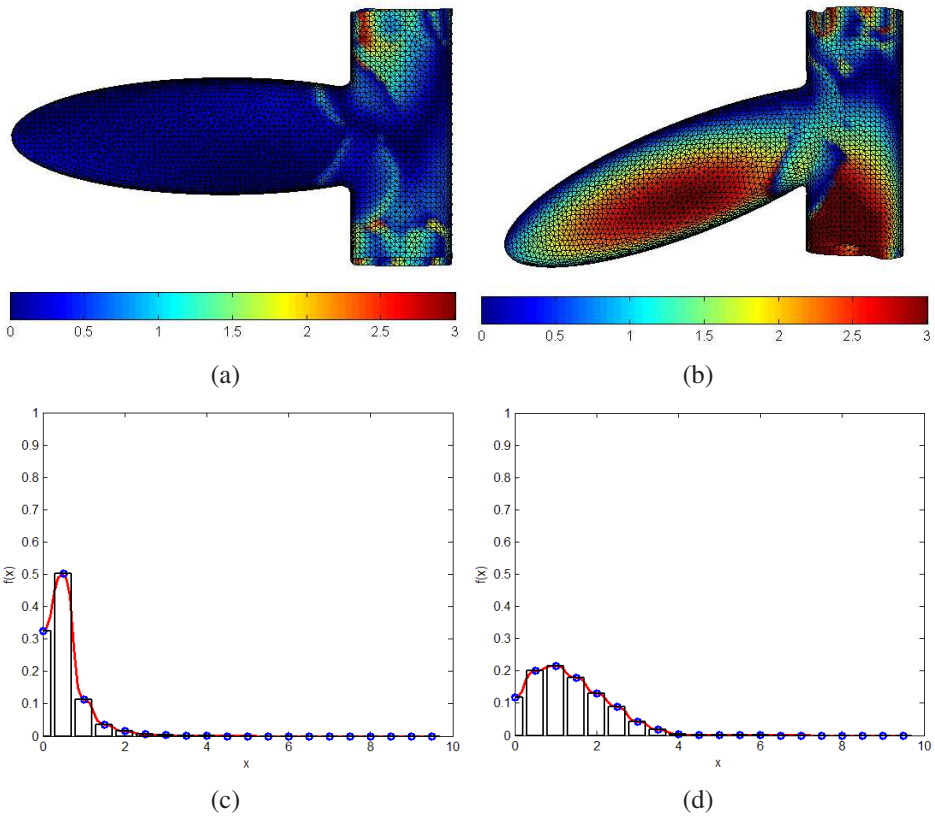

Figure 5.9: Analyze how the writhe number captures changes in the size of the angle between aneurysm and parent vessel. (a) The aneurysm makes a 90 degrees angle with its parent vessel. (b) The aneurysm makes a 70 degrees angle with its parent vessel. (c), (d) Corresponding histograms. It is apparent from both the writhe number values along the aneurysm surface and the corresponding histograms that the writhe number is proportional with deviations from the 90 degree angle.

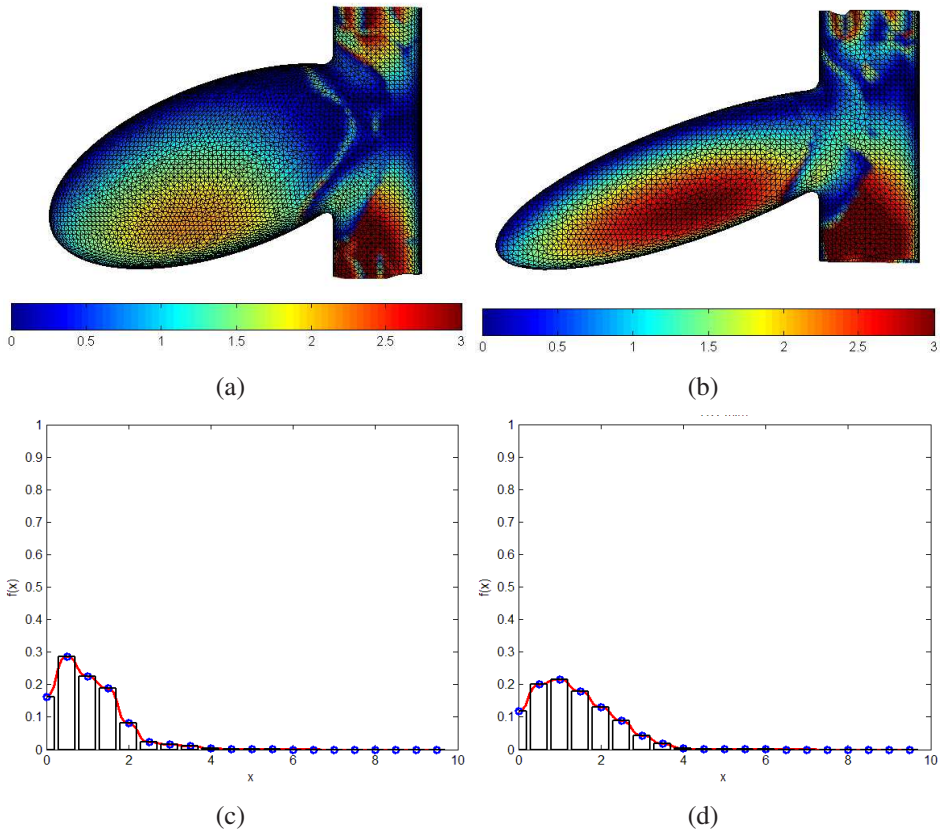

Figure 5.10: Analyze how the writhe number captures changes in the size of the aneurysm height and the width neck as reflected by the aspect ratio index. (a) The aneurysm has an aspect ratio of 15. (b) The aneurysm has an aspect ratio of 27.5. (c), (d) Corresponding histograms. It is apparent from both the writhe number values along the aneurysm surface and the corresponding histograms that the writhe number is proportional with the change in aspect ratio.

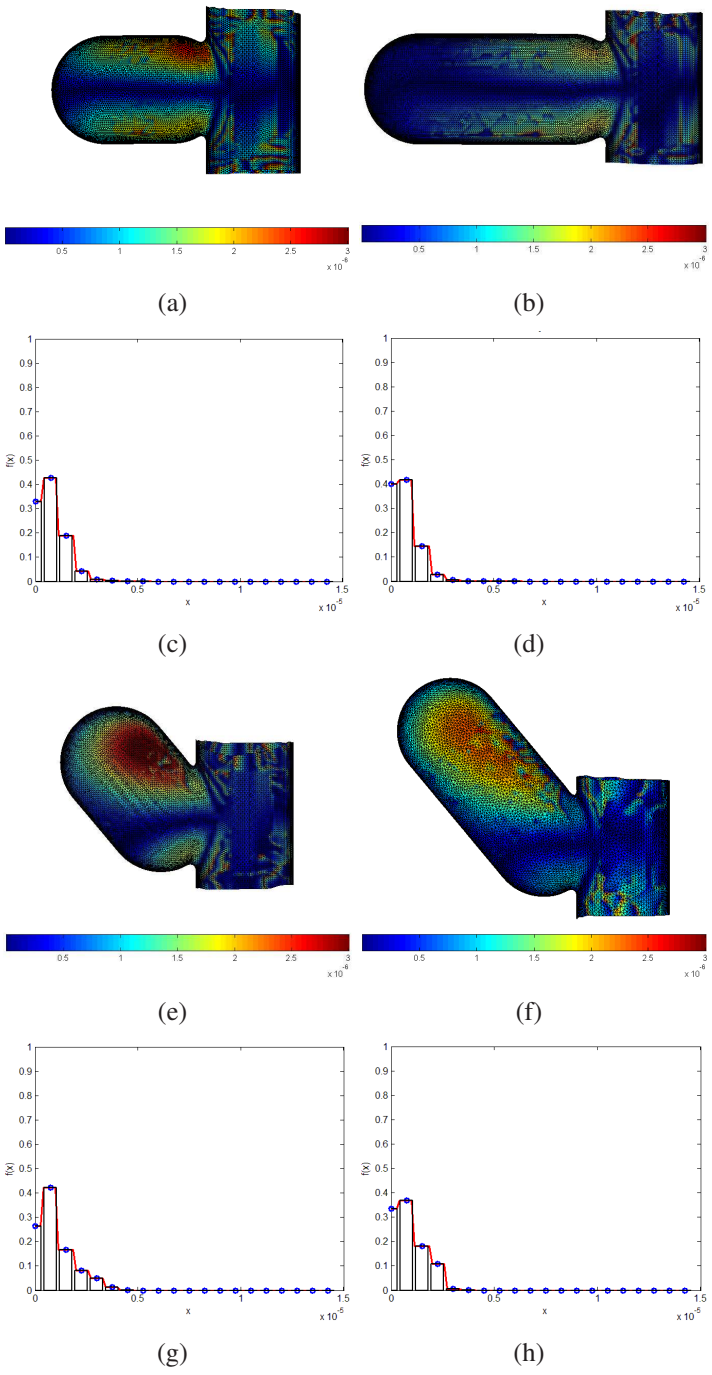

Figure 5.11: Analyze the relation between the writhe number and the aneurysm hight-width ratio (HW). (a) HW = 1.6 (b) HW = 3.6 (c), (d) Corresponding histograms. (e) HW = 1.6 and the inclination angle = 110 degrees. (f) HW = 3.6 and the inclination angle = 110 degrees. (g), (h) Corresponding histograms. It is apparent from both the writhe number values along the aneurysm surface and the corresponding histograms that the writhe number is inverse proportional with the change in HW. This correlation is true even when the angle between the aneurysm and the parent vessel changes.

Chapter 6

Rupture Status Classification of Intracranial Aneurysms using Surface Curvature and the Centroid-Radii Model

In this chapter, the usefulness of surface curvature and the centroid-radii model is investigated for rupture status prediction of intracranial aneurysms. The analysis is performed on the same aneurysm database described in Chapter 5.

6.1 Method

6.1.1 Overview of the Classification Algorithm

The methodology used in this chapter follows the steps detailed in Chapter 5. Cerebral vasculature is segmented and aneurysm models are created. Each aneurysm is described by two triangular models, with and without inclusion of parent vessel. Gaussian and mean curvatures, and centroid-radii distances are computed along the

surface of the aneurysm models. Histogram statistics are computed from the histograms representing distributions of curvatures and centroid-radii distances. Statistics derived from surface curvature and centroid-radii models are used to differentiate between ruptured and unruptured aneurysms first by themselves and then in combination with writhe number and other previously introduced indexes.

6.1.2 Segmentation

Similar to Chapter 5, image segmentation is performed using a combination of thresholding and region-growing techniques. In order to analyze the sensitivity to segmentation of the classification based on curvature and centroid-radii model, a second segmentation based on level-sets is employed on a subset of 58 sidewall aneurysms. The results of the analysis are presented in Section 6.2.2.

6.1.3 Isolation of Aneurysms

The aneurysm geometry is separated manually form the segmented vasculature. Two 3D models are created for each aneurysm. First, each parent vessel is cut at a distance approximately equal to its diameter, as measured at the aneurysm neck. Second, aneurysms are completely separated from adjacent parent vessels. The sensitivity to the cutting planes definition of the classification based on curvature and centroid-radii model is discussed in Section 6.2.3.

6.1.4 Surface Curvature and Centroid-Radii Computation

Gaussian and mean curvatures are computed along the surface of the models as described in Chapter 2, Section 2.1.3. Similarly, centroid-radii distances are computed as described in Chapter 2, Section 2.3.2. The centroid-radii distances are only computed on models representing the aneurysm sac completely separated from the

adjacent vessels.

6.1.5 Histogram Statistics

As detailed in Chapter 2, Section 2.2, Gaussian and mean curvatue values along the surface of an aneurysm are represented using smoothed histograms. Similarly, centroid-radii distances are computed for each point on the aneurysm surface and are represented as smoothed histograms. For each aneurysm model is described by the following attributes: 10 Gaussian curvature-related features (central moments $g\mu_2$ to $g\mu_8$, cumulants gk_4 and gk_5, entropy gh), 10 mean curvature-related features (central moments $m\mu_2$ to $m\mu_8$, cumulants mk_4 and mk_5, entropy mh) and 10 centroid-radii-related features (central moments $c\mu_2$ to $c\mu_8$, cumulants ck_4 and ck_5, entropy ch). Given that centroid-radii distances are only computed on the aneurysm sac model, each natural aneurysm is associated with 50 attributes, 30 describing the aneurysm sac and 20 describing the aneurysm with portion of the parent vessels attached. These descriptors are used as classification features in predicting the rupture status in cerebral aneurysms.

6.1.6 Classification

The classification problem solved here involves two classes (ruptured vs. unruptured) and 117 samples (the aneurysms), described by 50 features each. The method used is logistic regression with 10-fold cross validation [FEH01]. The classification is repeated 10 times with 10 different random seeds. This results in 100 different splittings and the average performance is reported.

Classification is first performed on all 117 samples, then separately on 58 sidewall aneurysms and 59 bifurcation aneurysms. In each of these cases, first the aneurysm sac attributes are considered, then only the attributes from aneurysm with parent vessels attached are considered, and finally the total of 50 attributes are con-

sidered. The analysis is further divided according to the nature of the attributes (curvature-based attributes and centroid-radii based attributes). The results of these different scenarios are described under classification results in Sec.6.2.1.

To reduce the dimensionality of the feature space and to insure a good samples-to-features ratio, sequential backward selection [SA04] was performed on the number of attributes considered for each of the nine classification scenarios. Details about the most significant attributes for each classification case are provided in Sec.6.2.1.

6.2 Classification Results

6.2.1 Rupture Status Prediction

Table 6.1 shows the classification results when centroid-radii analysis is applied to predict rupture status. Classification is performed on the three subsets: 117 SW + BF, 58 SW, and 59 BF aneurysms. Since centroid-radii distances are computed only for aneurysm sac models, the aneurysm model (AM) features are marked with an X in the corresponding columns of the table. These are the features previously detailed in Section 6.1.5. In this study, the features which are taken into consideration are distinguished those which are ultimately used for classification. More specifically, sequential backward selection is applied on the features taken into consideration to reduce the set to the five most significant features, which are the features used for classification. Using at most five features guarantees a samples-to-features ratio greater than ten. In turn, this reduces the risk that multivariate classification may overfit the data [Har84, FEH01]. Note that while we are considering at most five features, some models may require less than five statistically significant features that completely describe the dataset. The centroid-radii statistics model works very well on sidewall aneurysms (80.3% accuracy) using only one feature, namely the

entropy of the centroid-radii distance distribution. On the bifurcation subset, the accuracy is 70.0% using the entropy and the variance of the centroid-radii distance distribution. While lower than the prediction accuracy for sidewall aneurysms, this result is still better than when using any of the existing 11 indexes (Table 5.3) and comparable to the results when using writhe number statistics (Table 5.4). The morphological dichotomy between sidewall and bifurcation, which was mentioned in the previous chapter, it is also apparent from these results.

Table 6.2 shows the classification results when curvature analysis is applied to predict rupture status. For sidewall aneurysms, best prediction results are obtained when curvature features from both aneurysm and parent vessel models are considered (accuracy 77.1%). For bifurcation aneurysms, using parent vessel information results in a big accuracy increase compared to when using only aneurysm model data (55% to 73.5%).

Table 6.3 shows the prediction results when the analysis takes into account all features described in this study - writhe number, mean and Gaussian curvature, centroid-radii model and the 11 existing indexes. Groups of features taken into account are marked with an X in the corresponding columns. For sidewall aneurysms, the entropy of the centroid-radii model remains a strong feature and best accuracy results are obtain when combining centroid-radii entropy with writhe number statistics (88.4%). For bifurcation aneurysms, combining mean curvature derived statistics with centroid-radii statistics results in 79.8% accuracy. This represents a 25% accuracy improvement compared to using the 11 established size and shape indexes described in Chapter 2, Section 2.3.2. It is obvious from Table 6.3 that the entropy of a distribution is an important statistical measure regardless of the surface property (writhe number, mean curvature or centroid-radii distances). The entropy is part of all best features sets and it seems to be a significant quantity for both aneurysm subtypes. Ruptured aneurysms were consistently characterized by

Table 6.1: Accuracy of rupture prediction when centroid-radii statistics are used. The prediction is performed on three aneurysms sets: (1) 117 sidewall and bifurcation (SW+BF) aneurysms, (2) 58 sidewall (SW) aneurysms and (3) 59 bifurcation (BF) aneurysms. Rupture status is predicted by considering only aneurysm model (AM) features. Sequential backward selection is applied to determine best features set.

Type	N	AM	Best AM	Accuracy %
SW+BF	117	X	$c\mu_2$, ch	66.6
SW	58	X	ch	80.3
BF	59	X	$c\mu_2$, ch	70.0

Table 6.2: Accuracy of rupture prediction when centroid-radii statistics are used. The prediction is performed on three aneurysms sets: (1) 117 sidewall and bifurcation (SW+BF) aneurysms, (2) 58 sidewall (SW) aneurysms and (3) 59 bifurcation (BF) aneurysms. Rupture status is predicted by considering only aneurysm model (AM) features. Sequential backward selection is applied to determine best features set.

Type	AM	PVM	Best AM	Best PVM	Accuracy %
SW+BF	X		gk_4, gk_5, gh, $m\mu_5$, $m\mu_8$		58.9
SW+BF		X		$g\mu_3$, gh, $m\mu_2$, $m\mu_6$, mh	64.5
SW+BF	X	X		$g\mu_3$, gh, $m\mu_2$, $m\mu_6$, mh	64.5
SW	X		$g\mu_5$, $g\mu_6$, $m\mu_2$, $m\mu_5$, mk_4		75.4
SW		X		$g\mu_2$, $g\mu_8$, $m\mu_2$, $m\mu_4$	73.6
SW	X	X	$g\mu_5$	$g\mu_2$, $m\mu_2$, $m\mu_4$	77.1
BF	X		gk_4, gk_5, gh, $m\mu_2$, $m\mu_3$		55.0
BF		X		$g\mu_5$, $p\mu_3$, $m\mu_6$, $m\mu_7$, mh	73.3
BF	X	X		$g\mu_5$, $p\mu_3$, $m\mu_6$, $m\mu_7$, mh	73.3

a higher mean entropy of both the mean curvature and the centroid-radii distances compared to unruptured aneurysms.

The differences between ruptured and unruptured aneurysms as captured by the centroid-radii model are apparent in Figures 6.1 and 6.2 which show analysis results on sidewall aneurysms. In the figures, we show the centroid-radii distances along the surface of representative ruptured and unruptured aneurysms and their corresponding histograms. The results are shown on aneurysm dome models. It can be seen from the histograms that unruptured aneurysms have small skewness and small kurtosis (sharp distribution), while ruptured aneurysms tend to have high positive

Table 6.3: Accuracy of rupture prediction when all size and shape aneurysm attributes are taken into account: curvature statistics, centroid-radii model statistics(CR-M), writhe number statistics and the 11 established size and shape indexes. The prediction is performed on the sidewall and bifurcation aneurysms sets. The statistical model takes into account both aneurysm model (AM) features and parent vessel model (PVM) features. The set of features taken into account for each particular classification case are marked with an X. Sequential backward selection is applied to determine best features set.

Type	Curvature	CR-M	11 indexes	writhe	Best Features Selection	Accuracy %
SW	X	X			ch	80.3
SW	X	X	X		ch	80.3
SW	X	X	X	X	ch, PVM: wk_5, wh	88.4
BF	X	X			$c\mu_2$, ch, PVM: mh	78.3
BF	X	X	X		MAA, $c\mu_2$, PVM: mh	79.8
BF	X	X	X	X	MAA, $c\mu_2$, PVM: mh	79.8

skewness and high kurtosis (flat distribution). Ruptured aneurysms have significantly higher entropy of the centroid-radii distance distribution, when compared to unruptured aneurysms. Note from the two figures that some of the ruptured and unruptured aneurysms have very similar sizes, but the entropy of the centroid-radii model captures information about both the size and the shape of the aneurysms, and as such, it can differentiate rupture status among similar size aneurysms.

Figures 6.3 and 6.4 show the differences between ruptured and unruptured bifurcation aneurysms as captured by the mean curvature. In the figures, we show the mean curvature along the surface of representative ruptured and unruptured bifurcation aneurysms and their corresponding histograms. The results are shown on aneurysms with adjacent parent vessels attached. It can be seen from the histograms that unruptured aneurysms have small skewness and small kurtosis (sharp distribution), while ruptured aneurysms tend to have high positive skewness and high kurtosis (flat distribution). Rupture aneurysms have significantly higher entropy of the mean curvature distribution, when compared to unruptured aneurysms.

6.2.2 Sensitivity to Segmentation

In order to determine the sensitivity of the classification to segmentation, a subset of 58 sidewall aneurysms is segmented using two methods, region-growing thresholding [PXP00] and level-sets [Set99]. For this analysis only isolated aneurysm models (aneurysms completely separated from surrounding vessels) are considered. The robustness analysis involves four classification cases: two in which the training and the testing sets are segmented using the same method, and two in which the training and the testing sets are segmented using different methods.

Table 6.4 shows the robustness analysis when classification is based on statistics derived from the centroid-radii model. It is apparent from the table that the entropy of the centroid-radii distances distribution is very robust to segmentation and similar results are obtained regardless of the segmentation method used on training and testing data ($\sim$80%). Distances from centroid to the surface of the aneurysms are less sensitive to the small variation between segmentation methods and are more robust to different degrees of smoothness of the surface.

Table 6.5 shows the robustness analysis when classification is based on statistics derived from surface curvature. As expected surface curvature is very sensitive to the segmentation method. Accuracy results between the two segmentation methods are similar when both the training and the testing data sets are segmented using the same method ($\sim$72%). However, the accuracy decreases dramatically when the two set are segmented using different methods ($\sim$57%). Because both the Gaussian and the mean curvatures are computed over a small local neighborhood on the surface of the aneurysm, they are very sensitive to changes in the smoothness of the surface. It is to be expected that depending on the different natures of the various edge- and region-based segmentation algorithms, they may give somewhat different results and the surface curvature seems to be sensitive to these differences. Furthermore, many segmentation methods have one or more adjustable parameters which deter-

Table 6.4: Sensitivity of the classification based on centroid-radii model to segmentation. The study involves only sidewall aneurysms and takes into account features derived from aneurysm models (AM) only. The two segmentation methods used are region-growing thresholding and level sets. The study involves four classification cases: two in which the training and the testing sets are segmented using the same method, and two in which the training and the testing sets are segmented using different methods.

Train set	Test set	Best Features AM	Accuracy %
Threshold	Threshold	ch	80.3
Threshold	Level Sets	ch	79.7
Level Sets	Level Sets	ch	81.7
Level Sets	Threshold	ch	80.7

Table 6.5: Sensitivity of the classification based on surface curvature to segmentation. The study involves only sidewall aneurysms and takes into account features derived from aneurysm models (AM) only. The two segmentation methods used are region-growing thresholding and level sets. The study involves four classification cases: two in which the training and the testing sets are segmented using the same method, and two in which the training and the testing sets are segmented using different methods.

Train set	Test set	Best Features AM	Accuracy %
Threshold	Threshold	$g\mu_5$, $g\mu_6$, $m\mu_2$, $m\mu_5$, mk_4	75.4
Threshold	Level Sets	$g\mu_5$, $g\mu_6$, $m\mu_2$, $m\mu_5$, mk_4	59.6
Level Sets	Level Sets	$g\mu_5$, $g\mu_7$, $m\mu_6$, $m\mu_7$, $m\mu_8$	71.9
Level Sets	Threshold	$g\mu_5$, $g\mu_7$, $m\mu_6$, $m\mu_7$, $m\mu_8$	56.14

mine the granularity of the segmentation and different tuning of these parameters may lead sometimes to significantly different results [Zha97, ZFG05].

6.2.3 Sensitivity to Cutting Planes Definition

Similar to Chapter 5, the sensitivity of the classification to cutting plane definition is investigated on four aneurysms. The aneurysm types are sidewall ruptured, sidewall unruptured, bifurcation ruptured, and bifurcation unruptured. All four aneurysms were correctly classified previously in Section 6.2.1. For this analysis, only models of aneurysms with attached parent vessels are considered, since these are the mod-

Table 6.6: Sensitivity of the classification to cutting plane definition. Four aneurysms with parent vessels attached were cut using 3 different planes per parent vessel. N represents the resulting number of models for each aneurysm. The models are classified according to their type (SW or BF).

Type	Ruptured?	N	Best Features	Correctly classified
SW	yes	9	ch	9
SW	no	9	ch	9
BF	yes	27	$c\mu_2$, ch, PVM: mh	27
BF	no	27	$c\mu_2$, ch, PVM: mh	27

els affected by cutting plane definition. Similar to our analysis from the previous chapter, for each aneurysm, several models are created by using three different cutting planes per parent vessel cut. The planes are roughly chosen at distances equal with 1.5, 1 and 0.5 of the vessel diameter as measured at the aneurysm neck. A sidewall aneurysm results in 9 models and a bifurcation aneurysm with three branches results in 27 models. In the figure, the two most extreme models are shown for each aneurysm - when all adjacent vessels are cut using the outermost planes, and then all adjacent vessels are cut using the innermost planes. All other models fall between the two extreme models shown here.

The resulting aneurysm models were classified according to their type (SW or BF) using corresponding best features sets from Table 6.3. All 72 models were correctly classified regardless of the cutting plane choices (Table 6.6). The results suggest the classification based on centroid-radii model and surface curvature is not overly sensitive to cutting plane definition.

6.2.4 Synthetic Data Analysis

To give a better understanding on how the centroid-radii model captures changes in the size and shape of aneurysms, centroid-radii analysis was performed on 4 synthetic aneurysm models. The synthetic models were created using a commercial 3D mechanical CAD software (Dassault Systemes SolidWorks Corp, Concord

MA). The resulting mesh models were refined using the Harpoon automatic mesher (Sharc Ltd, Manchester UK). The results of the analysis are shown in Fig. 6.5. The entropy of the models increases with the model complexity. This is consistent to the findings from Section 6.1.6 that high entropy values of the centroid-radii distance distribution are associated with rupture.

6.3 Discussion

The morphological analysis of intracranial aneurysms started in Chapter 5 is continued in this chapter with the introduction of some novel shape features based on the centroid-radii model and on surface curvatures.

The centroid-radii model is applied on the isolated aneurysmal dome models and describes both the side and the shape of the aneurysms. The entropy of the resulting distribution proved to be strongly associated to rupture, especially for sidewall aneurysms. To the best of our knowledge, the entropy of the centroid-radii model seems to be the most accurate single index for rupture in sidewall aneurysms (80.3%). The centroid-radii model is very easy to use, it is completely automatic and very robust to segmentation.

The surface curvature analysis was performed both on isolated aneurysmal dome models and on combined models incorporating the attached adjacent parent vessel region. Using the entropy of the mean curvature distributions increased the prediction accuracy on bifurcation aneurysms to 79.8%. This represents a significant accuracy improvement compared to when some more established indexes are used. However, the classification based on surface curvature proved to be sensitive to the segmentation method and accuracy results decreased dramatically when the training and testing sets were segmented using different methods. Our recommendation is to use compatible training and testing methods for rupture classification.

The analysis based on the centroid-radii model and surface curvature, used both separately and combined, supports the morphological findings from Chapter 5. Namely, including parent vessel information improves rupture prediction for both sidewall and bifurcation aneurysms and it is vital for bifurcation aneurysms. While using the new features proposed in this current study increased the accuracy performance for bifurcation aneurysms, predicting rupture status on this subset remains a challenging task when compared to the results on sidewall aneurysms. The results support the idea of a clear morphological dichotomy between sidewall and bifurcation aneurysms and this current study is one of the first to describe this morphological split. We believe future research on aneurysm rupture status and risk analysis would greatly benefit from taking these inherent shape differences into account.

While the analysis was performed on a relatively large database and the results are very encouraging, the eventual added value of this new introduced morphological features has to be determined in the clinical setting and would require validation in prospective clinical trials.

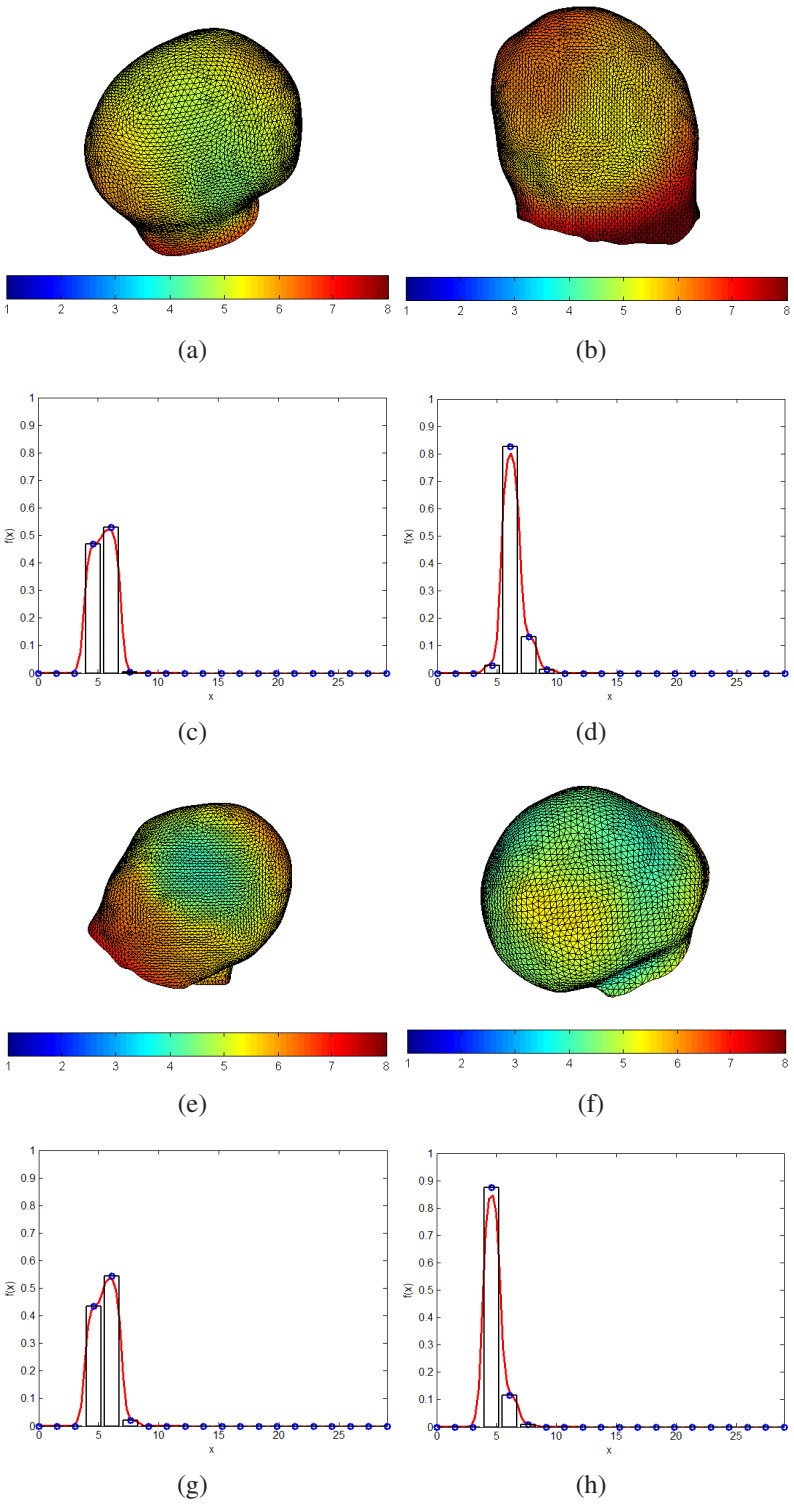

Figure 6.1: Analysis results based on the centroid-radii model on four representative unruptured SIDEWALL aneurysms. The results are shown on aneurysm dome models. (a),(b),(e),(f) Unruptured aneurysms. (c),(d),(g),(h) Corresponding histograms. The approximating probability distribution of centroid-radii distances is shown in red. Unruptured aneurysms have sharp centroid-radii distributions, low entropy and low variance.

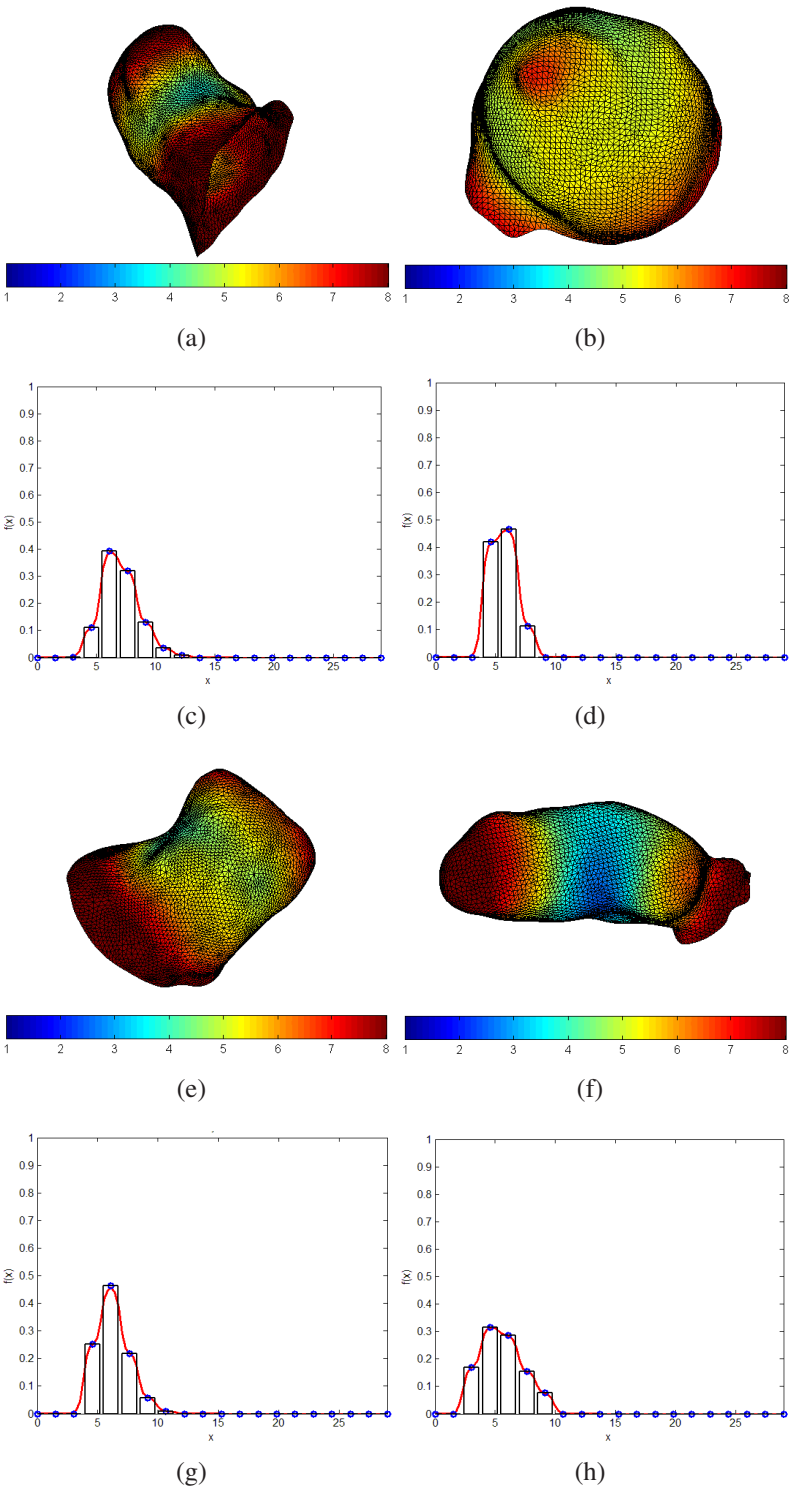

Figure 6.2: Analysis results based on the centroid-radii model on four representative ruptured SIDEWALL aneurysms. The results are shown on aneurysm dome models. (a),(b),(e),(f) Ruptured aneurysms. (c),(d),(g),(h) Corresponding histograms. The approximating probability distribution is shown in red. Ruptured aneurysms have more spread centroid-radii distributions, high entropy and high variance.

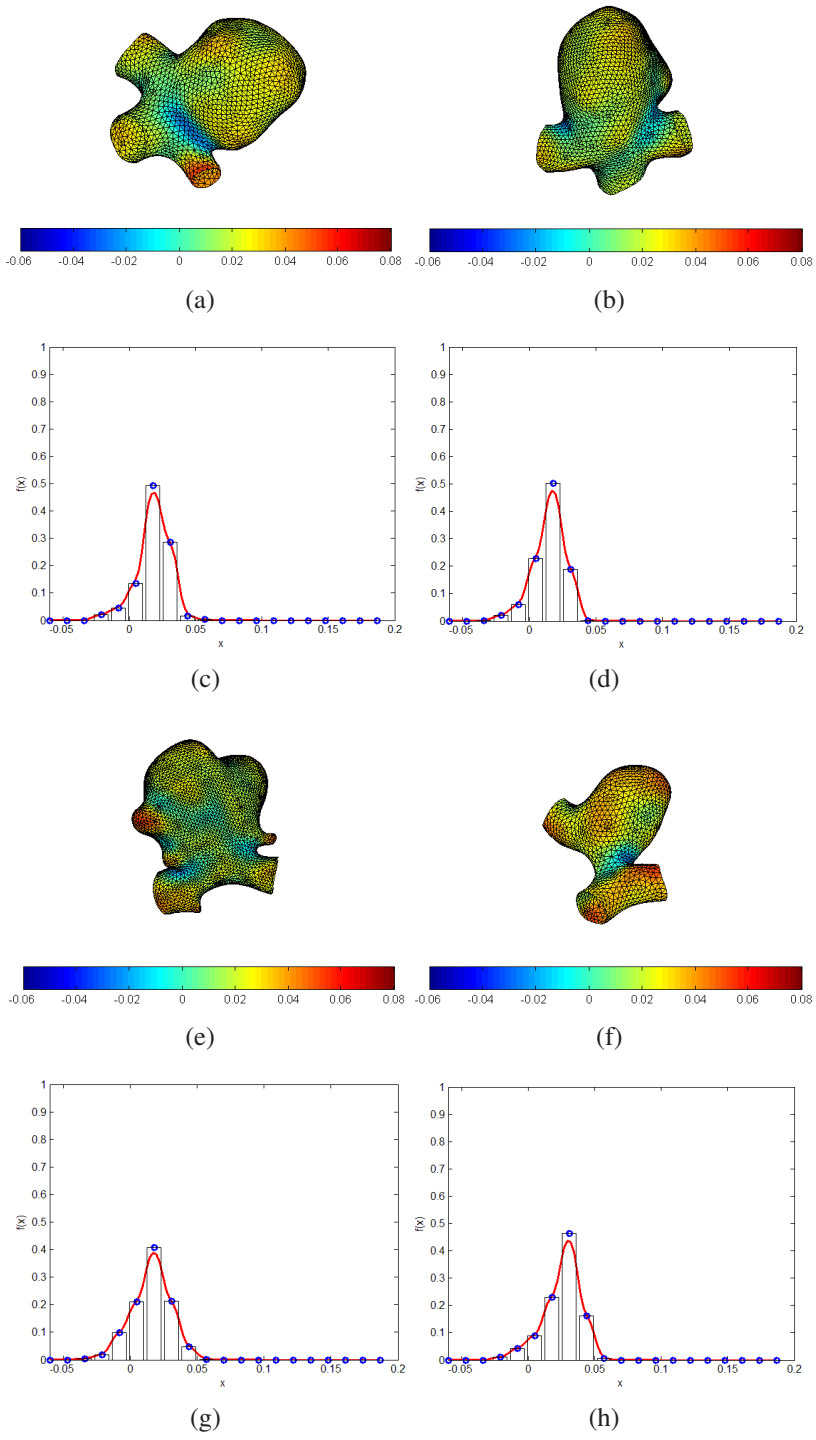

Figure 6.3: Analysis results based on mean curvature statistics on four representative unruptured BIFURCATION aneurysms. The results are illustrated on aneurysms with adjacent parent vessels attached. (a),(b),(e),(f) Unruptured aneurysms. Mean curvature values along the surface. (c),(d),(g),(h) Corresponding histograms. The approximating probability distribution is shown in red. Mean curvature distribution for unruptured aneurysms have lower entropy, variance, skewness and kurtosis compared with ruptured aneurysms.

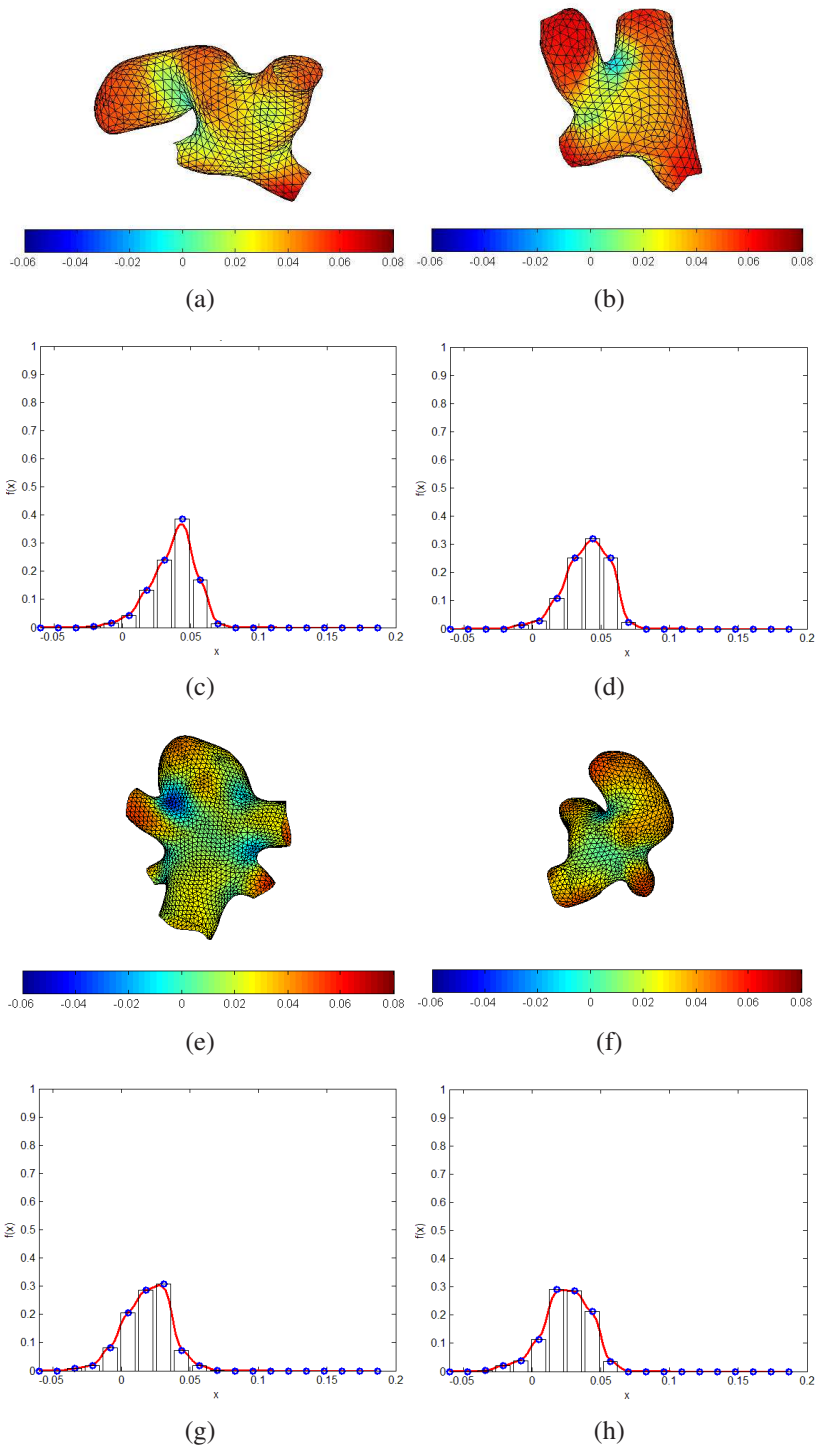

Figure 6.4: Analysis results based on mean curvature statistics on four representative ruptured BIFURCATION aneurysms. The results are illustrated on aneurysms with adjacent parent vessels attached. (a),(b),(e),(f) Ruptured aneurysms. Mean curvature values along the surface. (c),(d),(g),(h) Corresponding histograms. The approximating probability distribution is shown in red. Mean curvature distribution for ruptured aneurysms have higher entropy, variance, skewness and kurtosis compared with unruptured aneurysms.

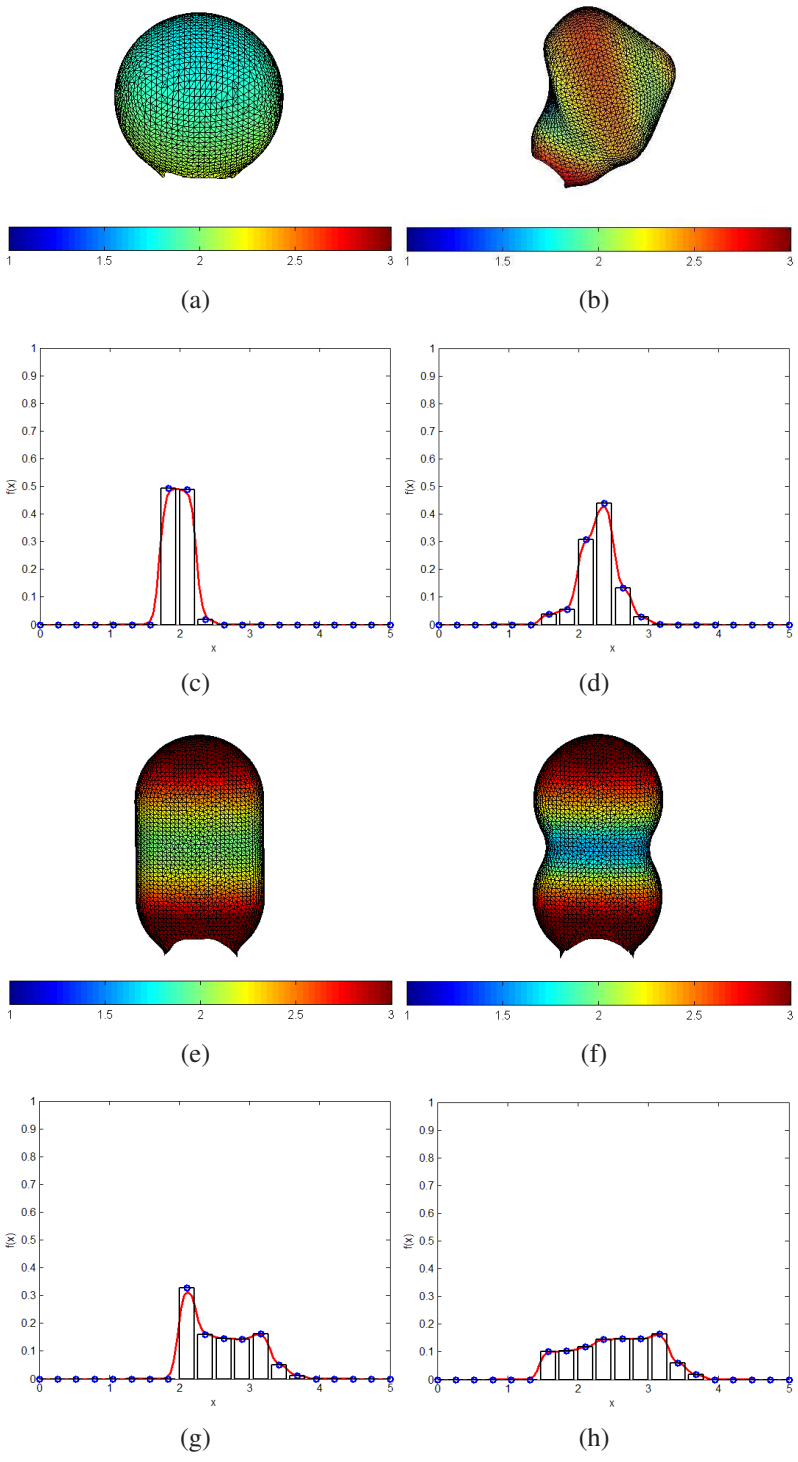

Figure 6.5: Centroid-radii model analysis on four synthetic models. (a),(b),(e),(f) Centroid-radii distance values along the surface of the models. (c),(d),(g),(h) Corresponding histograms. Models entropy values increase from (c) to (h). Higher entropy values are associated with rupture.

Chapter 7

Conclusions and Future Work

This thesis presents solutions for two major areas of intracranial aneurysm analysis, namely aneurysm detection and rupture risk prediction. For both applications, the proposed solutions are based on the writhe number theory introduced in this work. Here, the writhe number was extended from 2D curve theory to 3D surfaces and it was described as a new 3D surface and shape descriptor. From this theory, writhe number-based methods were developed for both automatic detection of aneurysms and rupture status classification.

First, a new method for automated detection of intracranial aneurysms, based on the local 3D shape of the parent vessels, was reported. Surface and shape analysis based on the writhe number was applied to distinguish between tubular and non-tubular regions along the vessels, using the symmetric property of the writhe number. The detection algorithm required only a segmented volume of cerebral vasculature and is otherwise independent of the imaging modality. The method was tested on 3D-RA and CTA patient data. The robustness of the method was investigated analytically and validated experimentally. The method returned few false positive results and did not involve a complex false positive reduction scheme. In our experiments on patient-derived data, the sensitivity of the detection method was

close to 100%.

Second, the writhe number of surfaces was used to analyze the complex shape of intracranial aneurysms and predict their rupture status. A novel analogy was proposed between the writhe number of surfaces and torque. Under this analogy, high writhe number values were interpreted as regions of tension on the surface of the aneurysms, and were an indicator of rupture. A morphological dichotomy was reported between sidewall and bifurcation aneurysms, and the two subtypes were analyzed separately. The analysis was performed both with and without adjacent parent vessels information and leaded us to conclude that the relation between the aneurysmal sac and surrounding vessels was relevant for rupture status prediction. The prediction accuracy obtained using morphological analysis based on writhe number was of $86\pm2\%$ for sidewall aneurysms and of $71\pm3\%$ for bifurcation aneurysms.

Rupture status prediction was further researched by evaluating the utility of the centroid-radii model and surface curvature in discriminating between ruptured and unruptured aneurysms. Statistics derived from the centroid-radii model proved to be highly correlated with rupture, especially in sidewall aneurysms. Combining all the features introduced in this work resulted in a strong statistical model for rupture status prediction. More specifically, the proposed methodology resulted in a prediction accuracy of 88.4% for sidewall aneurysms (vs. 77.1% using established indexes) and 79.8% for bifurcation aneurysms (vs. 64.2% using established indexes).

7.1 Ongoing Research

Ongoing work is focused on improving the results and the methodology for rupture risk prediction. More specifically, we are currently investigating rupture risk pre-

diction in bifurcation aneurysms, which proved to be a more challenging task when compared to the analysis of sidewall aneurysms. One of the findings of this research was that the relationship between an aneurysm and its adjacent parent vessels is essential for the morphological analysis of bifurcation aneurysms. We are currently working to extend the use of the centroid-radii model from aneurysm models to models including parent vessels.

The classification analysis presented here was performed on aneurysms from patient-derived 3D rotational angiography (3D-RA) datasets. 3D-RA imaging is the gold standard in cerebral aneurysm imaging and provides high resolution, high contrast, high signal-to-noise ratio data. However, due to constant improvements in sensitivity and specificity of less-invasive imaging modalities, magnetic resonance angiography (MRA) and computed tomography angiography (CTA) are more and more used for cerebrovascular imaging. To assess the robustness to image modality of the morphological parameters introduced in this work, we are currently performing rupture status prediction on a large database of aneurysms from patient derived CTA datasets.

7.2 Future Work

Although tested on three imaging modalities, the detection method was applied to a relatively small number of datasets (10 for each modality). A larger one modality detection study needs to be performed to better analyze the performance of our method. Detection methods usually fail on small aneurysms, especially on MRA and CTA data. A size analysis of the method needs to be performed on both synthetic data, and on aneurysms of various sizes from patient-derived data.

Each of the detection steps (image reconstruction, segmentation, medial-axis computation, writhe-number analysis) influences the detection accuracy and espe-

cially the false positive rates. At the same time, each of these steps represents an active research field. Improving the segmentation and medial-axis computation will likely improve the specificity of the detection method, and work in this area is one of our main future work directions.

Improving vasculature segmentation will also have a positive impact on increasing the robustness of the prediction method, since some of the morphological parameters presented here, especially curvature, are somewhat sensitive to variations between segmentation methods.

While aneurysm detection and aneurysm rupture status prediction can be used independently, we plan to investigate how the two methods can be combined. This would require an intermediate step, in which the aneurysms are detached from the vasculature using writhe number analysis and taken into account their local neighborhood. This approach could potentially result in automatic isolation of the aneurysms which would completely automate the classification process. It would also provide a unified diagnostic protocol for cerebral aneurysm detection and management.

Both methods require clinical validation studies to assess their effect and potential added value on diagnostic accuracy. We believe the methods introduced in this thesis have the potential to provide additional objective tools, designed to complement the experience and expertize of the clinicians.

A Writhe Number Analysis

A.1 Writhe Number of a Cylinder

If $N(p)$ is a cylinder of radius R and length L and points c_0 and c_1 are the centers of the base and the top of the cylinder respectively, then the medial axis of $N(p)$ is a line segment described by the parametric equation $m(t) = c_0(1-t) + c_1 t$, where $t \in [0,1]$. Without loss of generality, we assume that c_0 is the origin of the local coordinate system, c_1 lies on the x axis and the normal **np** at point p is parallel to the y axis (Fig. A.1). Points p_1, p_2 are chosen as discussed in Section 3.2.1.

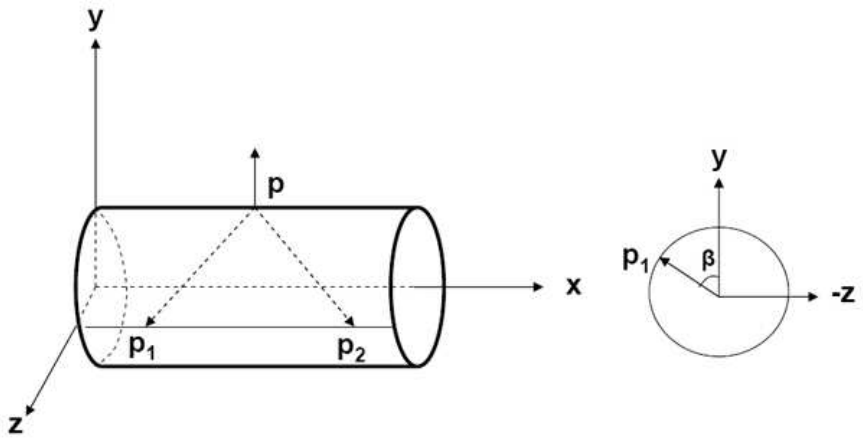

Figure A.1: Computing the writhe number of a cylinder.

Let (p_x, p_y, p_z) be the Cartesian coordinates of point p. Point p_1 sits on the circumference of a circle $C(p_1)$ parallel to the base of $N(p)$. Let β be the angle between y axis and the vector from the origin of $C(p_1)$ to point p_1 (Fig. A.1). The same holds for point p_2. For any pair of points (p_1, p_2) the following are true:

$$(p_x, p_y, p_z) = (\frac{L}{2}, R, 0),$$

$$(p_{1x}, p_{1y}, p_{1z}) = (Lt, R\cos\beta, R\sin\beta), t \in [0,1],$$

$$(p_{2x}, p_{2y}, p_{2z}) = (L(1-t), R\cos\beta, R\sin\beta), t \in [0,1],$$

$$(p_1 - p) = (Lt - \frac{L}{2}, R(\cos\beta - 1), R\sin\beta), t \in [0,1],$$

$$(p_2 - p) = (-Lt + \frac{L}{2}, R(\cos\beta - 1), R\sin\beta), t \in [0,1],$$

$$\mathbf{np} = (0,1,0),$$

$$\mathbf{np}_1 = (0, \cos\beta, \sin\beta),$$

$$\mathbf{np}_2 = (0, \cos\beta, \sin\beta),$$

$$\mathbf{np} \times \mathbf{np}_1 = (\sin\beta, 0, 0),$$

$$\mathbf{np} \times \mathbf{np}_2 = (\sin\beta, 0, 0),$$

$$w(p, p_1) = (p_1 - p) \cdot (\mathbf{np} \times \mathbf{np}_1) = (Lt - \frac{L}{2})\sin\beta,$$

$$w(p, p_2) = (p_2 - p) \cdot (\mathbf{np} \times \mathbf{np}_2) = -(Lt - \frac{L}{2})\sin\beta,$$

$$w(p, p_1) = -w(p, p_2).$$

A.2 Writhe Number of an Extruded Surface Along a Parabola

An arbitrary parabola H, with the apex in the origin of the coordinate system, is defined by the parametric equations $x = at^2, y = 2at, t \in \mathbb{R}$. A point h on H has coordinates $(at^2, 2at)$ and the tangent to H at h is given by equation $ty = x + at^2$.

Given a surface point p, let $N(p)$ be an extruded surface along H, having H as its medial axis. Point p lies on the circumference of a circle $C(p)$, with center c and perpendicular to H. Note that all the points on $C(p)$ have the same local neighborhood as p and implicitly the same writhe number. Without loss of generality, we assume that H lies in the xy plane, c is the apex of H and p is the apex of the largest parabola on the extruded surface, such that the normal **np** to the surface is parallel to the x axis (Fig. A.2). Points p_1, p_2 are chosen as discussed in Section 3.2.2.

Let (p_x, p_y, p_z) be the Cartesian coordinates of point p and **tp** be the tangent to the surface at point p. Point p_1 sits on the circumference of a circle $C(p_1)$ with center c_1 and perpendicular to H. $C(p_1)$ intersects the largest parabola on the extruded

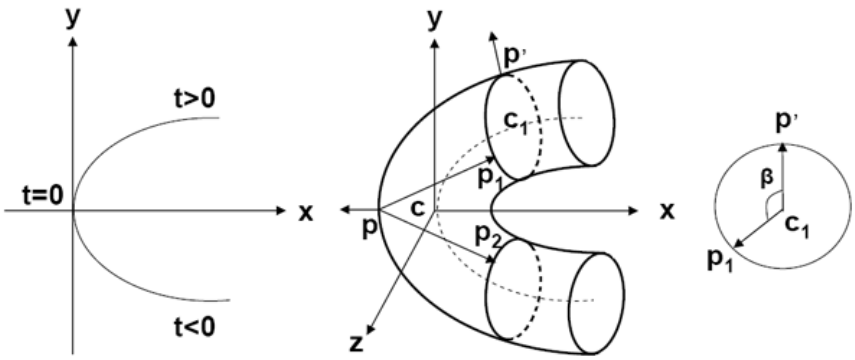

Figure A.2: Computing the writhe number of an extruded parabola.

surface in a point $p^{'}$, with normal $\mathbf{np}^{'}$ to the surface. Let β be the angle between $\mathbf{np}^{'}$ and the vector from c_1 to point p_1 (Fig. A.1). The same holds for point p_2. For any pair of points (p_1, p_2) the following are true:

$$
\begin{aligned}
&(c_x, c_y, c_z) = (0, 0, 0),\\
&(c_{1x}, c_{1y}, c_{1z}) = (at^2, 2at, 0), t \in \mathbb{R},\\
&(c_{2x}, c_{2y}, c_{2z}) = (at^2, -2at, 0), t \in \mathbb{R},\\
&\mathbf{nc} = (-1, 0, 0),\\
&\mathbf{nc}_1 = (-\frac{\frac{1}{t}}{\sqrt{1+\frac{1}{t^2}}}, \frac{1}{\sqrt{1+\frac{1}{t^2}}}, 0), t \in \mathbb{R},\\
&\mathbf{nc}_2 = (-\frac{\frac{1}{t}}{\sqrt{1+\frac{1}{t^2}}}, -\frac{1}{\sqrt{1+\frac{1}{t^2}}}, 0), t \in \mathbb{R},\\
&\mathbf{tc}_1 = (\frac{1}{\sqrt{1+\frac{1}{t^2}}}, \frac{\frac{1}{t}}{\sqrt{1+\frac{1}{t^2}}}, 0), t \in \mathbb{R},\\
&\mathbf{tc}_2 = (\frac{1}{\sqrt{1+\frac{1}{t^2}}}, -\frac{\frac{1}{t}}{\sqrt{1+\frac{1}{t^2}}}, 0), t \in \mathbb{R}
\end{aligned}
$$

The tuple $(tc_1, nc_1, tc_1 \times nc_1)$ is the basis of a 3D-RA orthogonal coordinate system local to $C(p_1)$. Similarly, $(tc_2, nc_2, tc_2 \times nc_2)$ is the basis of an orthogonal coordinate system local to $C(p_2)$. We will express p_1 and p_2 locally in terms of the

new bases.

$$(p_x, p_y, p_z) = (-R, 0, 0),$$

$$p_{1x} = at^2 - \frac{\frac{R}{t}}{\sqrt{1+\frac{1}{t^2}}}\cos\beta, t \in \mathbb{R},$$

$$p_{1y} = 2at + \frac{R}{\sqrt{1+\frac{1}{t^2}}}\cos\beta, t \in \mathbb{R},$$

$$p_{1z} = R\sin\beta,$$

$$p_{2x} = at^2 - \frac{\frac{R}{t}}{\sqrt{1+\frac{1}{t^2}}}\cos\beta, t \in \mathbb{R},$$

$$p_{2y} = -2at + \frac{R}{\sqrt{1+\frac{1}{t^2}}}\cos\beta, t \in \mathbb{R},$$

$$p_{2z} = R\sin\beta,$$

$$(p_1 - p)_x = at^2 + R(1 - \frac{\frac{R}{t}}{\sqrt{1+\frac{1}{t^2}}}\cos\beta), t \in \mathbb{R},$$

$$(p_1 - p)_y = 2at - \frac{R}{\sqrt{1-\frac{1}{t^2}}}\cos\beta, t \in \mathbb{R},$$

$$(p_1 - p)_z = R\sin\beta,$$

$$(p_2 - p)_x = at^2 + R(1 - \frac{\frac{R}{t}}{\sqrt{1+\frac{1}{t^2}}}\cos\beta), t \in \mathbb{R},$$

$$(p_2 - p)_y = -2at + \frac{R}{\sqrt{1+\frac{1}{t^2}}}\cos\beta, t \in \mathbb{R},$$

$$(p_2 - p)_z = R\sin\beta,$$

$$\mathbf{np} = (-1, 0, 0),$$

$$\mathbf{nc}_1 = (-\frac{\frac{1}{t}}{\sqrt{1+\frac{1}{t^2}}}, \frac{1}{\sqrt{1+\frac{1}{t^2}}}, \sin\beta), t \in \mathbb{R},$$

$$\mathbf{nc}_2 = (-\frac{\frac{1}{t}}{\sqrt{1+\frac{1}{t^2}}}, -\frac{1}{\sqrt{1+\frac{1}{t^2}}}, \sin\beta), t \in \mathbb{R},$$

$$\mathbf{np} \times \mathbf{np}_1 = (0, -\sin\beta, -\frac{1}{\sqrt{1+\frac{1}{t^2}}}), t \in \mathbb{R},$$

$$\mathbf{np} \times \mathbf{np}_2 = (0, -\sin\beta, \frac{1}{\sqrt{1+\frac{1}{t^2}}}), t \in \mathbb{R},$$

$$\begin{aligned} w(p, p_1) &= (p_1 - p) \cdot (\mathbf{np} \times \mathbf{np}_1) \\ &= -(2at - \frac{R\cos\beta}{\sqrt{1-\frac{1}{t^2}}})\sin\beta - \frac{R}{\sqrt{1+\frac{1}{t^2}}}\sin\beta, \end{aligned}$$

$$\begin{aligned} w(p, p_2) &= (p_2 - p) \cdot (\mathbf{np} \times \mathbf{np}_2) \\ &= -(-2at + \frac{R\cos\beta}{\sqrt{1-\frac{1}{t^2}}})\sin\beta + \frac{R}{\sqrt{1+\frac{1}{t^2}}}\sin\beta, \end{aligned}$$

$$w(p, p_1) = -w(p, p_2).$$

Bibliography

[ACSD+03] Pierre Alliez, David Cohen-Steiner, Olivier Devillers, Bruno Lvy, and Mathieu Desbrun. Anisotropic polygonal remeshing. *ACM Transactions on Graphics*, 22, 2003.

[AEW04] PK. Agarwal, H. Edelsbrunner, and Y. Wang. Computing the writhing number of a polygonal knot. *Discrete & Computational Geometry*, 32(1):37–53, 2004.

[Ahn04] Sung Joon Ahn. *Least squares orthogonal distance fitting of curves and surfaces in space*, volume 3151 of *Lecture Notes in Computer Science*. Springer Berlin/Heidelberg, 2004.

[ALK+04] H. Arimura, Q. Li, Y. Korogi, T. Hirai, H. Abe, Y. Yamashita, S. Katsuragawa, R. Ikeda, and K. Doi. Automated computerized scheme for detection of unruptured intracranial aneurysms in three-dimensional magnetic resonance angiography. *Academic Radiology*, 11(10):1093–1104, 2004.

[ALK+05] H. Arimura, Q. Li, Y. Korogi, T. Hirai, H. Abe, Y. Yamashita, S. Katsuragawa, R. Ikeda, and K. Doi. CAD scheme for detection of intracranial aneurysms in MRA based on 3D analysis of vessels skeletons and enhanced aneurysms. *Proc. of SPIE*, 5747:967–974, 2005.

[ALK+06] H. Arimura, Q. Li, Y. Korogi, T. Hirai, S. Katsuragawa, Y. Yamashita, K. Tsuchiya, and K. Doi. Computerized detection of intracranial aneurysms for three-dimensional MR angiography: Feature extraction of small protrusions based on a shape-based difference image technique. *Medical Physics*, 33(2):394–401, 2006.

[APT+07] Yulia Arzhaeva, Mathias Prokop, David M. J. Tax, Pim A. De Jong, Cornelia M. SchaeferProkop, and Bram van Ginneken. Computer-aided detection of interstitial abnormalities in chest radiographs using a reference standard based on computed tomography. *Medical Physics*, 34(12):4798–4809, 2007.

[BA97] Adrian W Bowman and Adelchi Azzalini. *Applied Smoothing Techniques for Data Analysis*. Oxford University Press, USA, 1997.

[Blo97] Ethan D. Bloch. *A First Course in Geometric Topology and Differential Geometry*. Birkhuser Boston, 1997.

[BP06] Mitchell A Berger and Chris Prior. The writhe of open and closed curves. *Journal of Physics A: Mathematical and General*, 38(26):8321–8348, 2006.

[BReB+03] J. Beck, S. Rohde, M. el Beltagy, M. Zimmermann, J. Berkefeld, V. Seifert, and A. Raabe. Difference in configuration of ruptured and unruptured intracranial aneurysms determined by biplanar digital subtraction angiography. *Acta Neurochirurgica*, 145(10):861–865, 2003.

[BSH+10] Merih I. Baharoglu, Clemens M. Schirmer, Daniel A. Hoit, Bu-Lang Gao, and Adel M. Malek. Aneurysm Inflow-Angle as a Discriminant for Rupture in Sidewall Cerebral Aneurysms: Morphometric and Computational Fluid Dynamic Analysis. *Stroke*, 41(7):1423–1430, 2010.

[BSN06] J L Brisman, J K Song, and D W Newell. Cerebral aneurysms. *New England Journal of Medicine*, 355(9):928–939, 2006.

[BST05] Sylvain Bouix, Kaleem Siddiqi, and Allen Tannenbaum. Flux driven automatic centerline extraction. *Medical Image Analysis*, 9(3):209–221, 2005.

[CCD+07] Bert A. Coert, Steven D. Chang, Huy M. Do, Michael P. Marks, and Gary K. Steinberg. Surgical and endovascular management of symptomatic posterior circulation fusiform aneurysms. *J Neurosurg*, 106:855865, 2007.

[CGR08] Juan C. Caicedo, Fabio A. Gonzalez, and Eduardo Romero. Content-based medical image retrieval using low-level visual features and modality identification. *Advances in Multilingual and Multimodal Information Retrieval*, LNCS 5152:615–622, 2008.

[CHB91] C. C. Chang, S. M. Hwang, and D. J. Buehrer. A shape recognition scheme based on relative distances of feature points from the centroid. *Pattern Recognition*, 24(11):1053–1063, 1991.

[CSM03a] David Cohen-Steiner and Jean-Marie Morvan. Approximation of normal cycles. 2003.

[CSM03b] David Cohen-Steiner and Jean-Marie Morvan. Restricted delaunay triangulations and normal cycle. *ACM Sympos. Comput. Geom.*, pages 312–321, 2003.

[CT06] Thomas M. Cover and Joy A. Thomas. *Elements of information theory*. Wiley, 2nd edition, 2006.

[DHKL01] Nira Dyn, Kai Hormann, Sun-Jeong Kim, and David Levin. Optimizing 3d triangulations using discrete curvature analysis. pages 135–146, 2001.

[DTM+08] Sujan Dhar, Markus Tremmel, J Mocco, Minsuok Kim, Junichi Yamamoto, Adnan H. Siddiqui, L. Nelson Hopkins, and Hui Meng. Morphology parameters for intracranial aneurysm rupture risk assessment. *Neurosurgery*, 63(2):185–197, 2008.

[EMO08] Jonathan A. Edlow, Adel M. Malek, and Christopher S. Ogilvy. Aneurysmal subarachnoid hemorrhage: update for emergency physicians. *Journal of Emergency Medicine*, 34(3):237–251, 2008.

[Fan01] Shuang Fan. Shape representation and retrieval using distance histograms,. Technical report, Department of computer science, University of Alberta, Edmonton, Alberta, Canada, 2001.

[FEH01] jr Frank E. Harrell. *Regression modeling strategies*. Springer Series in Statistics, 2001.

[FPAB04] Y. Fridman, S. M. Pizer, S. Aylward, and E. Bullitt. Extracting branching tubular object geometry via cores. *Med Image Anal*, 8(3):169–76, 2004.

[FPBJES03] Jr. Ferdinand P. Beer, E. Russell Johnston, Elliot R. Eisenberg, and George H. Staab. *Vector Mechanics for Engineers: Statics*. McGraw-Hill Science, 2003.

[Ful71] F. Brock Fuller. The writhing number of a space curve. *Proceedings of the National Academy of Sciences of the USA*, 68(4):815–819, 1971.

[GG06] TD Gatzke and CM Grimm. Estimating curvature on triangular meshes. *International Journal of Shape Modeling*, 12:1–28, 2006.

[GJMP06] R. Gupta, S E Jones, E A Q Mooyaart, and S R Pomerantz. Computed tomographic angiography in stroke imaging: fundamental principles, pathologic findings, and common pitfalls. *Seminars in Ultrasound, CT, and MRI*, 27(3):221–2423, 2006.

[Gra93] Alfred Gray. *Modern differential geometry of curves and surfaces*. CRC Press, 1993.

[Ham93] B. Hamann. Curvature approximation for triangulated surfaces. pages 139–153, 1993.

[Har84] F. E. Harrell. Regression modelling strategies for improved prognostic prediction. *Statistics in Medicine*, 3:143–152, 1984.

[Har90] Wolfgang Hardle. *Applied Nonparametric Regression*. Cambridge University Press, 1990.

[Har91] Wolfgang Hardle. *Smoothing Techniques*. Springer-Verlag, 1991.

[HF07] M. Hernandez and A. F. Frangi. Non-parametric geodesic active regions: method and evaluation for cerebral aneurysms segmentation in 3dra and cta. *Med Image Anal*, 11(3):224–41, 2007.

[HGLS08] Monica K Hurdal, Juan B Gutierrez, Christian Laing, and Deborah A Smith. Shape analysis for automated sulcal classification and parcellation of MRI data. *Journal of Combinatorial Optimization*, 15(3):257–275, 2008.

[HH94] Istvan Hargittai and Magdolna Hargittai. *Symmetry: A Unifying Concept*. Shelter Publications, 1994.

[HL93] Josef Hoschek and Dieter Lasser. *Fundamentals of computer-aided geometric design*. AK Peters, 1993.

[HMM+03] Naoto Hayashi, Yoshitaka Masutani, Tomohiko Masumoto, Harushi Mori, Akira Kunimatsu, Osamu Abe, Shigeki Aoki, Kuni Ohtomo, Naoki Takano, and Kazuhiko Matsumoto. Feasibility of a curvature-based enhanced display system for detecting cerebral aneurysms in mr angiography. *Magnetic Resonance in Medical Sciences*, 2:29–36, 2003.

[HSF+07] Brian L. Hoh, Christopher L. Sistrom, Christopher S. Firment, Gregory L. Fautheree, Gregory J. Velat, Jobyna H. Whiting, John F. Reavey-Cantwell, and Stephen B. Lewis. Bottleneck factor and height-width ratio: Association with ruptured aneurysms in patients with multiple cerebral aneurysms. *Neurosurgery*, 61(4):716–723, 2007.

[JGP+01] M. R. Johnson, C. D. Good, W. D. Penny, P. R. Barnes, and J. W. Scadding. Lesson of the week: Playing the odds in clinical decision making: lessons from berry aneurysms undetected by magnetic resonance angiography. *BMJ*, 322(7298):1347–9, 2001.

[JKK05] N.L. Johnson, A.W. Kemp, and S. Kotz. *Univariate discrete distributions*. Wiley Interscience, 3nd edition, 2005.

[JPP00] Seppo Juvela, Matti Porras, and Kristiina Poussa. Natural history of unruptured intracranial aneurysms: Probability and risk factors for aneurysm rupture. *Journal of Neurosurgery*, 93:379–387, 2000.

[Juv04] S. Juvela. Treatment Options of Unruptured Intracranial Aneurysms. *Stroke*, 35(2):372–374, 2004.

[KE09] Ioannis Koktzoglou and Robert R. Edelman. Ghost magnetic resonance angiography. *Magnetic Resonance in Medicine*, 61:1515–1519, 2009.

[KKH06] S. Kobashi, K. Kondo, and Y. Hata. Computer-aided diagnosis of intracranial aneurysms in MRA images with case-based reasoning. *IEICE Transactions on Information and Systems*, 89(1):340–350, 2006.

[KL00] Konstantin Klenin and Jrg Langowski. Computation of writhe in modeling of supercoiled DNA. *Biopolymers*, 54(5):307–317, 2000.

[KLZL07] Xiaodong Kong, Qingshan Luo, Guihua Zeng, and Moon Ho Lee. A new shape descriptor based on centroid-radii model and wavelet transform. *Optics Communications*, 273(2):362 – 366, 2007.

[KQ03] C. Kirbas and F K H Quek. Vessel extraction techniques and algorithms: a survey. *Proc of Third IEEE Symposium on BioInformatics and BioEngineering*, pages 238–245, 2003.

[KW07] Bernhard Kis and Werner Weber. Treatment of unruptured cerebral aneurysms. *Proc of Third IEEE Symposium on BioInformatics and BioEngineering*, 17(3):159–166, 2007.

[LeBB09] Rohan R. Lall, Christopher S. Eddl eman, Bernard R. Bendok, and H. Hunt Batjer. Unruptured intracranial aneurysms and the assessment of rupture risk based on anatomical and morphological factors: sifting through the sands of data. *Neurosurgical Focus*, 26(5), 2009.

[LMBM10] Alexandra Lauric, Eric L. Miller, Merih I. Baharoglu, and Adel M. Malek. 3d shape analysis of intracranial aneurysms using the writhe number as a discriminant for rupture. *IEEE Transactions on Medical Imaging*, 2010. under review.

[LMFM09] Alexandra Lauric, Eric Miller, Sarah Frisken, and Adel M. Malek. Automated detection of intracranial aneurysms based on parent vessel 3D analysis. *Medical Imaging Analysis*, 2009.

[LZ05] Suhuai Luo and Youliang Zhong. Extraction of brain vessels from magnetic resonance angiographic images: concise literature review, challenges, and proposals. *Conf Proc IEEE Eng Med Biol Soc.*, 2:1422–1425, 2005.

[MDMP+07] R. D. Millan, L. Dempere-Marco, J. M. Pozo, J. R. Cebral, and A. F. Frangi. Morphological characterization of intracranial aneurysms using 3-d moment invariants. *IEEE Transactions on Medical Imaging*, 26(9):1270–1282, SEP 2007.

[MHR04] B. S. Ma, R. E. Harbaugh, and M. L. Raghavan. Three-dimensional geometrical characterization of cerebral aneurysms. *Annals of Biomedical Engineering*, 32(2):264–273, FEB 2004.

[Mor08] Jean-Marie Morvan. *Generelized Curvatures*, volume 2 of *Geometry and Computing*. Springer Verlag, 2008.

[MSR07] Evgeni Magid, Octavian Soldea, and Ehud Rivlin. A comparison of gaussian and mean curvature estimation methods on triangular meshes of range image data. *Computer Vision and Image Understanding*, 107(3):139 – 159, 2007.

[MSW00] Szymon Mercik, Zuzanna Siwy, and Karina Weron. What can be learnt from the analysis of short time series of ion channel recordings. *Physica A: Statistical Mechanics and its Applications*, 276(3-4):376 – 390, 2000.

[MW00] D. S. Meek and D. J. Walton. On surface normal and gaussian curvature approximations given data sampled from a smooth surface. *Computer Aided Geometric Design*, 17(6):521 – 543, 2000.

[NDM+05] Brian V. Nahed, Michael L. DiLuna, Thomas Morgan, Eylem Ocal, Abigail A. Hawkins, Koray Ozduman, Kristopher T. Kahle, Andrea Chamberlain, Arun P. Amar, and Murat Gunel. Hypertension, age, and location predict rupture of small intracranial aneurysms. *Neurosurgery*, 57(4):676–683, 2005.

[O'N06] Barrett O'Neill. *Elementry differential geometry*. Elsevier Academic Press, second edition, 2006.

[oUIAI98] The International Study of Unruptured Intracranial Aneurysm Investigators. Unruptured intracranial aneurysmsrisk of rupture and risk of surgical intervention. *N Engl J Med*, 339:17251733, 1998.

[PXP00] D L Pham, C Xu, and J L Prince. Current methods in medical image segmentation. *Annual Review of Biomedical Engineering*, 2:315–337, 2000.

[RDAvG98] G J Rinkel, M. Djibuti, A. Algra, and J van Gijn. Prevalence and risk of rupture of intracranial aneurysms: a systematic review. *Stroke*, 29(1):251–256, 1998.

[RLB+05] Stefan Rohde, Katharina Lahmann, Jrgen Beck, Reinhold Nafe, Bernard Yan, Andreas Raabe, and Joachim Berkefeld. Fourier analysis of intracranial aneurysms: towards an objective and quantitative evaluation of the shape of aneurysms. *Neuroradiology*, 47(2):121–126, 2005.

[RM03] V. Rossetto and A C Maggs. Writhing geometry of open DNA. *Journal of Chemical Physics*, 118:9864–9874, 2003.

[RMH05] Madhavan L Raghavan, Baoshun Ma, and Robert E Harbaugh. Quantified aneurysm shape and rupture risk. *Journal of neurosurgery*, 102(2):355–362, 2005.

[RP09] A. G. Radaelli and J. Peiro. On the segmentation of vascular geometries from medical images. *Communications in Numerical Methods in Engineering*, 2009.

[RS06] W J Van Rooij and M. Sluzewski. Procedural morbidity and mortality of elective coil treatment of unruptured intracranial aneurysms. *American Journal of Neuroradiology*, 27(8):1678–1680, 2006.

[SA04] Helene Schulerud and Fritz Albregtsen. Many are called, but few are chosen. feature selection and error estimation in high dimensional spaces. *Computer Methods and Programs in Biomedicine*, 73:91–99, 2004.

[Sch97] Wouter I. Schievink. Intracranial Aneurysms. *N Engl J Med*, 336(1):28–40, 1997.

[SCH06] Xiangjun Shi, H.D. Cheng, and Liming Hu. Mass detection and classification in breast ultrasound images using fuzzy svm. *JCIS-2006 Proceedings*, 2006.

[Set99] J. A. Sethian. *Level set methods and fast marching methods*. Cambridge University Press, 1999.

[SJY+09] Hiromitsu Sumikawa, Takeshi Johkoh, Shuji Yamamoto, Masahiro Yanagawa, Atsuo Inoue, Osamu Honda, Shigeyuki Yoshida, Noriyuki Tomiyama, and Hironobu Nakamura. Computed tomography values calculation and volume histogram analysis for various computed tomographic patterns of diffuse lung diseases. *Journal of Computer Assisted Tomography*, 33(5):731–738, 2009.

[SOT+04] Masaaki Shojima, Marie Oshima, Kiyoshi Takagi, Ryo Torii, Motoharu Hayakawa, Kazuhiro Katada, Akio Morita, and Takaaki Kirino. Magnitude and Role of Wall Shear Stress on Cerebral Aneurysm: Computational Fluid Dynamic Study of 20 Middle Cerebral Artery Aneurysms. *Stroke*, 35(11):2500–2505, 2004.

[ST06] Sheri D. Sheppard and Benson H. Tongue. *Statics : analysis & design of systems in equilibrium*. John Wiley & Sons, 2006.

[Sta05] E. L. Starostin. *Physical and Numerical Models in Knot Theory Including Applications to the Life Sciences.*, chapter On the writhing

number of a non-closed curve., page 525545. World Scientific Publishing, 2005.

[STS06] Jose I. Suarez, Robert W. Tarr, and Warren R. Selman. Aneurysmal Subarachnoid Hemorrhage. *N Engl J Med*, 354(4):387–396, 2006.

[SUS09] K.Prabhu Shetty, V. R. Udupi, and Bairu K. Saptalakar. Wavelet based microcalcification detection on mammographic images. *International Journal of Computer Science and Network Security*, 9(7):213–217, 2009.

[SV01] D. Saupe and D.V. Vranic. 3d model retrieval with spherical harmonics and moments. In *Proceedings of DAGM*, pages 392–397. Munich, 2001.

[SW92] E.M. Stokely and S.Y. Wu. Surface parametrization and curvature measurement of arbitrary 3-d objects: Five practical methods. *IEEE Transactions on Pattern Analysis and Machine Intelligence*, 14:833–840, 1992.

[Tau95] Gabriel Taubin. Estimating the tensor of curvature of a surface from a polyhedral approximation. In *The Fifth International Conference on Computer Vision*, page 902907, 1995.

[TK03] Sergios Theodoridis and Konstantinos Koutroumbas. *Pattern Recognition*. Academic Press, 2003.

[TOT00] Kian-Lee Tan, Beng Chin Ooi, and Lay Foo Thiang. Indexing shapes in image databases using the centroid-radii model. *Data & Knowledge Engineering*, 32:271–289, 2000.

[TOT03] Kian-Lee Tan, Beng Chin Ooi, and Lay Foo Thiang. Retrieving similar shapes effectively and efficiently. *Multimedia Tools and Applications*, 19:111–134, 2003.

[UAY+05] Y. Uchiyama, H. Ando, R. Yokoyama, T. Hara, H. Fujita, and T. Iwama. Computer-aided diagnosis scheme for detection of unruptured intracranial aneurysms in MR angiography. *Conf Proc IEEE Eng Med Biol Soc.*, 3:3031–3034, 2005.

[UTH+99] Hiroshi Ujiie, Hiroyuki Tachibana, Osamu Hiramatsu, Andrew L. Hazel, Takeshi Matsumoto, Yasuo Ogasawara, Hiroshi Nakajima, Tomokatsu Hori, Kintomo Takakura, and Fumihiko Kajiya. Effects of size and shape (aspect ratio) on the hemodynamics of saccular aneurysms: A possible index for surgical treatment of intracranial aneurysms. *Neurosurgery*, 45(1):119–130, 1999.

[vGKR07] Jan van Gijn, Richard S Kerr, and Gabriel JE Rinkel. Subarachnoid haemorrhage. *Lancet*, 369(9558):306–318, 2007.

[VS00] D.V. Vranic and D. Saupe. 3d medel retrieval. In *Spring Conference on Computer Graphics and its Applications*, pages 89–93. Comenius University Slovakia, 2000.

[WBHT06] S. Q. Wolfe, M. K. Baskaya, R. C. Heros, and R. P. Tummala. Cerebral aneurysms: learning from the past and looking toward the future. *Clin. Neurosurg.*, 53:157178, 2006.

[Wei05] Bryce Weir. Patients with small, asymptomatic, unruptured intracranial aneurysms and no history of subarachnoid hemorrhage should generally be treated conservatively: against. *Stroke*, 36:4010–411, 2005.

[Whi98] Ross T. Whitaker. A level-set approach to 3d reconstruction from range data. *International Journal of Computer Vision*, 29(3):203–231, 1998.

[Wie03] David O Wiebers. Unruptured intracranial aneurysms: natural history, clinical outcome, and risks of surgical and endovascular treatment. *The Lancet*, 362(9378):103 – 110, 2003.

[Wie05] David O. Wiebers. Patients with small, asymptomatic, unruptured intracranial aneurysms and no history of subarachnoid hemorrhage should generally be treated conservatively: for. *Stroke*, 36:408–409, 2005.

[Wil97] G.P. Williams. *Chaos theory tamed*. Washington, DC: National Academy Press, 1997.

[WW00] J. M. Wardlaw and P. M. White. The detection and management of unruptured intracranial aneurysms. *Brain*, 123(2):205–221, 2000.

[YM06] Azadeh Yadollahi and Zahra M. K. Moussavi. A robust method for heart sounds localization using lung sounds entropy. *IEEE Transactions on Biomedical Engineering*, 33(3):497–502, 2006.

[YPC+06] P. A. Yushkevich, J. Piven, H. Cody, S. Ho, J. C. Gee, and G. Gerig. User-guided level set segmentation of anatomical structures with itk-snap. *NeuroImage*, 31:11161128, 2006. Special Issue on ISC/NA-MIC/MICCAI Workshop on Open-Source Software.

[ZD04] Gregory J. Zipfel and Ralph G Dacey. Update on the management of unruptured intracranial aneurysms. *Neurosurgical Focus*, 17(5), 2004.

[ZFG05] Hui Zhang, Jason E. Fritts, and Sally A. Goldman. A co-evaluation framework for improving segmentation evaluation. *Signal Processing, Sensor Fusion, and Target Recognition XIV*, 5809(1):420–430, 2005.

[Zha97] Y.J. Zhang. Evaluation and comparison of different segmentation algorithms. *Pattern Recognition Letters*, 18(10):963 – 974, 1997.